The Heterogeneous Partial Oxidation of Light Alkanes

Yee San Su

M. S. in Chemical Engineering Practice
Massachusetts Institute of Technology, 2000

B. S. in Chemical Engineering
Stanford University, 1998

Submitted to the Department of Chemical Engineering in Partial Fulfillment
of the Requirements for the Degree of

Doctor of Philosophy in Chemical Engineering

at the

MASSACHUSETTS INSTITUTE OF TECHNOLOGY

February 2004

© Massachusetts Institute of Technology 2004. All rights reserved.

Author: _____
Department of Chemical Engineering
January 16, 2004

Certified by: _____
Professor William H. Green
Associate Professor of Chemical Engineering
Thesis Supervisor

and: _____
Professor Jackie Y. Ying
Professor of Chemical Engineering
Thesis Supervisor

Accepted by: _____
Professor Daniel Blankschtein
Professor of Chemical Engineering
Chairman, Committee for Graduate Studies

MASSACHUSETTS INSTITUTE OF TECHNOLOGY
MAR 0 2 2004
LIBRARIES

ARCHIVES

Heterogeneous Partial Oxidation of Light Alkanes

Yee San Su

M. S. in Chemical Engineering Practice
Massachusetts Institute of Technology, 2000

B. S. in Chemical Engineering
Stanford University, 1998

Submitted to the Department of Chemical Engineering
on January 6, 2004 in Partial Fulfillment of the
Requirements for the Degree of Doctor of Philosophy in Chemical Engineering

Abstract

Within the petrochemical industry, a sizeable economic incentive exists for the upgrading of low-value, light alkanes. For instance, the dehydrogenation of ethane to ethene is of considerable interest due to ethene's use as a polymeric and chemical precursor. Partial oxidation provides an attractive alternative to standard pyrolysis methods for alkane-to-alkene conversion. Unlike pyrolysis, partial oxidative routes are largely unaffected by coke formation and have the added benefit of exothermicity. With the inclusion of oxygen as a reactant, however, numerous additional reaction pathways result. Among these, the presence of parallel and consecutive reaction channels to CO_x products is of major concern. For this reason, previous efforts to create selective partial oxidation catalysts with high activity have typically fallen below economic feasibility requirements. This thesis focuses on the following alkane-to-alkene transformation reactions:

Oxidative Coupling of Methane (OCM): $2CH_4 + O_2 \leftrightarrow C_2H_4 + 2\ H_2O$
Oxidative Dehydrogenation of Ethane (ODHE): $C_2H_6 + \frac{1}{2}\ O_2 \leftrightarrow C_2H_4 + H_2O$
Oxidative Dehydrogenation of Propane (ODHP): $C_3H_8 + \frac{1}{2}\ O_2 \leftrightarrow C_3H_6 + H_2O$

Regarding OCM, an approach was presented for determining an upper bound on the yield of a catalytic process, which allowed for variations in the catalytic chemistry. Scaling and thermodynamic arguments were used to set parameters of an elementary step surface mechanism at values resulting in optimal yields, subjected only to physical constraints. Remaining unknowns were treated as independent variables and varied over a broad range. The result was a set of thermodynamically consistent mechanisms with optimal kinetics that could be incorporated into reactor-transport models. With this approach, an upper bound on the yield for OCM was computed. Results showed that even with optimal surface chemistry, strict limits existed on the attainable yield. Surface energetics necessary for superior OCM performance were identified and the origins of these requirements elucidated. The resulting upper bound on OCM yield under conventional, packed-bed, continuous-feed operation was found to be 28%.

The catalytic properties of LiCl/sulfated ZrO_2-based catalysts were explored for ODHE. LiCl was shown to strongly interact with the acid sites on sulfated ZrO_2 (SZ),

influencing its catalytic behavior. Two approaches were taken to modify the nature/strength of the LiCl-support interaction. Firstly, $LiCl/Nd_2O_3$-impregnated MoO_x/ZrO_2 and WO_x/ZrO_2 were examined. Unlike SZ, these supports allowed for the tailoring of MoO_x and WO_x surface densities, which in turn drastically altered their ODHE performance. The poor stability of these supports, however, rendered them inferior to SZ. Secondly, the effects of dopant incorporation on the catalytic behavior of $LiCl/MO_x/SZ$ were studied. Si-doped ZrO_2-based catalysts synthesized via the sol-gel method were found to exhibit superior activity, selectivity and stability for ODHE. Sulfate decomposition experiments related the ODHE activity of these materials to the influence of the Si dopant on the sulfate binding strength. The sol-gel synthesis conditions were optimized with respect to sol pH, water:alkoxide ratio and silicon precursor, achieving improved catalyst homogeneity and enhanced ODHE performance. The co-impregnation of 5 wt% Na was found to suppress catalyst deactivation from lithium leaching. CeO_2 was determined to be the optimal secondary metal oxide. Using a $LiCl/NaCl/CeO_2$/Si-doped SZ catalyst (5 wt% Li, 5 wt% Na, 5 wt% CeO_2, Si/Zr = 0.05), conversions of > 92% were achieved, while maintaining ethane selectivities in excess of 83%, giving a maximum ODHE yield of 77%.

ODHP represented another potential application of the upper bound methodology developed for OCM. Scaling and thermodynamic arguments were used in conjunction with reactor data, water desorption kinetics and literature values to develop a thermodynamically and physically consistent model for ODHP. Propene selectivity was found to be very sensitive to the Eley-Rideal and Mars-van Krevelen reactions of allyl species with the surface to form allene. Difficulties in constraining these barrier heights, however, rendered the construction of a strict bound on ODHP infeasible. In addition to simulations, MoO_x/doped ZrO_2 catalysts were synthesized for ODHP. Through dopants, we endeavored to improve the low-temperature propane activity without relying on high surface densities of MoO_x. MoO_x/Nb-doped ZrO_2 catalyst (Nb/Zr = 0.05, 5.0 Mo/nm^2) was shown to exhibit a maximum propene yield of 9.1% vs. 6.1% for the MoO_x/ZrO_2 catalyst. Based on kinetic studies, the performance improvement was traced to a reduction in the difference of the activation energy barriers between ODHP and secondary propene combustion. Conversions over MoO_x/Nb-doped ZrO_2, however, remained lower than those achievable in short contact time or heterogeneous/homogeneous-coupled systems. Catalysts operating at higher temperatures, where homogeneous reaction pathways might play a larger role, were examined in depth, in particular, $LiCl/MO_x$/doped SZ catalysts were tested, since these nanocomposites were found to display superior ODHE activity at lower temperatures. In-doped SZ was found to be a promising support for ODHP, and Nd_2O_3 impregnation was determined to give the optimal selectivity-conversion trajectory. The optimized $LiCl/Nd_2O_3$/In-doped SZ catalyst (5 wt% Li, 5 wt% Nd_2O_3, In/Zr = 0.10) achieved an excellent yield of 24.3% at 600°C.

Thesis Supervisor: William H. Green, Jr.
Title: Associate Professor of Chemical Engineering

Thesis Supervisor: Jackie. Y. Ying
Title: Professor of Chemical Engineering

Acknowledgements

First and foremost, I'd like to thank my parents. As the years pass, I have come to appreciate more and more the enormous sacrifices they have made to make my life as charmed as it is. Their unconditional love and support (and in my mother's case, cooking) have been a bastion of strength and comfort.

Next, I would like to gratefully acknowledge my two advisors, Professors Jackie Y. Ying and William H. Green, Jr. Given their polemic research approaches (I liken them to the "ying" and yang of my Ph.D. experience), they have been enormously flexible in allowing me to pursue my thesis research. The resulting blend of modeling and experiment has provided me with a unique Ph.D. experience for which I am grateful. I continue to be humbled by Bill's vast knowledge of kinetics. His guidance in focusing on the larger scientific issues deserves mention. Even more precious was his gift of time – during my time here his office door has always been open to me. I'd like to thank Jackie for the enormous resources that she provided, and for giving me the creative freedom to pursue my experimental research. I'd also like to thank her for teaching me a great deal about preparation and meticulousness in presenting my research in professional settings. Also, I would like to thank the members of my thesis committee: Professors Karen K. Gleason, Klavs F. Jensen, and Bernhardt L. Trout.

Being a member of two groups has been a privilege, especially with two such creative, intelligent, and dynamic groups as the NMRL and Green group. In particular, I'd like to thank Andrey Zarur, Neeraj Sangar, Edward Ahn, Justin McCue and Jinsuo Xu from the NMRL and Sumathi Raman and Dave Matheu from the Green Group for their valuable insights and assistance. I would also like to thank Susan Lanza and Linda Mousseau for their patience and help with administrative tasks. I am grateful to Alstom Power and the Army Research Office (MURI Program) for financial support of this research.

Perhaps just as valuable as the intellectual contributions of my peers were the emotional contributions of my family and friends that kept me sane. I'd like to thank my two sisters, Yee-Chun and Betty, for "Family Fun Days" on those rare occasions we were all at home. I'd like to thank Binita, for expanding my horizons regarding Berkeley students and vegetarians, and for making the past 5+ years "interesting." I'd like to thank my labmates Pemakorn Pitukmanorom and Mei-Chee Tan for helping make 66-565 a fun, relaxed atmosphere to work. I'd also like to acknowledge a number of friends I've made over the years playing volleyball. In particular, I'd like to thank the members of our IM A/B+ co-ed championship team: Aimee, Manfred, James, Jan, Joanna and Paola.

It has only recently dawned on me that I am finishing my doctorate, and at MIT of all places. In some ways, this is a dream come true for me. As I am about to leave this place, I am thankful for the opportunity to have been here. With that in mind, I'd like to thank Prof. Robert Armstrong for initiating this collaboration between Bill and Jackie. In the end, he was right in the sense that a Ph.D. is more about the journey and not the destination. I feel extremely privileged to have been here. Even more so than the vast resources at my disposal, never in my entire life have I been surrounding by such gifted minds. If I have become a better engineer, it is my surroundings that must take most of the credit.

Table of Contents

List of Figures

List of Tables

List of Symbols

*	Surface species, i.e., O* ≡ surface oxygen species
A_f	Arrhenius pre-exponential factor, forward direction [=] mol, cm, s
A_r	Arrhenius pre-exponential factor, reverse direction [=] mol, cm, s
D	Diffusion coefficient
E_a	Activation energy [=] kJ/mol
E_f	Activation energy, forward direction [=] kJ/mol
E_r	Activation energy, reverse direction [=] kJ/mol
$K_{eq,i}$	Equilibrium constant for reaction i
k_i	Rate constant for reaction i
k_j	Rate constant for reaction $i \neq j$
M	Metal atom
n	Reaction order or Arrhenius temperature order
P	Pressure [=] atm
r	Reaction rate
r_p	Average pore radius [=] nm
R	Universal gas constant
R_0	Tube radius [=] cm
s	Sticking coefficient
T	Temperature [=] °C or K
$X_{RC,i}$	Degree of rate control for step i
z	Axial coordinate [=] cm
Z	Pre-exponential factor
α	Degree of water desorption
β	Heating rate [=] °C/min
θ	Site fraction
τ	Residence time [=] s

Chapter 1 — Background and Research Motivation

1.1 Introduction

Over 90% of natural gas is comprised of methane, ethane and propane. Although used as a fuel, the low value and difficult transportation issues associated with selling natural gas have motivated processes to convert light alkanes into more valuable, easily transportable materials. For instance, the dehydrogenation of ethane to ethene is of considerable interest due to ethene's use as a polymeric and chemical precursor. Recent reports[3] have stated that the present industrial capacity for lower olefins is insufficient to address the growing petrochemical needs. In Western Europe, for example, petrochemical demand is projected to grow annually at 2.4% until 2010. Olefins such as ethene and propylene account for the largest portion of this demand, fueled by a growing market for plastics. According to the American Plastics Council, sales of polyethylene and polypropylene in 2002 grew 4.0% and 6.0%,[1] respectively, with a total annual production of ~ 24 million metric tons.[2]

1.2 Steam Pyrolysis

Light alkenes are traditionally generated through steam pyrolysis of various hydrocarbon feedstocks such as naphtha, ethane, heavy condensates, middle distillates and refinery gas. While naphtha remains and will remain the most important feedstock for petrochemical production, predicted future naphtha shortages due to competing demands (i.e., transportation and aromatic production) will require petrochemical producers to seek both alternative raw materials and processes.[3] Moreover, steam pyrolysis suffers from two major shortcomings. As shown in Figure 1.1, the endothermic nature of this approach requires temperatures in excess of 800°C for favorable thermodynamics. In addition, gradual coke formation on reactor walls necessitates periodic shutdowns and results in sub-optimal operation. To improve performance, efforts have been made to use alloy coatings resistant to coke build-up, to manufacture reactor materials capable of operating under more severe conditions (i.e., higher temperature and shorter residence time), and to develop materials capable of catalyzing these processes at lower temperature.

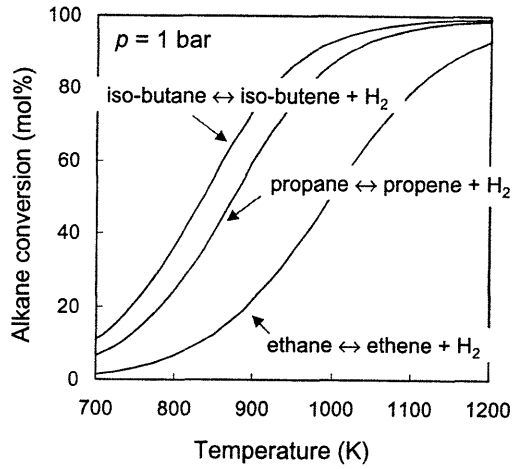

Figure 1.1. Pyrolytic conversion as a function of temperature.[4]

Regarding non-oxidative catalytic dehydrogenation, a few companies such as BASF and Orient Petrochemicals have established commercial operations.[5,6] Although publicly available economic analyses of catalytic dehydrogenation do not exist, the limited commercial interest suggests that these processes are not yet sufficiently profitable. Developments in this area still suffer from the same pitfalls as non-catalyzed pyrolysis. For instance, while platinum-tin/alumina and chromium/alumina catalysts have been found with high initial activity and selectivity for dehydrogenation, these catalysts have been found to quickly deactivate due to coke formation.[7,8,9,10]

1.3 Partial Oxidation

One means by which alkanes may be converted into alkenes is through catalytic partial oxidation. Although our understanding of the surface reaction pathways remains incomplete, the basic framework for partial oxidation consists of the following steps:

$$C_nH_{2n+2} + O^* \leftrightarrow C_nH_{2n+1} + OH^*$$

$$OH^* + OH^* \leftrightarrow H_2O + O^* + V^*$$

$$O_2 + 2V^* \leftrightarrow 2O^*$$

As the alkane feedstock makes contact with the active surface oxygen, hydrogen is abstracted. This facilitates subsequent gas-phase/surface rearrangement of the resulting hydrocarbon into the desired unsaturated product. Newly formed surface hydroxyl groups can combine, releasing water into the gas phase and producing surface vacancies

(V*). Lost oxygen must then be replenished from either the bulk phase or an oxidizing feedstock. Typically, due to the poor oxygen storage capacity of oxides, oxygen is co-fed with the reacting alkane.

Because it addresses both major disadvantages of steam pyrolysis, heterogeneous partial oxidation provides an attractive alternative for alkane-to-alkene conversion. Of particular interest are those reactions involved in ethene and propylene formation. These are the oxidative coupling of methane (OCM), the oxidative dehydrogenation of ethane (ODHE) and the oxidative dehydrogenation of propane (ODHP). With the inclusion of oxygen as a reactant, however, additional reaction channels to unwanted CO_x products are created. Thus, previous efforts to create selective partial oxidation catalysts with high activity have fallen below economic feasibility. Burch and Crab[11,12] have found that in almost all cases, homogeneous yields under oxidative conditions are comparable, if not better, than yields obtained using the best partial oxidation catalysts. As shown in Figure 1.2, a general performance trend exists that as conversion increases, selectivity decreases. In many cases, the sites responsible for catalyzing reactant transformation also react with the desired products. This has been found to be especially problematical in cases where bond energies for products are more than 30-40 kJ/mol lower than reactants.[13] In fact, the inclusion of a catalyst can oftentimes decrease performance, as additional unwanted oxidation channels occur due to unselective surface sites.

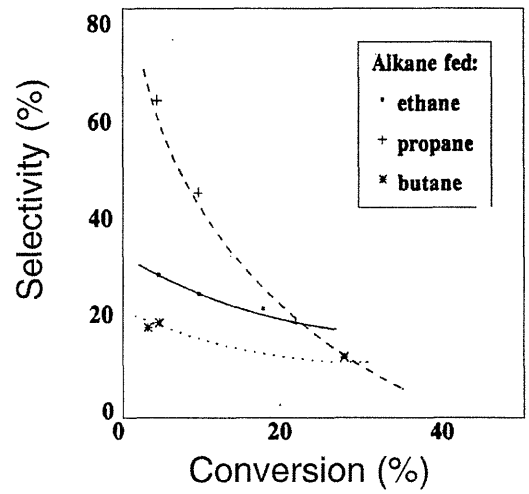

Figure 1.2. Selectivity-conversion profiles of VO_x catalysts for alkane partial oxidation.[14]

1.3.1 Oxidative Coupling of Methane

The search for a heterogeneous OCM catalyst has been described as a modern day search for the philosopher's stone.[15] The reaction involves the conversion of methane to ethane,

$$2\ CH_4 + \tfrac{1}{2}\ O_2 \leftrightarrow C_2H_6 + H_2O,$$

which is followed by a dehydrogenation reaction to form ethene. The initial transformation is believed to occur via an Eley-Rideal mechanism. Challenges faced by all partial oxidation reactions are well illustrated by OCM. The difficulty of successful OCM is that the desired C_2 products – ethene and ethane – are susceptible to further oxidation in parallel and subsequent steps. Hydrogen abstraction from methane is one of the primary roles of the catalyst in heterogeneous OCM. Given the high strength of the methane C-H bond, however, the robust reaction conditions necessary for this step oftentimes result in further reaction of C_2 products. The C-H bonds in methane (~ 450 kJ/mol) are stronger than or on par with those in either ethane (~ 429 kJ/mol) or ethene (~ 475 kJ/mol).[i] Thus, a catalyst capable of activating methane for coupling frequently activates it for complete oxidation as well.

While strongly dependent on ethene valuation, analyses performed by the MITRE Corporation,[16] SRI[17] and Gradassi and Green[18] have placed the minimum values for OCM economic feasibility at ~ 16-30% yield and > 80% selectivity. These economic projections typically assume industrial conditions of elevated pressures and undiluted feedstreams. For simplicity and safety, however, laboratory-scale catalyst screening has focused almost exclusively on exceeding these values in a packed bed reactor operated at atmospheric pressure with dilute feedstreams. Yet even under such favorable conditions, none of the numerous OCM catalysts synthesized since Keller and Bhasin's initial report[19] have managed to be commercially viable. Furthermore, those catalysts that have enjoyed the most success — lithium-based catalysts — have frequently suffered from problems of deactivation or lithium volatilization.

[i] Values calculated at 800°C from NIST Chemistry Webbook data.

1.3.2 Oxidative Dehydrogenation of Ethane

Oxidative dehydrogenation of ethane represents a somewhat "easier" catalytic system to study than OCM, since C-H bond energy is reduced with an increasing number of carbon atoms. As a result, lower reaction temperatures are required, reducing potential problems with catalyst deactivation and unwanted homogeneous reactions. In addition, from a C-H bond energy standpoint, the conversion of ethane to ethene represents the most feasible of the three partial oxidation reactions being studied. The overall reaction is:

$$C_2H_6 + \tfrac{1}{2}\, O_2 \leftrightarrow C_2H_4 + H_2O$$

Under reaction conditions, the C-H bond energy of ethene is ~ 44 kJ/mol higher than that of ethane. Presumably, we could therefore envision a window of opportunity wherein only ethane would significantly react with the catalyst surface. Even with this bond strength differential, however, the ethene π-bond is considered more reactive than the σ-bonds present in ethane. Similar to parallel efforts in OCM and ODHP, efforts to find economical ODHE catalysts have not met with much success.

Many ODHE catalysts have their roots in OCM. Typically, those catalysts that showed high selectivity, but low conversion for OCM[20,43] or displayed poor thermal stability at the higher OCM reaction temperatures were applied to ODHE. Materials such as transition metal oxides,[43] magnesia doped rare-earth oxides,[21] or supported molybdate and vanadate catalysts[22] have been examined. More recently, some researchers have turned towards using CO_2 (instead of O_2) as a mild oxidizing gas to examine supported Ga_2O_3[23] and Cr_2O_3[24,25,26] catalysts. In addition, both alkali halide[21] and chlorine[27] impregnation have been found to further enhance catalytic performance. While suffering from shortcomings (i.e., volatilization), lithium-containing catalysts like LiCl/MgO remain popular in that they have consistently resulted in yields superior to simple or mixed metal oxide catalysts. Moreover, Wang *et al.*[28,29,30] have found that LiCl impregnated on a sulfated zirconia support significantly outperforms LiCl impregnated on alternative supports such as MgO and ZrO_2. Similar to Conway *et al.'s* work on LiCl/MgO systems,[31] additional impregnation of small quantities of metal oxide onto the LiCl/sulfated ZrO_2 catalyst was found by Wang *et al.* to improve conversion without

significantly reducing selectivity. Using a Nd_2O_3/LiCl/sulfated ZrO_2 catalyst, Wang *et al.* [32] managed to obtain sustainable yields of over 77%.

1.3.3 Oxidative Dehydrogenation of Propane

The oxidative dehydrogenation of propane involves the formation of propylene via the reaction:

$$C_3H_8 + ½\ O_2 \leftrightarrow C_3H_6 + H_2O$$

Similar to OCM, ODHP has proven difficult due to the higher propensity for the alkene product to react than the alkane reactant. This can be attributed both to the ease with which propylene adsorbs as well as to the resonance stabilization of the resulting radical.

Based on the results of early screening studies,[33] efforts to develop ODHP catalysts have focused on the use of molybdate and vanadate moieties impregnated on various supports. Thus far, however, even the highest yield catalysts still fail to exceed 30% yield.[34] The most extensive studies of these systems are by Iglesia *et al.*,[35,36,37,38] who have characterized and manipulated parameters such surface density, surface promotion via alkali salt addition, and support to alter the local electronic properties of active sites. They have established that these manipulations result in improved selectivity at the cost of conversion (or vice-versa), and influence the relative rates of propane dehydrogenation versus propylene combustion.

1.4 Research Objectives

Despite the alluring features of heterogeneous partial oxidation, it remains unclear whether catalysts can be synthesized to successfully achieve controlled oxidation. For instance, despite the hundreds (if not thousands) of catalysts screened for OCM, none has managed to exceed the economic viability thresholds. This hints at some fundamental limitation on OCM yields. Alternative reactor/separation schemes have been shown to exceed yield-selectivity targets and may represent the only viable future for OCM.[39,40] But before more elaborate and costly reactor schemes are pursued, the upper limit on yield for a conventional packed-bed, single-pass, continuous-feed operation needs to be fully assessed.

An approach is presented in Chapter 2 for determining an upper bound on the yield of OCM, which allows for variations in the catalytic chemistry. Although the notion of an upper bound for OCM has been explored previously,[41,42] we believe that several reasons warrant a more detailed examination of the problem. To accomplish this, we have constructed "idealized" catalysts using scaling and thermodynamic arguments to set parameters of an elementary step surface mechanism, subject only to physical constraints. Remaining unknowns are treated as independent variables and are varied over a broad range. The result is a set of thermodynamically consistent mechanisms with optimal kinetics that can be incorporated into reactor-transport models to generate yield trajectories. Using this approach, an upper bound on the yield for oxidative coupling of methane (OCM) is computed. Results show that even with optimal surface chemistry, limits exist on the attainable yield. We explore several factors responsible for these limitations. Moreover, surface energetics necessary for superior OCM performance are identified and the origins of these requirements are elucidated.

In Chapters 3 and 4, we focus our attention on synthesizing highly homogeneous nanocomposites via controlled chemical precipitation and sol-gel methods for ODHE and ODHP. For ODHE, we have chosen to study zirconia-based nanocomposite materials, using Wang *et al.'s* Nd_2O_3/LiCl/sulfated ZrO_2 catalyst as a starting point. Since other lithium-supported catalysts have been previously tested with significantly lower yields, we examine the unique interaction between LiCl and the sulfated zirconia support. By doping alternative cations into the zirconia matrix, we then capitalize on this interaction in the hopes of manipulating catalyst activity and selectivity. Subsequent studies investigate the impact of sol-gel synthesis parameters on catalytic performance.

For ODHP, since the C-H bond energy differential between the product and reactant is unfavorable, our research focuses on minimizing propylene adsorption on MoO_x catalysts. Similar to ODHE, we attempt to influence the local electronic properties of the active site by incorporating dopants into the support. The ultimate goal of heterogeneous ODHP has been to operate at low reaction temperatures to promote presumably more selective heterogeneous pathways. Currently, however, the best-reported ODHP yields occur at high reaction temperatures. Under the dilute feedstream conditions that most studies are carried out, it has been argued that the role of

homogeneous reactions is small in such cases.[43] Initiation and selective quenching of homogeneous radical pathways, however, could be one important role of the catalyst. Alongside our efforts to develop low-temperature catalysts for ODHP, we explore the ramifications of gas-phase reactions on ODHP performance at higher temperatures.

1.5 References

[1] American Plastics Council, *2002 Year In Review*, 22 April 2003, <http://ww.w.americanplasticscouncil.org/benefits/economic/03/pips_02_year_review.html> (10 June 2003).

[2] American Plastics Council, *APC Year-End Statistics for 2002*, April 2003, <http://www.americanplasticscouncil.org/benefits/economic/03/YearEnd2002_Stats.pdf > (10 June 2003).

[3] Zehnder, S., *Hydro. Proc.* **Feb.**, 59 (1998).

[4] DelftChemTech, *Industrial Catalysis*, <http://www.dct.tudelft.nl/~wwwrace/st3141a/cpt_04.pdf> (4 February, 2003).

[5] Anon., *Chem. Week* **161**, 32 (1999).

[6] Anon., *Chem. Week* **160**, 23 (1998).

[7] Rebo, H. P., Blekkan, E. A., Bednarova, L., and Holmen, A., *Stud. Surf. Sci. Catal.* **126**, 333 (1999).

[8] Sault, A. G., Martino, A., Kawola, J. S., and Boespflug, E., *J. Catal.* **191**, 474 (2000).

[9] Aguilar-Rios, G., Salas, P., Valenzuela, M. A., Armendariz, H., Wang, J. A., and Salmones, J., *Catal. Lett.* **60**, 21 (1999).

[10] Jablonski, E. L., Castro, A. A., Scelza, O. A., and de Miguel, S. R., *Appl. Catal. A* **183**, 189 (1999).

[11] Burch, R., and Crabb, E. M., *Appl. Catal. A* **100**, 111 (1993).

[12] Burch, R., and Crabb, E. M., *Appl. Catal. A* **97**, 49 (1993).

[13] Cassidy, F. E., and Hodnett, B. K., *CATTECH* **2**, 173 (1998).

[14] Blasco, T., and Nieto, J. M. L., *Appl. Catal. A*, **157**, 117 (1997).

[15] Mortazavi, Y., Hudgins, R. R., and Silveston, P. L., *Can. J. Chem. Eng.* **74**, 683 (1996).

[16] Tomlinson, G. D., *Direct Methane Conversion — An Assessment*, Contractor Report, SAND-88-7110, 1988.

[17] Field, S., Niruta, S. C., and McCarthy, J. G., SRI International, Project Report 6:9129-01-SQ, 1989.

[18] Gradassi, M. J., and Green, N. W., *Fuel Proc. Tech.* **42**, 65 (1995).

[19] Keller, G. E., and Bhasin, M. M., *J. Catal.* **73**, 9 (1982).

[20] Morales, E., and Lunsford, J. H., *J. Catal.* **118**, 255 (1989).

[21] Fuchs, S., Leveles, L., Seshan, K., Lefferts, L., Lemonidou, A., and Lercher, J. A., *Top. Catal.* **15**, 169 (2001).

[22] Watling, T. C., Deo, G., Seshan, K., Wachs, I. E., and Lercher, J. A., *Catal. Today* **28**, 139 (1996).

[23] Nakagawa, K., Okamura, M., Ikenaga, N., Suzuki, T., and Kobayashi, T., *Chem. Commun.* **11**, 1025 (1998).

[24] El-Idrissi, J., Kacimi, M., Bozon-Verduraz, F., and Ziyad, M., *Catal. Lett.* **56**, 221 (1998).

[25] Wang, S., Murata, K., Hayakawa, T., Hamakawa, S., and Suzuki, K., *Appl. Catal. A* **196**, 1 (2000).

[26] Ge, X., Zhu, M., and Shen, J., *React. Kinet. Catal. Lett.* **77**, 103 (2002).

[27] Wang, D., Rosynek, M. P., and Lunsford, J. H., *J. Catal.* **151**, 155 (1995).

[28] Wang, S., Murata, K., Hayakawa, T., Hamakawa, S., and Suzuki, K., *Cat. Lett.* **59**, 173 (1999).

[29] Wang, S., Murata, K., Hayakawa, T., Hamakawa, S., and Suzuki, K., *Chem. Comm.* **2**, 221 (1997).

[30] Wang, S., Murata, K., Hayakawa, T., Hamakawa, S., and Suzuki, K., *J. Chem. Tech. Biotech.* **74**, 988 (1999).

[31] Conway, S. J., Wang, D. J., and Lunsford, J. H., *Appl. Catal. A.* **79**, L1 (1991).

[32] Wang, S., Murata, K., Hayakawa, T., Hamakawa, S., and Suzuki, K., *Cat. Lett.* **62**, 191 (1999).

[33] Chaar, M. A., Patel, D., and Kung, H. H., *J. Catal.* **109**, 463 (1988).

[34] Albonetti, S., Cavani, F., and Trifiro, F., *Catal. Rev.-Sci. Eng.* **28**, 413 (1996).

[35] Chen, K., Xie, S., Bell, A. T., and Iglesia, E., *J. Catal.* **198**, 232 (2001).

[36] Khodakov, A., Yang, J., Su, S., Iglesia, E., and Bell, A. T., *J. Catal.* **177**, 343 (1998).

[37] Barton, D. G., Soled, S. L., Meitzner, G. D., Fuentes, G. A., and Iglesia, E., *J. Catal.* **181**, 57 (1999).

[38] Chen, K., Bell, A. T., and Iglesia, E., *J. Phys. Chem. B* **104**, 1292 (2000).

[39] Jiang, Y., Yentekakis, I. V., and Vayenas, C. G., *Science* **264**, 1563 (1994).

[40] Androulakis, I. P., and Reyes, S. C., *AIChE J.* **45**, 860 (1999).

[41] Labinger, J. A., *Catal Lett.* **1**, 371 (1988).

[42] Labinger, J. A., Ott, K. C., *J. Phys. Chem.* **91**, 2682 (1987).

[43] Kennedy, E., and Cant, N. W., *Appl. Catal. A* **75**, 321 (1991).

Chapter 2 – A Theoretical Upper Bound on the Oxidative Coupling of Methane

2.1 Background

Motivated by earlier failures to synthesize economically viable OCM catalysts, previous researchers have explored the notion of a fundamental upper bound on OCM performance. At the core of many of such efforts is the development of an elementary-step surface mechanism. Upon acquiring experimental data for a particular OCM catalyst, Arrhenius pre-exponential factors and activation energies are adjusted to fit experimental results.[1,2] Once established, these kinetic mechanisms are utilized in reactor design optimization algorithms to maximize yield. Since optimization is performed with fixed chemical kinetics, this maximum is constrained by the quality of the catalyst used in developing the kinetic mechanism. The unintentional result is the de-emphasis of the catalyst's role in obtaining high yields. This is greatly at odds with experimental conclusions, which have often linked catalyst performance to the relative rates of surface reactions.

An early attempt at determining a bound on OCM yield was undertaken by Labinger.[3] In his paper, Labinger solves a set of ordinary differential equations derived via a pseudo-elementary reaction mechanism to ultimately chart methane conversion vs. C_2 selectivity. In this model, the surface irreversibly reacts with CH_4, CH_3, C_2H_6, C_2H_4, and C_3+ species. Initial rate parameter estimates for his mechanism are derived from experimental data for a mixed Mn-Mg oxide catalyst.[4] By manipulating select rate constants to advantageous values consistent with other experimental catalytic data, Labinger sets an upper bound of 30% yield (at 1 atm methane partial pressure) for the case where methane and oxygen react separately with the catalyst.

Recently, several issues have been brought to light that warrant re-examining Labinger's upper bound. First, because both heterogeneous and homogeneous steps are necessary for C_2 formation, mass transfer is believed to play a potentially significant role in the OCM yields obtained. Couwenberg *et al.*[2,5] identified irreducible mass-transfer limitations on surface generated reactive intermediates such as methyl radical, whose lifetimes are short compared with the transport time-scale. The resulting concentration gradients facilitate second-order processes such as methyl radical coupling to form C_2

species, increasing the yield. It is not possible to capture this effect with an ordinary differential equation model (CSTR or PFR); a 2-D or 3-D simulation is necessary.

Secondly, at the high temperatures needed for OCM, $O_2(g)$ will be present above the regenerable metal oxide catalyst. This being the case, an industrial OCM process will probably co-feed methane and oxygen to avoid reduction of the catalyst. The presence of $O_2(g)$ introduces many additional complications as it will also quickly undergo reaction with gas-phase radicals, significantly affecting the selectivity and yield. Here we establish the yield limit for a co-fed CH_4/O_2 system rather than the two-stage system studied by Labinger.

The intricate balance between the need for gaseous oxygen in catalyst activation and its detrimental role in gas-phase oxidation contradicts the notion of simply treating the catalyst as a methyl radical generator. A number of additional interactions occurring between the gas phase and the catalyst surface deserves further attention because of the intimate coupling of heterogeneous and homogeneous reactions. Beyond its role in methyl radical generation, the catalyst has been shown to serve as a radical quencher. This removal of detrimental/beneficial gas-phase species can significantly alter the conversion-selectivity trajectory.

Finally, although OCM has long been thought to occur via a catalytic cycle, researchers have largely focused on only one step in this cycle: reducing the activation energy for hydrogen abstraction from methane. However, for very active catalysts, alternative bottlenecks could be present. For instance, acceleration of hydrogen abstraction typically requires increasing the stability of the resulting surface hydroxyl species. If pushed to extremes, these surface hydroxyls could effectively act as poisons. Understanding the limited combinations of surface energetics that allow for optimum throughput in the catalytic cycle could provide catalyst developers with both a clear target and a tool for screening catalysts.

2.2 Approach

2.2.1 Overview

Since our goal is to determine whether a fundamental upper bound on OCM yield exists, instead of fixing surface chemistry parameters to match one particular catalyst, we

have computed the OCM yield of a range of conceivable catalysts. OCM is a model case study for this approach in that, despite the large number of catalysts examined, a fairly unified surface mechanism has been set forth. The key catalytic cycle consists of a small number of elementary reactions, minimizing the dimensionality of the search space. In each case, beneficial surface reaction rates are set at the upper limit of what is physically achievable. While large uncertainties exist in any one set of experimentally derived kinetic parameters, some of the limits of catalyst behavior are well known (e.g., the energetics of oxygen adsorption/desorption on metal oxides, diffusion limits on reaction rates). Surface thermochemistry immediately provides a bound on kinetics. Thanks to improvements in computational speed, the use of detailed multicomponent transport models coupled with elementary surface reaction mechanisms is now practical. As shown later, even if one could synthesize a catalyst where all desired reaction rates were maximized and all surface species had optimal thermochemistry, the OCM yield would still be significantly restricted by fundamental thermodynamic and transport limitations.

2.2.2 Reaction Mechanism

Gas-phase rate constants and thermodynamic property data were taken from a library of reactions compiled previously by Mims *et al.*[6] This homogeneous model contains almost 450 reversible elementary chemical reactions and 115 species. Here we assume the detailed gas-phase chemistry model is accurate, and focus on the surface kinetics of our hypothetical ideal catalysts. Similar to previous models,[5,7] the elementary surface mechanism used is shown in Table 1. Reaction (1) describes the one-step dissociative chemisorption of oxygen. The resulting activated oxygen serves to abstract hydrogen from methane in reaction (2) via an Eley-Rideal mechanism, generating methyl radicals that then couple in the gas phase. To complete this catalytic cycle, two surface hydroxyls combine to form water in reaction (3), regenerating a vacancy site in the process.

In addition to these steps, reactions (4)-(7) describe hydrogen abstraction from the major products. Inclusion of these reactions undoubtedly reduces yields, yet the lower/similar C-H bond energies of ethane, ethene, methanol, and formaldehyde make these species as susceptible to hydrogen abstraction as methane. We assume that at OCM

Table 2.1. Proposed mechanism for OCM[†]

Reaction	A_f[‡]	E_f (kJ/mol)	A_r	E_r (kJ/mol)
(1) $O_2 + 2V^* \leftrightarrow O^* + O^*$	1.63E+22	0.00	2.39E+19	250.00
(2) $CH_4 + O^* \leftrightarrow CH_3\bullet + OH^*$	1.85E+13	125.00	1.91E+13	0.00
(3) $OH^* + OH^* \leftrightarrow H_2O + O^* + V^*$	2.25E+19	0.00	2.17E+22	5.59
(4) $C_2H_6 + O^* \leftrightarrow C_2H_5\bullet + OH^*$	1.35E+13	103.80	1.37E+13	0.00
(5) $C_2H_4 + O^* \leftrightarrow C_2H_3\bullet + OH^*$	1.40E+13	149.71	1.42E+13	0.00
(6) $CH_2O + O^* \leftrightarrow CHO\bullet + OH^*$	1.35E+13	61.74	1.37E+13	0.00
(7) $CH_3OH + O^* \leftrightarrow CH_3O\bullet + OH^*$	1.31E+13	108.00	1.33E+13	0.00
(8) $HOO\bullet + O^* \leftrightarrow O_2 + OH^*$	1.29E+13	0.00	1.31E+13	138.78
(9) $HOO\bullet + V^* \leftrightarrow HO\bullet + O^*$	1.29E+13	0.00	1.80E+13	110.51
(10) $CH_3OO\bullet + 2V^* \leftrightarrow O^* + OCH_3^*$	1.34E+22	0.00	1.72E+19	386.76
(11) $CH_3OO\bullet + V^* \leftrightarrow O^* + CH_3O\bullet$	1.08E+13	0.00	1.33E+13	149.49
(12) $CH_3\bullet + O^* \leftrightarrow CH_3O^*$	1.91E+08	0.00	2.24E+13	233.28
(13) $CH_3O^* + X\bullet \leftrightarrow XH + CH_2O + V^*$	[++]			
(14) $CH_3O^* + O^* \leftrightarrow OH^* + CH_2O + V^*$	1.72E+19	5.96	1.69E+19	0.00

[†] A-Factor and E_a values shown are for the case where ΔH_{ads} = -250.00 kJ/mol and ΔH_{abs} = 125.00 kJ/mol. These are the optimal kinetic parameters for OCM performance as determined by the yield map in Figure 2.3.
[‡] A-Factors in cm, mole, s units.
[++] A-Factors and E_a values are dependent on the abstracting gas-phase species.

temperatures, the surface interacts with these species in a manner similar to how it reacts with methane. As a partial proof of their necessity, previous simulations done by Hargreaves, Hutchings and Joyner found that failure to include reaction (6) resulted in concentrations of formaldehyde that were never experimentally observed.[8]

The appropriateness of assuming comparable hydrogen abstraction rates from C-H bonds with similar strengths may come into question given the experimentally observed rate constants for methane versus ethene combustion. Shi, Rosynek and Lunsford,[9] through isotope labeling experiments, have determined that for several OCM catalysts, the overall rate for ethene combustion is ~3-5 times larger than that for methane

combustion. This may seem surprising, since the C-H bond energy for ethene is greater than for methane. When considering the overall rates for the combustion of methane and ethene, however, we must consider the fact that this process involves several elementary reactions. Following hydrogen abstraction, the resulting methyl and vinyl radical species must undergo further reaction to form CO_2. Unlike vinyl radicals, which are known to react very quickly with $O_2(g)$ to form CO_x precursors, methyl radicals are relatively unreactive with O_2.[6] The initial methyl-O_2 adduct is unstable at OCM temperatures and falls apart back to methyl and $O_2(g)$. Our calculations also suggest that surface-mediated routes from CH_3 to CO_2 often involve an endothermic reaction. Thus, it is not surprising that ethene is converted to CO_x more rapidly than methane, even though the rate of the first step is not very different.

While the main function of the catalyst is to act as a source for radical species, several researchers have discussed the radical quenching abilities of solid surfaces.[10,11] Such quenching reactions may provide a means for the removal of detrimental gas-phase species and thus inhibit negative gas-phase reaction channels. Peroxy species have been shown to facilitate undesirable gas-phase deep oxidation pathways.[6,12] Therefore, we have also included what we consider to be the major surface-mediated peroxy radical quenching reactions (reactions (8)-(11)). These reactions either involve a very fast H abstraction or cleavage of the very weak peroxide bond.

One aspect of the surface mechanism that is not clear is the role of the catalyst in heterogeneous deep oxidation. Many researchers have speculated about such pathways, but a great deal of debate still exists as to the appropriate treatment of such pathways.[13] Deep oxidation products are often blamed on the presence of unselective, surface adsorbed oxygen species that have not had time to be incorporated into the oxide lattice.[7] In addition, unwanted secondary reactions of ethene, such as reaction of the ethene double bond with the surface, also eventually lead to deep oxidation products. Both of these heterogeneous reaction pathways result in lower C_2 yields. Since our ultimate goal is to obtain an upper bound on the OCM yield, however, we have limited the heterogeneous contribution to deep oxidation only to indirect pathways. Perhaps the most critical examples of indirect deep oxidation involve secondary reactions of ethane and ethene. Surface-mediated hydrogen abstraction from these species results in radicals

that then degrade via gas-phase channels to CO_x species. Even under ideal circumstances, this is unavoidable and plays a large role in limiting OCM yields. Thus, such steps have been included in the surface mechanism in the form of reactions (4)-(5).

Indirect, surface-mediated deep oxidation pathways were also considered in the treatment of surface methoxy species. From an energetic standpoint, we expect the collision of methyl radicals with the catalyst to favor methoxy formation (reaction (12)). Such intermediate species have been observed in related, lower temperature reactions involving methanol and methane. *In situ* DRIFT studies of OCM over lanthana catalysts, however, detected only trace amounts of these species under reaction conditions.[13] Thus, we hypothesize that surface methoxy species are unstable at high temperature, either dissociating or being quickly subjected to further degradation. Examination of methoxy degradation routes in lower temperature partial oxidation reactions provides some clues. *In situ* DRIFT studies by Li *et al.*[14] on the decomposition and adsorption products of methanol and formaldehyde on CeO_2 found that methoxy species degrade in the following sequence of reactions:

$$CH_3O \rightarrow HCOO \rightarrow CO_2 \text{ (adsorbed carbonate)}$$

Surface formaldehyde is an intermediate in this process. In certain cases, this sequence appears to terminate before carbonate formation. Selective partial oxidation catalysts such as MoO_3/SiO_2 have been found to convert methane to formaldehyde with high selectivity without any evidence of surface carbonate.[15] Yang and Lunsford theorized that the rate of formaldehyde desorption from the surface was rapid enough to prevent formaldehyde degradation.[15] Perhaps this is one reason why MoO_3 species have been found to have superior performance in partial oxidation reactions. Under ideal circumstances, we assume that surface methoxy species are converted to formaldehyde through reactions (13) and (14). Upon formation, formaldehyde is quickly desorbed from the surface.

Having developed an *a priori* surface mechanism, both Arrhenius pre-exponential factors and activation energies were needed to specify the forward and reverse rate constants. To set an upper bound on catalyst activity, no additional barriers to reaction were considered beyond those required by thermochemistry. Thus, in the case of

endothermic reactions, the activation energy was set equal to the enthalpy of reaction, while exothermic steps were assumed to have no barriers.

For steps involving gas molecules striking the surface, upper-bounds on the Arrhenius pre-exponential factors were calculated using collision theory. Pre-exponential factors for reactions involving only surface species were determined using simplified transition-state arguments.[16] To set an upper bound on catalyst turnover, sticking coefficients were initially set to unity. The only exception to this was the reaction of methyl radicals with the catalyst surface. Lunsford *et al.*[17] have presented evidence suggesting that the sticking coefficient for methyl radicals on good OCM catalysts is significantly less than unity, approximately 10^{-7}. As shown later, an ideal OCM catalyst would certainly not have a collision-controlled rate for this detrimental reaction.

Given the number of surface reactions, this approach appears to result in a dauntingly large multidimensional search space. We will show however, through a variety of arguments, that the number of truly independent reaction enthalpies is relatively small. A brief description of the methodology is given below. For additional details please refer to Appendix 2-A. The enthalpy associated with reaction (1) was the first of two independently specified reaction enthalpies. A range of oxygen adsorption enthalpy values spanning -75 to -300 kJ/mole was examined, which includes and extends literature values obtained for oxygen adsorption on a wide variety of metal oxides.[18] Enthalpies for this reaction were examined at fixed intervals of 25 kJ/mole. Similarly, the enthalpy for reaction (2), the hydrogen abstraction reaction of methane, was independently fixed at 25 kJ/mole increments in the range of 75 to 200 kJ/mole. This broad range centers around the average hydrogen abstraction energy for Li/MgO[19] and Li/Sn/MgO,[5] two of the most active and well-characterized OCM catalysts to date. By independently setting the values of reactions (1) and (2), the reaction enthalpy associated with reaction (3) is automatically fixed according to the thermochemistry of the overall catalytic transformation of methane and oxygen to methyl radicals and water.

Upon specifying the enthalpy of methane hydrogen abstraction, the remaining barriers for ethane, ethene, formaldehyde and methanol were scaled according to the difference in C-H bond energy of these species relative to methane. To distinguish the bond energies of MO-H versus MO-CH_3, the differences in bond strength for several

hydrocarbon species of the type RO-H and RO-CH_3 were compared.[20] Finally, surface formaldehyde was assumed to desorb from the surface with no barrier.

Altogether there are 5 surface species whose thermochemistry is unknown. One of these is fixed by the requirements of thermodynamic consistency, one is set relative to the energy of OH* by analogy, one is set by defining the zero of energy, and two are allowed to float within a physically reasonable range. To fully span the two-dimensional mesh of surface species thermochemistry as defined above requires a total of 60 independent calculations.

2.2.3 Model Formulation

As a first approximation of flow through a packed bed, the bed was visualized as a series of parallel, non-interacting, isothermal cylinders. These cylinders were considered lined with our hypothetical catalyst, and intraparticle microporosity was ignored. To maximize catalyst site density, a cubic crystal structure was examined where all exposed surface oxygen atoms were assumed to be potentially active sites for OCM. The resulting site density was calculated to be ~ 1×10^{-9} mole/cm^2. Site densities from other crystal structures are comparable.

To maximize methyl radical production, the smallest allowable pipe diameter was desired to increase the surface-to-volume ratio of the pipe and hence the heterogeneous phase contribution. The cylinder diameter (0.02 cm) was determined by averaging the resulting void space of typically meshed particles (20-60) employed in OCM tests. As with most laboratory-scale OCM experiments, simulations were performed at 1 atm. The flow velocity was fixed at 5.25 cm/s. Higher velocities were avoided as they are typically observed to result in pressure drops during packed bed studies. Cylinder length was not fixed, but adjusted to maximize the yield for each hypothetical catalyst and reaction condition.

Using the various surface kinetic models described earlier, the typical range of packed bed conditions was simulated to find a maximum yield. Specifically, temperatures ranging from 700 to 800°C were examined, with methane to oxygen molar feed ratios of 2:1 to 10:1. Similar to experimental catalyst screening conditions, a dilute feedstream of 15% reactants was employed. The series of equations describing multi-

component transport and chemical reaction occurring throughout the catalyst-lined cylinder was solved using the commercial modeling package, CRESLAF™.[21] This solves the conservation equations for momentum, species and energy in a two-dimensional channel, assuming laminar flow, neglecting axial diffusion and utilizing the ideal gas law as the equation of state. A more detailed discussion of the formulation can be found in either the CRESLAF™ manual[21] or in the publications of Coltrin *et al.*[22,23] Concentration profiles output from CRESLAF™ simulations were used in calculating methane conversion and C_2 selectivities down the catalyst bed. Yields versus axial position were then calculated, and the maximum yield was selected in forming yield maps. As mentioned earlier, CRESLAF™ was utilized to capture the potentially significant effects of radial gradients in radical concentration. For comparison, calculations were also made with a plug flow approximation using PLUG™.[21]

2.3 Results and Discussion

2.3.1 Yield Bounds for Non-Porous OCM Catalysts

Maximum yields of the aforementioned subspace of surface energies were tabulated in yield maps such as Figure 2.1. Results displayed are for reactor conditions of T = 800°C and CH_4:O_2 = 2:1, as these conditions were found to result in the highest yields. Even under the most optimal set of surface energies, however, the maximum yield only approaches 12%. In contrast, yields cited for superior OCM catalysts exceed 20%.

Several possible explanations exist for this discrepancy. One possibility is that the elementary mechanism does not accurately represent the surface kinetics of high-yield OCM catalysts. An alternative mechanism, such as one that differentiates between oxygen species, may be more appropriate. Assuming the kinetic mechanism employed is correct, however, another potential pitfall is the inadvertent maximization of a negative reaction channel. We do not believe this is the case. With respect to the main catalytic cycle, our belief is that high OCM yields are attained via rapid catalytic turnover. The generation of a high methyl radical concentration should promote coupling to C_2 species over deep oxidation. This is due to the second-order nature of the coupling reaction. One area where the reduction of activation energies to enthalpic values was presumably sub-

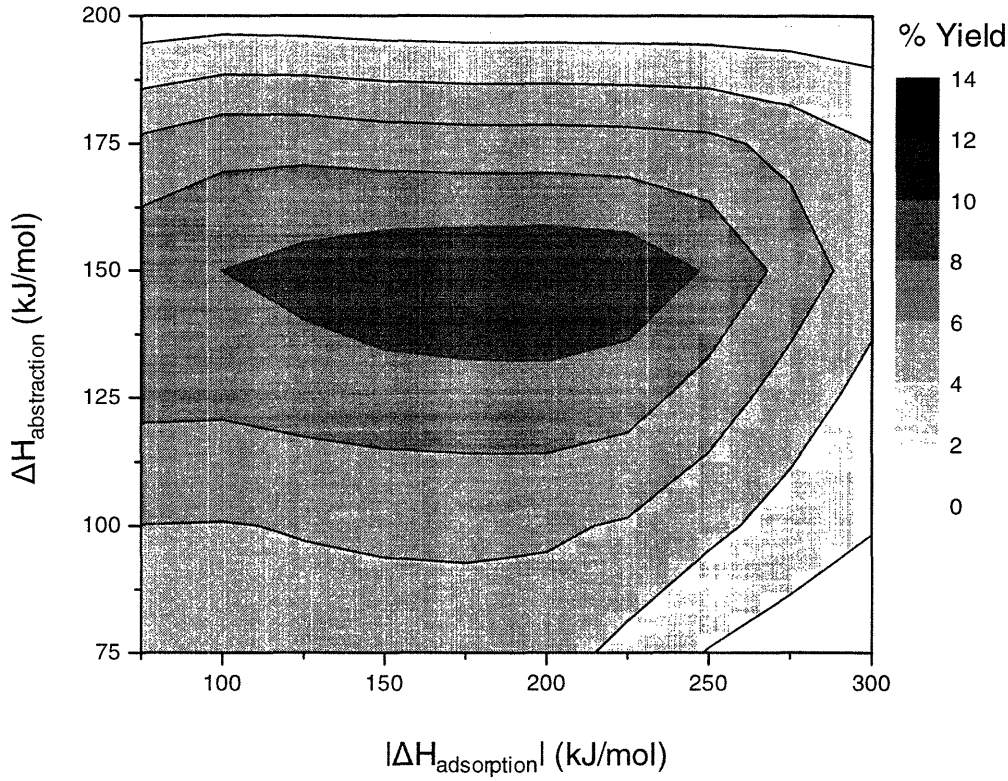

Figure 2.1. OCM yield bound map for a non-porous catalyst as determined by an axisymmetric, multicomponent reacting flow simulation. Each grid point represents a single simulation performed using a specific set of surface reaction parameter values. The various parameter sets employed are generated through independent selection of O_2 dissociative adsorption enthalpy (reaction (1)) and CH_4 hydrogen abstraction enthalpy (reaction (2)) in the main OCM catalytic cycle. Details are given in Section 2.2. T = 800°C, P = 1 atm, CH_4:O_2:N_2 feed ratio = 2:1:17.

optimal was in reaction (14), the conversion of surface methoxy species to formaldehyde. Concern regarding the over-expression of this reaction prompted examining the effects of removing this reaction pathway. The resulting impact on C_2 yield, however, was found to be minor. While rate-of-production analysis shows reaction (14) to be the primary surface channel for the formation of formaldehyde, its impact is ameliorated by the low formation rate of surface methoxy species. Finally, the influence of various radical-quenching reactions was also evaluated. As shown later, manipulations of the sticking coefficients for these reactions indicate that the optimal kinetic parameters were used.

The source of the yield discrepancy can likely be attributed to some oversimplification, whether physical or kinetic, of the real packed bed. For example, non-homogeneity in temperature as well as in catalyst surface undoubtedly has a

significant impact on the resulting yield trajectory. One important cause of the lower-than-expected yields is the geometric constraint imposed on the model. By modeling the system as a series of catalyst-lined pipes, the bulk of catalyst sites provided by porosity is neglected. As a first attempt to take into account this phenomenon, transport effects within the pores themselves were ignored and the surface site densities were simply increased. Barring the possibility of selective transport such as oxygen sieving, it is believed that this should provide an upper bound on what really occurs in porous catalysts.

2.3.2 Model for Microporous Packed-Bed Catalysts

To approximate the extent to which microporous networks could contribute to catalyst active sites, we employed a geometric argument based on a sphere-packing model of catalyst particles.[24,25] The sieved particles constituting the packed bed were assumed to consist of agglomerated networks of non-porous microspheres. Assuming microspheres of a given uniform size, the number of microspheres making up the sieved particle can be calculated. From this, the total surface area of the sieved particles is determined.

As expected, reducing the microsphere size results in increased total surface area. Constraints exist, however, as to the area that may be effectively utilized for OCM. The effective surface area cannot be simply increased by selecting smaller and smaller microspheres. Reyes and Iglesia[25] have shown that for a uniform agglomerate of microspheres, the average pore radius is roughly half that of the microsphere radius. This average pore diameter must exceed the methyl radical mean free path to allow significant methyl radical coupling in the gas phase to form the C_2 products. Under the reaction conditions studied, the mean free path is approximately 200 nm. In addition, coupled products such as ethene, once formed, must diffuse out of the particle without further reaction with the surface (otherwise they will be converted to CO_x products). To determine the particle shell thickness wherein OCM can take place without destruction of the ethene produced, we employ a random walk argument. The mean time for a randomly formed ethene molecule to contact the pore wall is approximated by $(2r_p)^2/12D$ where r_p is the average pore radius and D is the diffusion coefficient of ethene. This time

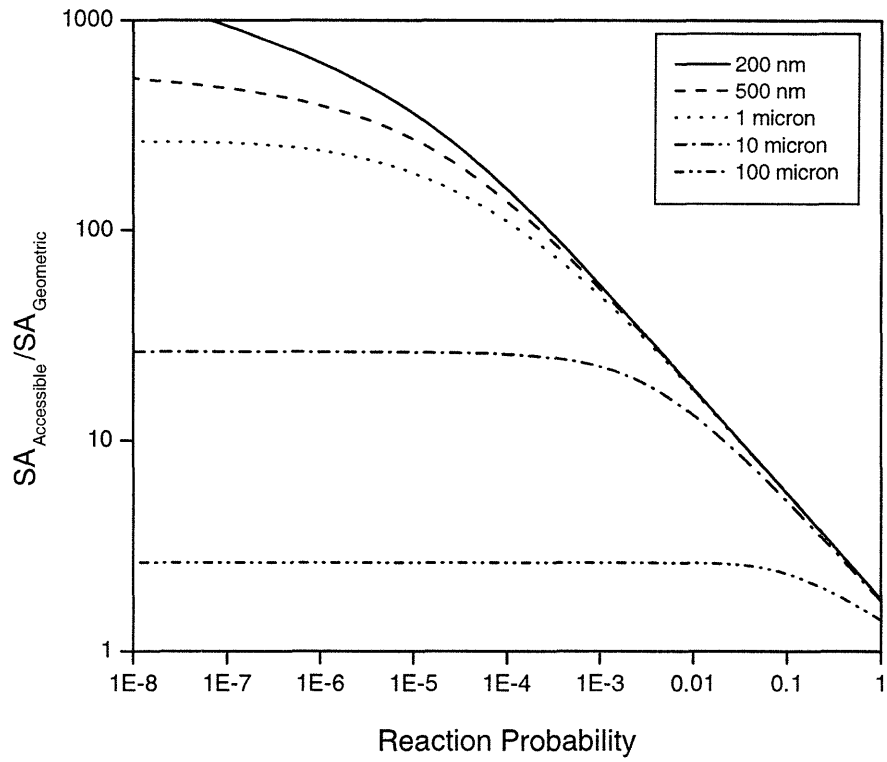

Figure 2.2. Impact of microsphere size on accessible pore surface area of sieved particles. Smaller particles show significant enhancement of accessible surface area with decreasing ethene reaction probability. In our model, the reaction probability is ~ 10^{-5}, so microporosity can increase the effective surface area by two orders of magnitude. Bed void fraction = 0.2, particle porosity = 0.3.

is then scaled via the inverse of the reaction probability of ethene with the surface. This estimates the average time elapsed prior to ethene reaction. Using this value of time, the mean square distance that ethene molecules can travel in the pores before being consumed can be calculated. Thus, an estimate of the thickness of the particle shell that can be utilized effectively for OCM may be obtained. Figure 2.2 shows the ratio of the accessible surface area to the geometric surface area of the pipe. As expected, since the time before wall reaction increases with the square of the pore diameter, ethene can safely diffuse out of particles made of large microspheres. However, the size of the microspheres then limits the gain in surface area. The effectiveness of particles composed of small microspheres is strongly influenced by the reaction probabilities of the molecules being examined. With low reaction probabilities, the accessible number of sites inside the particles is much larger than that of the geometric surface area. With a

barrier of 100 kJ/mole for ethene surface abstraction at 800°C, the reaction probability of ethene is ~ 1.4×10^{-5} per collision with the surface. This results in a maximum effective surface area that is two orders of magnitude larger than the geometric surface area used in computing Figure 2.1.

2.3.3 Yield Bounds for Microporous OCM Catalysts

To simulate the contribution of this additional surface area, the original site density was increased by two orders of magnitude such that the total number of active sites was conserved. As shown in Figure 2.3, OCM yields of up to 28% may be obtained. While modification of the site density to capture internal micropore contributions is a rough approximation, it is interesting that the consequent upper bound is comparable to yields reported for the best experimental OCM catalysts.

One important result from Figure 2.3 is that superior yields are observed only within a narrow window of catalyst thermochemistries. This contradicts earlier predictions that the catalyst plays a minor role in determining OCM performance.[1,26] While the unavoidable secondary reactions of ethane and ethene undeniably shape the maximum yields attainable, Figure 2.3 testifies to the uniqueness of each catalyst in determining that ultimate bound. The fact that maximized yields occur under conditions where the methane hydrogen abstraction energy is not minimized raises an important possibility. While two of the three critical reactions in the main catalytic cycle can be independently fixed, the energetics of the third reaction is constrained by thermodynamics. This interconnectedness complicates the notion of rational catalyst design. For instance, the ease with which a material adsorbs oxygen has a profound effect on how easily water can be desorbed. Targeting efforts exclusively to improve a single catalyst feature (e.g., hydrogen abstraction) may simply result in bottlenecks from other surface reactions.

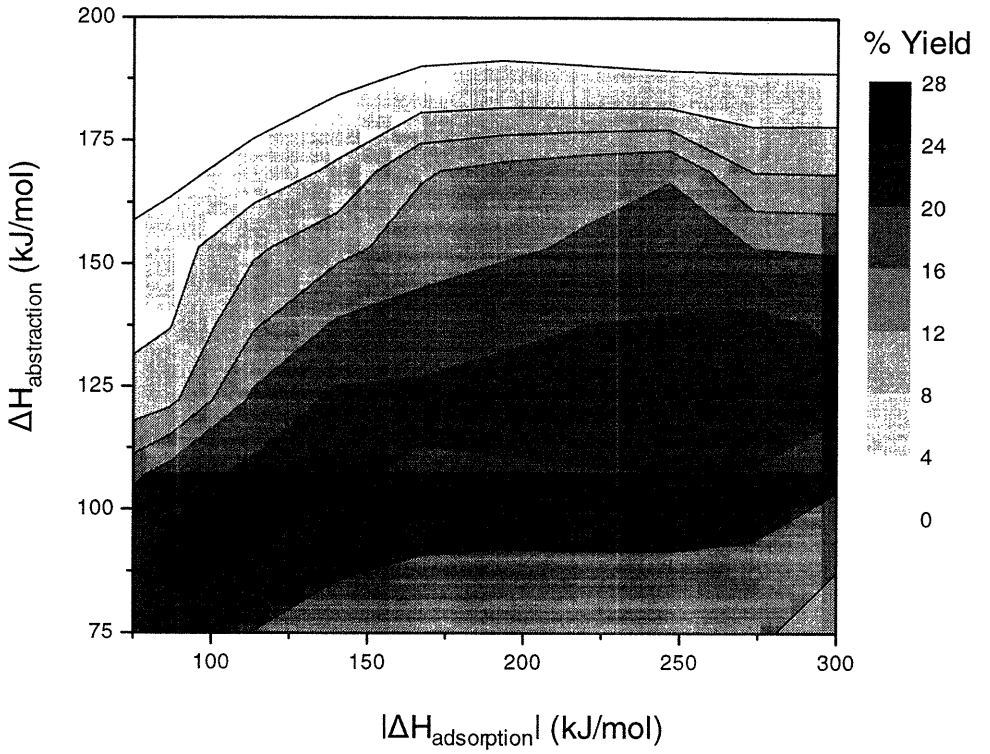

Figure 2.3. OCM yield bound map with 100 times the effective site density used in Figure 2.1 (to model the increased surface area due to microporosity). Other parameters used are identical to those employed in generating Figure 2.1.

2.3.4 Reaction Pathway Analysis

To test this hypothesis, the main catalytic cycle was analyzed via Campbell's degree of rate control.[27] $X_{RC,i}$, the degree of rate control for step i, is defined as:

$$X_{RC,i} = \frac{k_i}{r}\left(\frac{\delta \mathrm{r}}{\delta k_i}\right)_{K_{eq,i},k_j}$$

where r is the overall rate of the catalytic cycle, k_i and $K_{eq,i}$ are the forward rate constant and equilibrium constant for step i, respectively, and k_j's are the rate constants for the remaining steps. Implementation of this method was done numerically. MATLAB™ was used to solve the steady-state rate equations in the main catalytic cycle for site fraction values. The site fractions obtained from this simplified model corresponded quite well to values obtained via PLUG™ and CRESLAF™ calculations at a fraction of the computational cost. The influence of each step on the overall rate was then

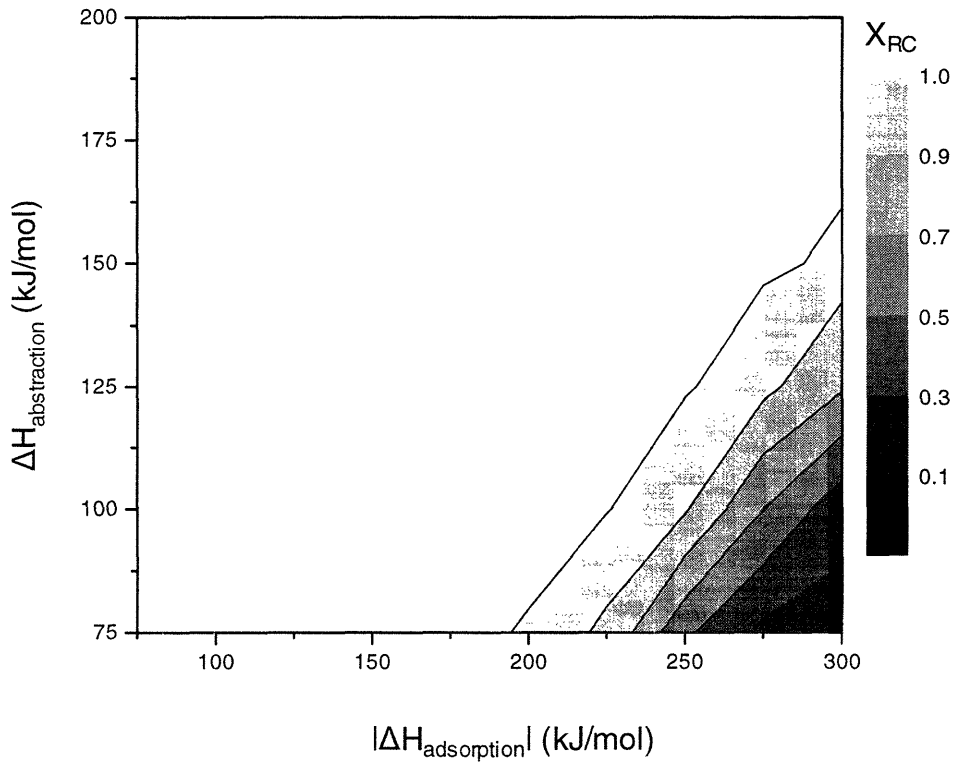

Figure 2.4. Contour map of potential rate-limiting behavior by surface methane hydrogen abstraction (reaction (2)) using Campbell's degree of rate control method. Reaction (2) is rate-controlling in almost all cases.

determined by increasing the values for both k_i and k_{-i} by a small factor and recalculating the steady state rate. This was repeated using smaller incremental increases until the true differential limit was approached.

Figure 2.4 shows the resulting X_{RC} values for the methane hydrogen abstraction reaction (reaction (2)) of the main catalytic cycle. In almost all cases, hydrogen abstraction was found to be rate-limiting. At low $\Delta H_{abstraction}$, however, increases in $|\Delta H_{adsorption}|$ result in the appearance of an alternative rate-limiting step. This effect, however, is only important in the lower right-hand corner of Figure 2.3, on the fringes of catalytic performance and does not explain why the computed OCM yield drops off in the range of $\Delta H_{abstraction} < 125$ kJ/mole and $-100 > \Delta H_{adsorption} > -250$ kJ/mole. In fact, hydrogen abstraction remains the rate-determining surface reaction throughout this region, which would seem to imply that further reductions in the hydrogen abstraction barrier would result in even greater methyl radical production. This is indeed the case. At $\Delta H_{adsorption} = -200$ kJ/mole, as $\Delta H_{abstraction}$ is decreased from 125 kJ/mole to 75 kJ/mole,

approximately two orders of magnitude increase in the methyl radical formation rate is observed. Overall C_2 yields, however, drop from 26.4% to 17.6%. The contradiction between high methyl radical production and low overall OCM yield hints at the onset of a new channel that competes with gas-phase methyl radical coupling. To quantify the consumption channels for methyl radicals, small sections of the catalyst-lined pipes were analyzed using Chemkin's AURORA™ CSTR model.[21] This allowed for the convenient extraction of reaction sensitivity and production rate values. To mimic the 2-D model system, catalyst surface area-to-volume ratios were maintained. A cross-section of abstraction enthalpies was studied at $\Delta H_{adsorption}$ = -200 kJ/mole using gas and surface mole fraction inputs obtained from earlier CRESLAF™ simulations. Small residence times (τ = 10^{-2} s, 10^{-3} s) were selected for CSTR simulations to take snapshots of behavior at different points along the catalyst-lined pipe. Since the axial length scale for reaction changes with $\Delta H_{abstraction}$ (reactants are converted to products in a much shorter distance at low $\Delta H_{abstraction}$), changes in production/consumption channels were compared at z values of identical conversion.

At 20% conversion, when $\Delta H_{abstraction}$ = 150 kJ/mole, methyl radical consumption is dominated by gas-phase coupling to form ethane. This reaction channel accounts for ~ 55% of methyl radical consumption. Several additional gas-phase consumption channels are also present, such as $C_2H_6 + CH_3 \rightarrow C_2H_5 + CH_4$ and $CH_3 + O_2 \rightarrow CH_3OO$, which account for ~ 10% and ~ 9% of CH_3 consumption. Under these conditions, the surface reaction, $OH^* + CH_3 \rightarrow CH_4 + O^*$, accounts for only 12.6% of the methyl radicals consumed. As $\Delta H_{abstraction}$ is reduced, however, this surface reaction becomes increasingly important. At $\Delta H_{abstraction}$ = 125 kJ/mole, $OH^* + CH_3 \rightarrow CH_4 + O^*$ consumes ~ 48% of the methyl radicals produced, increasing further to 92.6% and 99.2% at $\Delta H_{abstraction}$ = 100 kJ/mole and 75 kJ/mole, respectively. In some cases, this reverse reaction is accelerated to a degree such that reaction (2) becomes quasi-equilibrated. For $\Delta H_{abstraction} < 125$ kJ/mole and larger $|\Delta H_{adsorption}|$ values, an analysis of the reversibility of reaction (2) reveals values approaching 1.[28] The appearance of this surface reaction as a significant competitive channel for CH_3 consumption is not due to a change in its activation energy, which remains fixed in our model at 0 kJ/mole. Instead, as Figure 2.5 shows, the steady-state population of OH* rises dramatically as $\Delta H_{abstraction}$ is decreased,

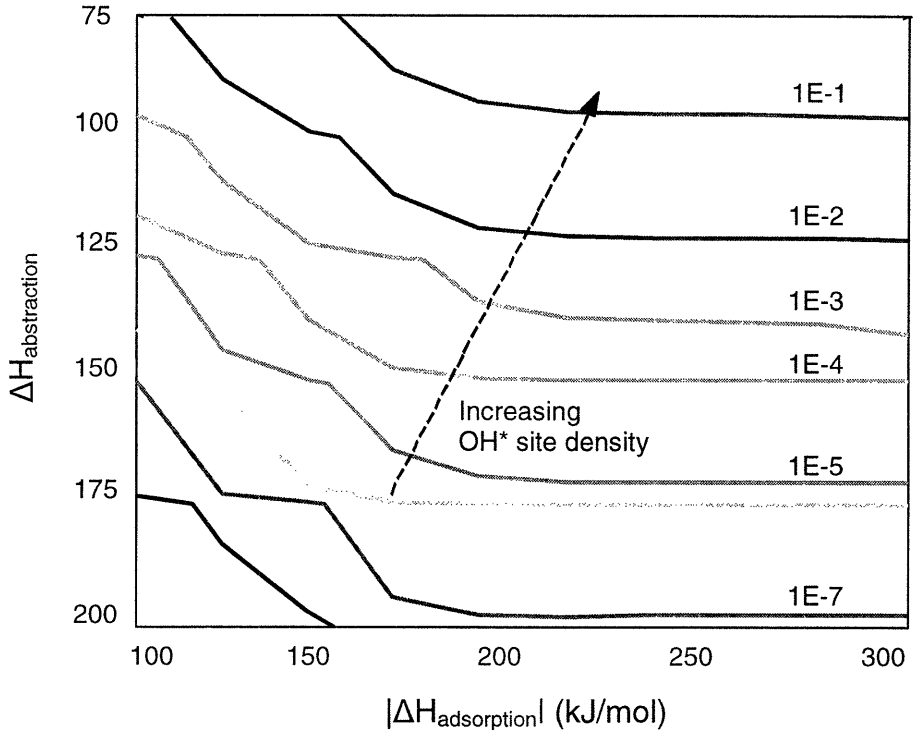

Figure 2.5. Variation in steady-state OH* site fraction at point of peak methyl radical production with changes in catalyst chemistry ($\Delta H_{abstraction}$, $\Delta H_{adsorption}$).

increasing from $\theta_{OH^*} < 10^{-8}$ at $\Delta H_{abstraction}$ = 200 kJ/mole to $\theta_{OH^*} \sim 0.3$ at $\Delta H_{abstraction}$ = 75 kJ/mole. Due to the interconnected nature of surface reaction steps, as $\Delta H_{abstraction}$ is decreased and $|\Delta H_{adsorption}|$ increased, hydroxyl removal becomes increasingly endothermic. The outcome is a dramatic increase in the steady-state equilibrium concentration of OH* species on the surface, which results in the reaction OH* + CH_3 → CH_4 + O* dominating over the desired methyl radical coupling.

While the increasing role of the surface back-reaction OH* + CH_3 → CH_4 + O* reduces the benefit of going to lower values of $\Delta H_{abstraction}$, it still cannot explain the drop off in the computed OCM yield. At a conversion of 20% and $\Delta H_{adsorption}$ = -200 kJ/mole, decreasing $\Delta H_{abstraction}$ from 125 kJ/mole to 100 kJ/mole results in an order-of-magnitude increase in methyl radical production. While a larger portion of these methyl radicals are reacted back to CH_4 (92.6% versus 47.5% for $\Delta H_{abstraction}$ = 125 kJ/mole), the steady-state concentration of CH_3 is still ~ 2 times higher. Thus, methyl radical coupling is always enhanced at lower values of $\Delta H_{abstraction}$. The decrease in yield that is observed at

$\Delta H_{abstraction}$ < 125 kJ/mole can only be explained if we examine the concurrent changes occurring in the other surface reactions. As $\Delta H_{abstraction}$ for methane is reduced, an identical barrier reduction occurs in the remaining hydrogen abstraction steps. In particular, the reactions of O* with the C_2 products (C_2H_6 and C_2H_4) are also accelerated by an order of magnitude. But unlike hydrogen abstraction of CH_4, once these C_2 species undergo hydrogen abstraction to form their radical counterparts, they are quickly reacted away. In the case of C_2H_5, many of these gas-phase consumption reactions simply lead to ethylene formation (i.e., $C_2H_5 \rightarrow C_2H_4 + H$ and $C_2H_5 + O_2 \rightarrow C_2H_4 + HO_2$). However, C_2H_3 formed from C_2H_4 is rapidly consumed by O_2 in the reactions, $C_2H_3 + O_2 \rightarrow HCO + CH_2O$ and $C_2H_3 + O_2 \rightarrow C_2H_3O + O$. At $\Delta H_{abstraction}$ = 125 kJ/mole, these reactions destroy 96% of the C_2H_3 formed; the products ultimately become unwanted CO_x. Importantly, these negative gas-phase consumption channels remain dominant at low $\Delta H_{abstraction}$. While the back-reaction $OH^* + CH_3 \rightarrow CH_4 + O^*$ competes effectively with methyl coupling (which is slow because it is second order in the radical concentration), the comparable back-reaction $C_2H_3 + OH^* \rightarrow C_2H_4 + O^*$ is not as competitive with the very fast $C_2H_3 + O_2$ reaction. For $\Delta H_{abstraction}$ > 100 kJ/mole, < 4% of the C_2H_3 formed is consumed by surface reactions. The increased rate of C_2 destruction continues largely uninhibited by surface back-reactions as $\Delta H_{abstraction}$ is lowered, and eventually outstrips the corresponding increases in C_2 formation with the more active catalyst.

2.3.5 Plug Flow Approximation vs. 2-D Simulation

To quantify the magnitude of potential yield improvements due to irreducible mass-transfer limitations[2,5] on methyl radicals, an identical yield map was created using the plug flow approximation (Figure 2.6). For most values of surface thermochemistry, the plug flow yield closely approximates the multidimensional simulation.

The combination of $\Delta H_{abstraction}$ = 125 kJ/mole and $\Delta H_{adsorption}$ = -250 kJ/mole was selected to further examine the role or lack thereof of CH_3 mass transfer on OCM yield. Figure 2.7 shows the methyl radical profile for the original tube radius of 0.01 cm as well as those for increased radii of 0.05 cm and 0.1 cm at z = 0.2 cm. No significant gradient of methyl radicals was observed for the original radius. A rate-of-production analysis

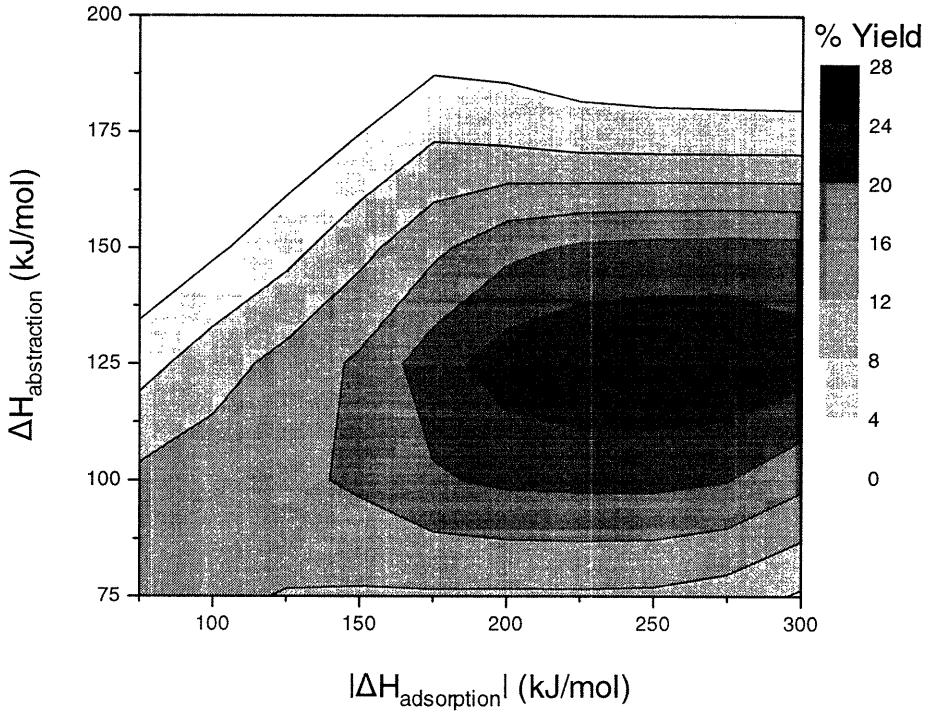

Figure 2.6. OCM yield bound map as determined via plug flow simulation. The various parameter sets employed as well as modeling conditions are identical to those used in generating Figure 2.3. For high surface-to-volume ratios, the plug flow approximation is accurate over most of the range. T = 800°C, P = 1 atm, CH_4:O_2:N_2 feed ratio = 2:1:17. Comparing methyl radical coupling near the wall as opposed to the channel center reveals only minor differences of ~ 4% at z = 0.2 cm.

comparing methyl radical coupling near the wall as opposed to the channel center reveals only minor differences of ~ 4% at z = 0.2 cm. A simple Damkohler reaction-diffusion analysis gives the expected length scale of the methyl radical gradient to be 0.02 cm. At R_0 = 0.01 cm, the walls of the tube remain within the gradient layer, resulting in overlap with the gradient from the opposing wall. It is only when the tube radius is increased that significant CH_3 gradients are seen. When this occurs, the beneficial impacts due to irreversible mass transport limitations can be large. Due to the second order nature of methyl radical coupling, the higher concentration of methyl radicals near the catalyst surface results in an increased rate of methyl radical coupling and overall C_2 yield. When comparing the maximum yields for various diameters, however, we have found the yield predicted by the multidimensional model to be lower for the larger diameter cases. Thus, while irreducible mass transport effects can significantly increase yields under certain conditions, this benefit is diminished by the fact that such effects are largest at sub-

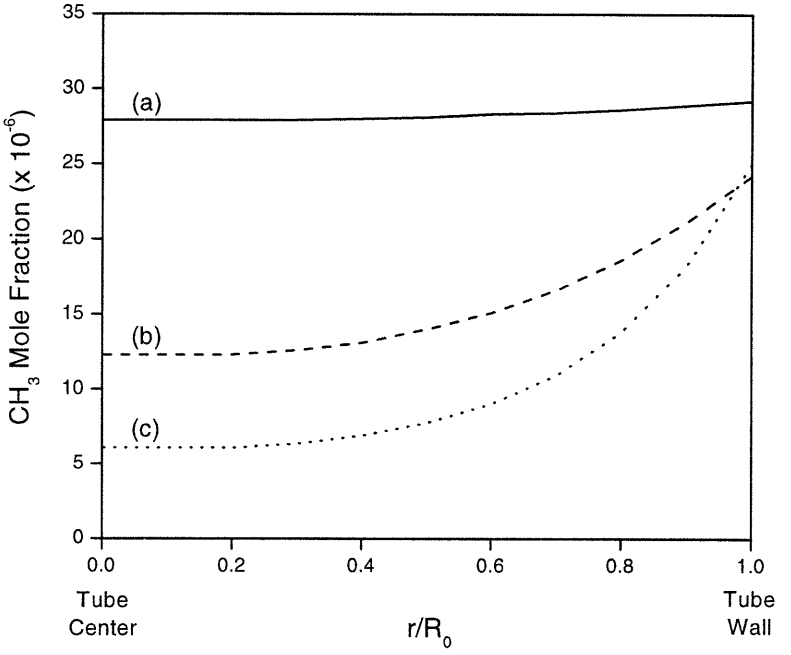

Figure 2.7. Methyl radical mole fraction versus fractional radial distance at z = 0.2 cm for R_0 = (a) 0.01 cm, (b) 0.05 cm and (c) 0.1 cm. For larger radii, the methyl radical concentration is significantly higher near the catalyst surface than in the middle of the channel, and the plug flow approximation is not accurate.

optimal operating conditions. To maximize yields, very high surface-to-volume ratios are required, so the spatial dimensions become small enough that diffusion across the channels becomes competitive with radical reactions. Under this condition, the irreducible mass transfer limitation vanishes and plug flow approximations are fairly accurate.

2.3.6 Importance of Surface Radical Quenching

As an alternative to coupling, methyl radicals near the surface can also react with the catalyst to form surface methoxy species via reaction (12). Poor OCM performance has been previously blamed on large sticking coefficients for methyl radical quenching.[29,30] As mentioned earlier, experimental work by Lunsford[19] seems to indicate that the sticking coefficient for methyl radicals on good OCM catalysts is significantly less than unity. Moreover, Tong and Lunsford inferred a lower limit on the methyl radical sticking coefficient of 10^{-8}.[17] (One caveat is that these sticking coefficients were

determined under conditions different from actual OCM conditions. Also, the physical origin of the low methyl radical uptake rate is not known; in our simulations we have just reduced the A-factor.) Figure 2.8 highlights the impact of the methyl radical sticking coefficient on catalyst yield for $\Delta H_{abstraction}$ = 125 kJ/mole and $\Delta H_{adsorption}$ = -250 kJ/mole. The extent to which this negative reaction channel competes with gas-phase methyl radical coupling plays a significant role in determining attainable C_2 yields. While it is difficult to imagine a sticking coefficient of 10^{-8} relative to other surface reactions (unless there is a barrier or the surface species is only weakly bound), we do see significant improvements in selectivity at the more moderate values for the methyl radical sticking coefficient. A value of 10^{-5} was used as the sticking coefficient in generating Figures 2.1 and 2.3; Figure 2.8 suggests that as long as the sticking coefficient is below 10^{-3}, the yield predictions will be similar.

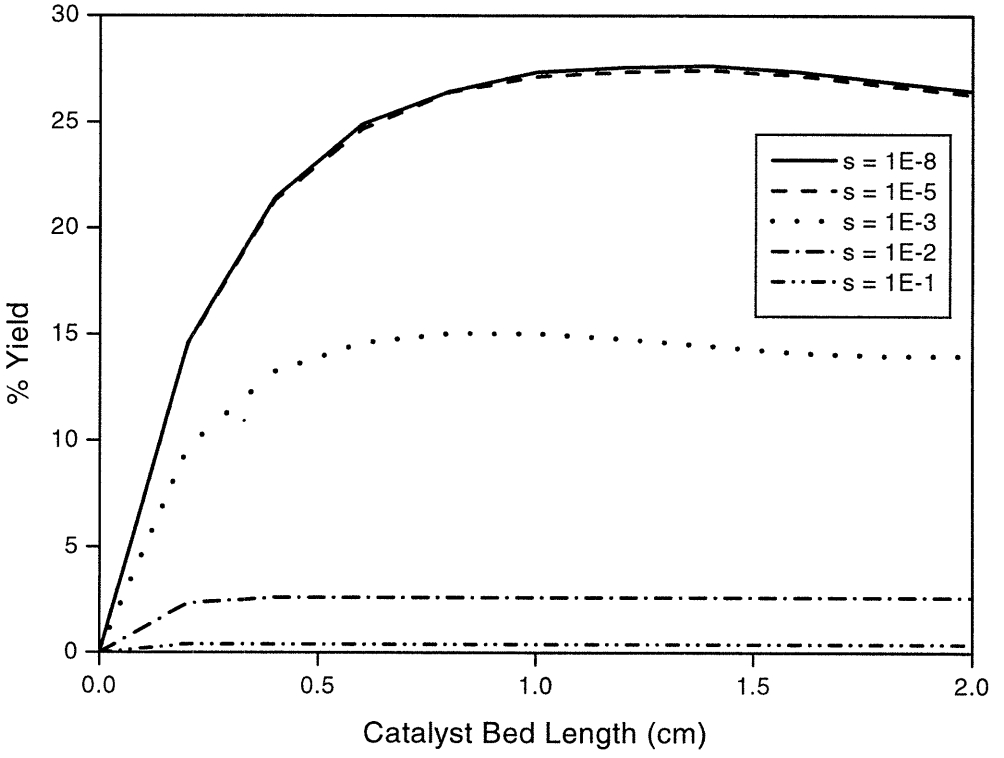

Figure 2.8. Influence of CH_3 quenching reaction sticking coefficient on OCM C_2 yield bound. Modeling conditions: $\Delta H_{abstraction}$ = 125 kJ/mol, $|\Delta H_{adsorption}|$ = 250 kJ/mol, T = 800°C, P = 1 atm, CH_4:O_2:N_2 feed ratio = 2:1:17. Low CH_3 sticking coefficients similar to those measured experimentally[17] appear to be necessary for effective OCM catalysts.

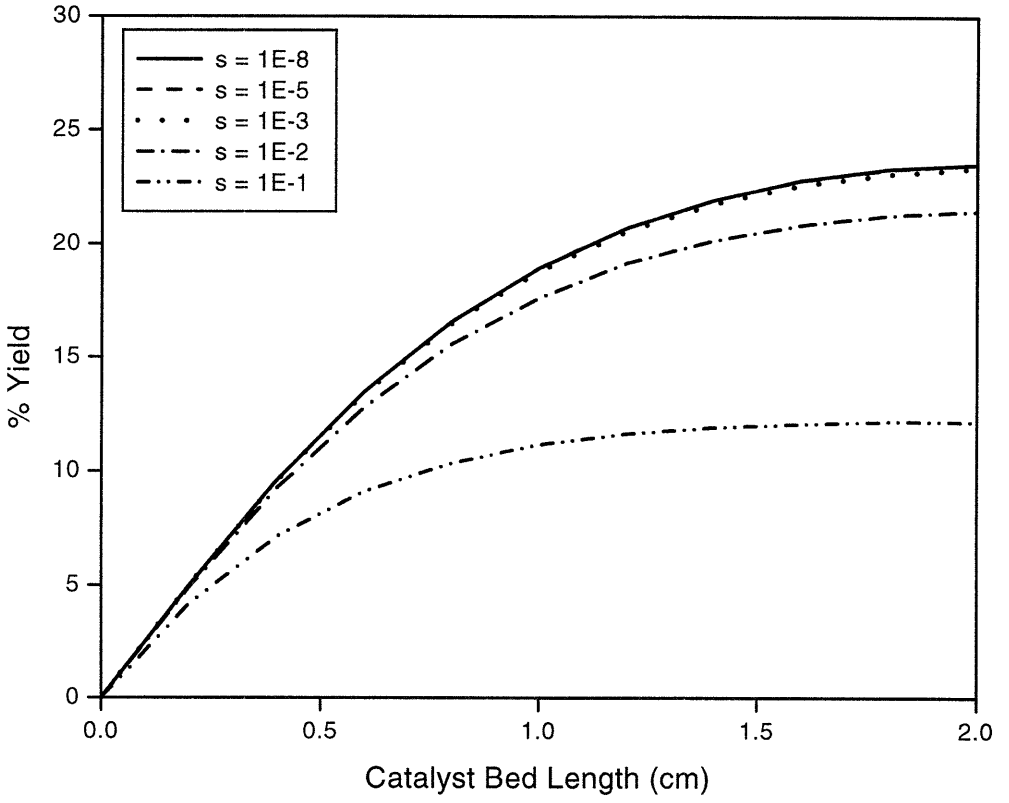

Figure 2.9. Influence of CH_3 quenching reaction sticking coefficient on OCM C_2 yield bound at alternative surface conditions: $\Delta H_{abstraction}$ = 100 kJ/mol, $|\Delta H_{adsorption}|$ = 75 kJ/mol, T = 800°C, P = 1 atm, CH_4:O_2:N_2 feed ratio = 2:1:17. Under these conditions, the yield bound is less sensitive to the sticking coefficient value than under the conditions of Figure 2.8.

The sensitivity to reaction (12) depends on the surface thermochemistry. For example, Figure 2.9 shows the impact of changing the sticking coefficient for a catalyst with $\Delta H_{abstraction}$ = 100 kJ/mole and $\Delta H_{adsorption}$ = -75 kJ/mole. Unlike results at $\Delta H_{abstraction}$ = 125 kJ/mole and $\Delta H_{adsorption}$ = -250 kJ/mole in Figure 2.8, these conditions seem more tolerant of higher sticking coefficients. The robustness of a particular set of surface energies with regard to reaction (12) provides us with an additional criterion to further narrow the desirable surface energetics for OCM catalysts. While both surface compositions achieve yields in excess of 20%, the conditions of $\Delta H_{abstraction}$ = 100 kJ/mole and $\Delta H_{adsorption}$ = -75 kJ/mole may be more desirable as they are less subject to the additional requirement of a low methyl radical sticking coefficient.

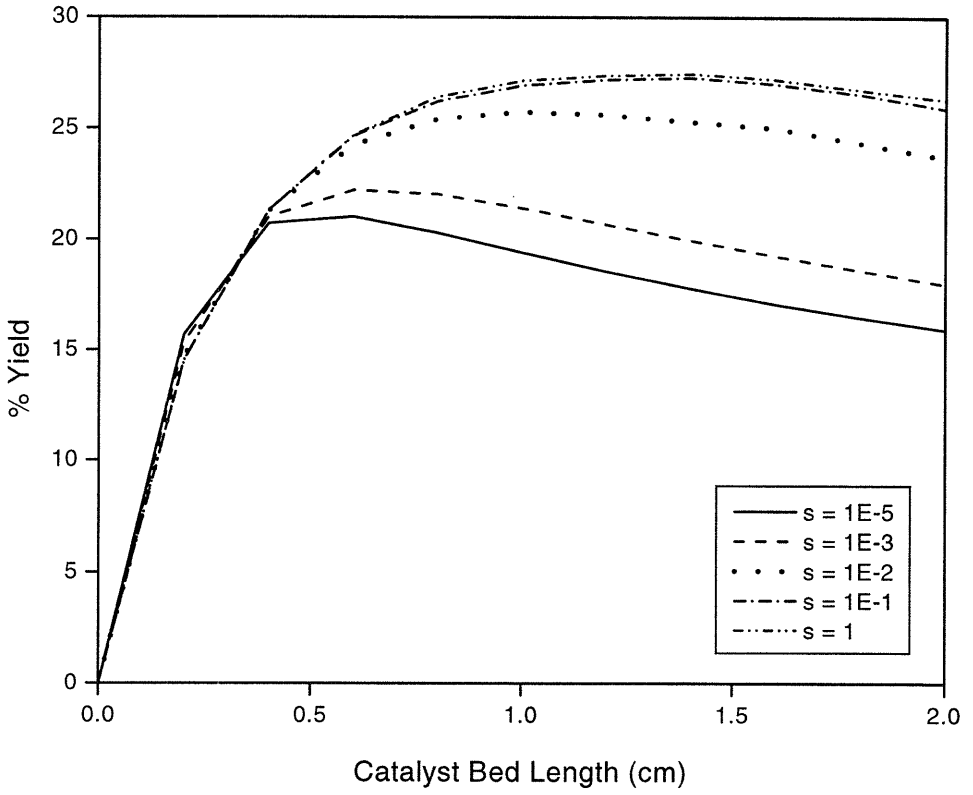

Figure 2.10. Impact of HO_2 sticking coefficient on OCM C_2 yield bound. Modeling conditions: $\Delta H_{abstraction}$ = 125 kJ/mol, $|\Delta H_{adsorption}|$ = 250 kJ/mol, T = 800°C, P = 1 atm, CH_4:O_2:N_2 feed ratio = 2:1:17. Surface destruction of HO_2 is necessary to obtain high yields.

Although surface reaction of methyl radicals is clearly undesirable, radical quenching was found to be advantageous under some circumstances. Studies manipulating the rate of HO_2 quenching by the catalyst (reactions (8) and (9)) via their sticking coefficients show that the catalyst plays an active role in controlling detrimental HO_2 radical populations. As shown in Figure 2.10, while reducing HO_2 quenching increases conversion, the selectivity drops dramatically, leading to an overall decrease in yield. As shown by Mims *et al.*,[6] HO_2 facilitates deep oxidation in the gas phase, primarily through the reaction $HO_2 + CH_3 \rightarrow CH_3O + OH$. Reaction sensitivity and rate-of-production values were extracted with AURORA™ for surface conditions of $\Delta H_{abstraction}$ = 125 kJ/mole and $\Delta H_{adsorption}$ = -250 kJ/mole, using gas and surface mole fraction inputs obtained from earlier 2-D simulations at z = 0.2 cm. When the sticking coefficient is set to 1, > 99% of HO_2 in the system is removed through surface quenching.

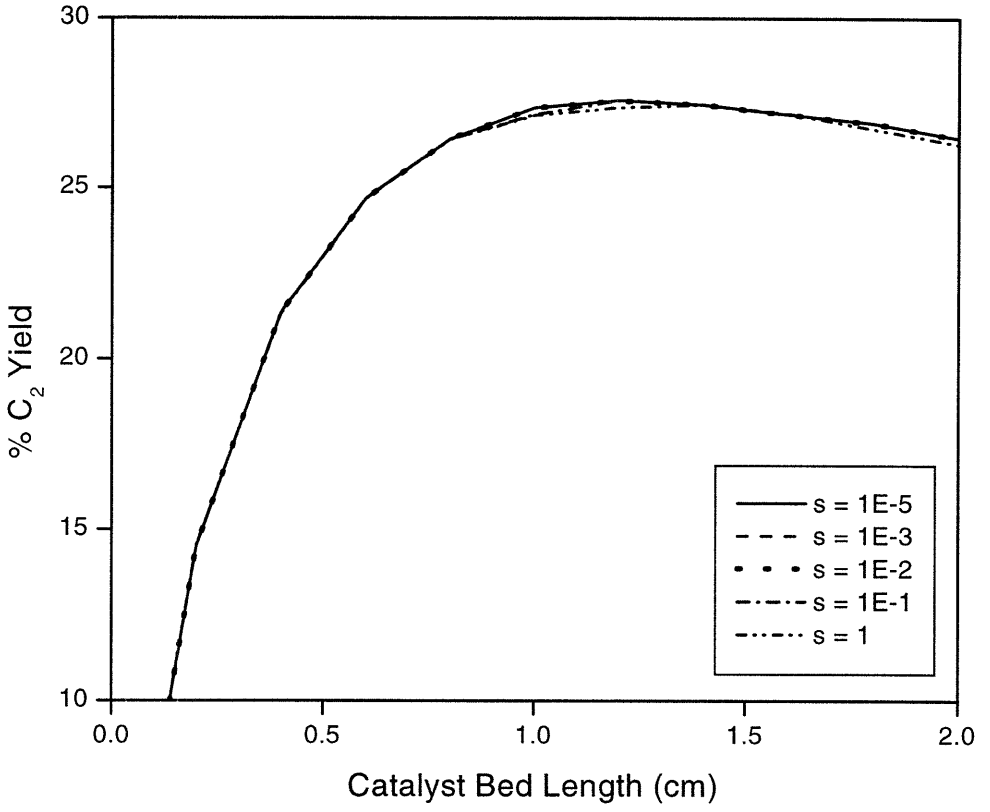

Figure 2.11. Impact of CH_3OO sticking coefficient on OCM C_2 yield bound. Modeling conditions: $\Delta H_{abstraction}$ = 125 kJ/mol, $|\Delta H_{adsorption}|$ = 250 kJ/mol, T = 800°C, P = 1 atm, CH_4:O_2:N_2 feed ratio = 2:1:17. C_2 yields are not sensitive to changes in CH_3OO sticking coefficient.

In contrast, with an HO_2 sticking coefficient of 10^{-5}, an insignificant portion of HO_2 is consumed at the surface. The difference in HO_2 surface quenching reduces the predicted upper bound on C_2 yield from 27% to 21%.

Upon seeing the significant impact of HO_2 on C_2 yield trajectories, the effects of CH_3OO quenching were also investigated. The major reaction channel in the gas phase for CH_3OO loss is $CH_3OO + CH_3 \rightarrow 2CH_3O$. Thus, it was suspected that the effective surface quenching of CH_3OO might also be necessary for high yields. As shown in Figure 2.11, however, the computed C_2 yields are not sensitive to the CH_3OO sticking coefficient. At a sticking coefficient of unity, ~ 72% of CH_3OO destruction is due to surface reaction. HO_2 reacts more readily with the surface through an additional fast channel because of its weak O-H bond. Fortunately, because the concentration of

CH_3OO is an order of magnitude less than that of HO_2, it has a negligible effect on the yield.

2.4 Summary

In this chapter, we describe a simple approach for defining the inherent limits that may exist for a catalytic reaction. This approach allows for the coupling of our physical intuition about the catalyst's function with our knowledge of the elementary surface kinetics. Although the use of elementary steps to describe surface kinetics leads to a large number of reaction parameters, it allows us to operate within a thermodynamically consistent framework, which is critical. We have shown that scaling arguments can be used to reduce the dimensionality of the problem. For the remaining unknowns, we can turn to experimental data to establish a range of possible values for them. Thus, a methodical survey of the attainable yield becomes tractable.

Unlike previous modeling attempts to determine optimal catalytic performance, this methodology focuses on the catalyst's impact on the attainable yield. Oftentimes, in employing a surface mechanism fit using experimental data from a single catalyst, the unique behavior of that catalyst is downplayed. Optimization is conducted solely with respect to reactor parameters such as space-time, feed ratio, and temperature. Lost in this process is the key role of the catalyst surface kinetics on yields. Our results for OCM reaffirm the importance and uniqueness of catalyst behaviors in determining reaction yields. This is demonstrated by the limited range of abstraction and adsorption enthalpies that correspond with superior catalytic performance.

In selecting OCM as a case study for this approach, our goal was to take into account additional complexities and perhaps more rigorously confirm Labinger's conclusion[3] that OCM could not be economically feasible. OCM highlights some of the challenges encountered in attempting to obtain a high-yield catalyst, while providing a relatively simple and well-understood surface mechanism. Here an upper bound of 28% for C_2 yield is determined for a continuous, CH_4/O_2 co-fed, single-pass process under conventional conditions used for catalyst screening. As Labinger pointed out,[3,4] the attainable yield computed under these laboratory conditions of dilute feedstream and

atmospheric pressure is higher than that achievable at more realistic industrial conditions. Based on these studies, it seems that existing catalysts are already close to the performance limit, and it does not appear that OCM can be viable with current economics using a simple packed-bed of catalyst that reacts via the conventional Eley-Rideal mechanism.

It remains to be seen how well real catalysts can be tailored to approach optimal surface thermochemistries. While it is difficult for the performance of idealized catalysts to be matched, this method does provide a guide to future catalyst development. We have found that a particular surface thermochemical behavior (i.e., ΔH_{ads} = -250.00 kJ/mol and ΔH_{abs} = 125.00 kJ/mol) is a necessary requirement for high OCM yield. Moreover, we have identified those specific combinations of enthalpies that result in optimal OCM behavior. With the growing interest in high-throughput catalyst screening, efficient metrics for identifying potentially superior catalysts are critical. In the case of OCM, for each new catalyst synthesized, adsorption and abstraction enthalpies may be measured to see whether they lie in the range where high yield may potentially exist. Thus, this simple metric for catalyst screening established for OCM should be very helpful for future studies.

2.5 References

[1] Colussi, A. J., and Amorebieta, V. T., *J. Catal.* **169,** 301 (1997).

[2] Couwenberg, P. M., Chen, Q., and Marin, G. B., *Ind. Eng. Chem. Res.* **35,** 3999 (1996).

[3] Labinger, J. A., *Catal Lett.* **1**, 371 (1988).

[4] Labinger, J. A., Ott, K. C., *J. Phys. Chem.* **91**, 2682 (1987).

[5] Couwenberg, P. M., Chen, Q., and Marin, G. B., *Ind. Eng. Chem. Res.* **35**, 3999 (1996).

[6] Mims, C. A., Mauti, R., Dean, A. M., and Rose, K. D., *J. Phys. Chem.* **98**, 13357 (1994).

[7] Wolf, D., Slinko, M., Kurkina, E., and Baerns, C., *Appl. Catal. A* **166**, 47 (1998).

[8] Hargreaves, J. S. J., Hutchings, G. J., and Joyner, R. W., *Nature* **348**, 428 (1990).

[9] Shi, C., Rosynek, M. P., and Lunsford, J. H., *J. Phys. Chem.* **98**, 8371 (1994).

[10] Sinev, M., Vorobieva, G. A., and Korchak, V. N., *Kinet. Katal.* **27**, 1007 (1986).

[11] Yates, D. J. C., Zlotin, N. E., Hatano, M., Hinson, P. G., Vines, K. S., and Lunsford, J. H., *J. Catal.* **124,** 557 (1990).

[12] Mackie, J. C., Smith, J. G., Nelson, P. F., and Tyler, R. J., *Energ. Fuel* **4**, 277 (1990).

[13] Lacombe, S., Geantet, C., and Mirodatos, C., *J. Catal.* **151**, 439 (1995).

[14] Li, C., Domen, K., Maruya, K., and Onishi, R., *J. Catal.* **125**, 445 (1990).

[15] Yang, T.-J., and Lunsford, J. H., *J. Catal.* **103**, 55 (1987).

[16] Somorjai, G. A., "Chemistry in Two Dimensional Surfaces." Cornell University Press, Ithaca, 1981.

[17] Tong, Y., and Lunsford, J. H., *J. Am. Chem. Soc.* **113**, 4741 (1991).

[18] Arnaud, Y. P., *Appl. Surf. Sci.* **62**, 37 (1992).

[19] Lunsford, J. H., *in* "Methane Conversion by Oxidative Processes." (E. E. Wolf, Ed.) Van Nostrand Reinheld, New York, 1994, p. 3.

[20] Gillespie, R. J., Humphreys, D. A., Baird, N. C., and Robinson, E. A., "Chemistry." (2nd Ed.) Allyn and Bacon, Inc., Massachusetts, 1989.

[21] Kee, R. J., Rupley, F. M., Miller, J. A., Coltrin, M. E., Grcar, J. F., Meeks, E., Moffat, H. K., Lutz, A. E., Dixon-Lewis, G., Smooke, M. D., Warnatz, J., Evans, G. H., Larson, R. S., Mitchell, R. E., Petzold, L. R., Reynolds, W. C., Caracotsios, M., Stewart, W. E., Glarborg, P., Wang, C., and Adigun, O., CHEMKIN Collection, Release 3.6, Reaction Design, Inc., San Diego, 2000.

[22] Coltrin, M. E., Kee, R. J., and Millar, J. A., *J. Electrochem. Soc.* **131**, 425 (1984).

[23] Coltrin, M. E., Kee, R. J., and Millar, J. A., *J. Electrochem. Soc.* **133**, 1206 (1986).

[24] Abbasi, M. H., Evans, J. W., and Abramson, I. S., *AIChE J.* **29**, 617 (1983).

[25] Reyes, S. S., and Iglesia, E., *J. Catal.* **129**, 457 (1991).

[26] Andrianova, Z. S., Ivanova, A. N., Matkovskii, P. E., and Startseva, G. P., *Kinet. Katal.* **37**, 246 (1996).

[27] Campbell, C. T., *J. Catal.* **204**, 520 (2001).

[28] Dumesic, J. A., *J. Catal.* **185**, 496 (1999).

[29] Campbell, K., Zhang, H., and Lunsford, J. H., *J. Phys. Chem.* **92,** 750 (1988).

[30] Korf, S., Roos, J., Derksen, W., Vreeman, J., Ommen, J. V., and Ross, J., *Appl. Catal. A* **59,** 291 (1990).

Appendix 2-A Calculation of Surface Reaction Enthalpies

The reactions involved in the main catalytic cycle of OCM are:

(1) $O_2 + 2V^* \leftrightarrow 2O^*$ ΔH_{ads}

(2) $CH_4 + O^* \leftrightarrow CH_3 + OH^*$ ΔH_{abs}

(3) $OH^* + OH^* \leftrightarrow H_2O + O^* + V^*$ ΔH_{recomb}

$CH_3 + CH_3 \leftrightarrow C_2H_6$ $\Delta H_{coupling}$

The overall reaction is given by:

$$2CH_4 + \tfrac{1}{2}O_2 \leftrightarrow C_2H_6 + H_2O \qquad \Delta H_{overall}$$

$\Delta H_{overall}$ and $\Delta H_{coupling}$ involve only gas-phase species with well-known heats of formation. Upon independently fixing reactions (1) and (2), the reaction enthalpy for reaction (3) is determined by:

$$\Delta H_{recomb} = \Delta H_{overall} - \tfrac{1}{2}\Delta H_{ads} - 2\Delta H_{abs} - \Delta H_{coupling}$$

We can then employ these values to specify surface species bond strengths, which are used to define enthalpies for the remaining surface reactions.

The formation of O* species on the surface ($\Delta H_{M\text{-}O}$) is defined via reaction (1). This involves the dissociative adsorption of oxygen on the surface, the result of which is the formation of two active O* species.

$$\Delta H_{M\text{-}O} = (\Delta H_{ads} - BDE_{O2})/2$$

where BDE_{O2} is simply the bond dissociation energy of O_2 in the gas phase at the reaction temperature of interest. The energy associated with the transformation of V* to OH* ($\Delta H_{M\text{-}OH}$) can be defined by:

$$\Delta H_{M\text{-}OH} = \Delta H_A + \Delta H_B - \Delta H_{abs} - \Delta H_{recomb}$$

where ΔH_A and ΔH_B are known enthalpies associated with the reactions:

$H + OH \leftrightarrow H_2O$ ΔH_A

$CH_4 \leftrightarrow CH_3 + H$ ΔH_B

Once $\Delta H_{M\text{-}OH}$ was defined, $\Delta H_{M\text{-}OCH3}$ was scaled relative to it. As a first approximation,

$$\Delta H_{M\text{-}OCH3} = \Delta H_{M\text{-}OH} + X_1$$

where X_1 = 41 kJ/mole, the average of the difference in bond energies between R-OH and R-OCH_3 for several hydrocarbon species.

Furthermore, taking into account bonds broken/formed in reaction (2), we can determine the energy associated with the formation of MOH from MO* as:

$$\Delta H_{MO\text{-}H} = -\Delta H_B + \Delta H_{abs}$$

Likewise,

$$\Delta H_{MO\text{-}CH3} = \Delta H_{M\text{-}OCH3} - BDE_{CH3\text{-}O} - \Delta H_{M\text{-}O}$$

where $BDE_{CH3\text{-}O}$ is the bond dissociation energy of methoxy radical.

As labeled in Table 2.1, the reaction enthalpies of reactions (4) – (7) were computed using the previously fixed value of ΔH_{abs}:

$$\Delta H_{4\text{-}7} = \Delta H_{abs} - (BDE_{CH3\text{-}H} - BDE_{R\text{-}H})$$

where R-H represents the major products C_2H_6, C_2H_4, CH_2O, and CH_3OH.

Reaction (8), the first of four peroxy quenching reactions, was calculated via:

$$\Delta H_8 = \Delta H_C + \Delta H_{MO\text{-}H}$$

where ΔH_C is the reaction enthalpy associated with:

$$HO_2 \leftrightarrow O_2 + H \qquad \Delta H_C$$

Reaction (9) is calculated as:

$$\Delta H_9 = \Delta H_D + \Delta H_{M\text{-}O}$$

where ΔH_D is the reaction enthalpy associated with:

$$HO_2 \leftrightarrow OH + O \qquad \Delta H_D$$

Reaction (10) involves the reaction of surface vacancies in quenching gas-phase methyl peroxy radicals. The barrier for this reaction is defined by:

$$\Delta H_{10} = BDE_{CH3O\text{-}O} + \Delta H_{M\text{-}OCH3} + \Delta H_{M\text{-}O}$$

where $BDE_{CH3O\text{-}O}$ is the energy associated with breaking the O-O bond in CH_3OO. Reaction (11) is calculated as:

$$\Delta H_{11} = BDE_{CH3O\text{-}O} + \Delta H_{M\text{-}O}$$

To define the reaction enthalpies associated with the hypothesized methyl radical degradation route on the surface, we have:

$$\Delta H_{12} = \Delta H_{MO\text{-}CH3}$$

This is followed by further hydrogen abstraction from the resulting surface methoxy species. This abstraction can occur by gas-phase radicals, wherein the resulting reaction enthalpy may be described by:

$$\Delta H_{13} = -\Delta H_{M\text{-}OCH3} + \Delta H_E + \Delta H_F$$

where ΔH_E is the enthalpy associated with the reaction:

$$X + H \leftrightarrow XH \qquad \Delta H_E$$

and ΔH_F represents the reaction enthalpy of:

$$OCH_3 \leftrightarrow OCH_2 + H \qquad \Delta H_F$$

Here we assume that the interaction between the surface and the resulting surface formaldehyde species is negligible. Alternatively, hydrogen abstraction from the surface methoxy can occur via neighboring surface oxygen species, at which point the enthalpy of reaction becomes:

$$\Delta H_{14} = -\Delta H_{M\text{-}OCH3} + \Delta H_{MO\text{-}H} + H_F$$

The resulting surface formaldehyde species simply desorb from the surface.

Chapter 3 — Oxidative Dehydrogenation of Ethane

3.1 Introduction

Of the various catalysts screened for the oxidative dehydrogenation of ethane (ODHE), lithium-based catalysts have shown the most promise. For example, LiCl/MgO has long served as a benchmark for superior ODHE performance.[1] Although originally synthesized for OCM, LiCl/MgO's poor thermal stability but excellent C_2H_4/C_2H_6 product ratios prompted its subsequent testing as an ODHE catalyst. In packed-bed studies, LiCl/MgO achieved ethene yields of 58%. Today, LiCl/MgO remains as one of the few catalysts to exceed the homogeneous ODHE threshold[i] set by Burch and Crabb.[2]

Compared to the excellent performance of LiCl/MgO, the 77% ethene yield recently attained by Wang *et al.*'s $LiCl/Nd_2O_3$/sulfated ZrO_2[3,4,5,6] catalyst seems even more remarkable. While the intricacies of its catalytic behavior are not well understood, components of Wang *et al.*'s catalyst have been previously utilized to promote related reactions. Extensive reactor studies have shown that lithium impregnation promotes partial oxidation performance. Specifically, Conway *et al.*[1] have determined that using the chloride precursor of lithium results in superior yields due to LiCl's ability to resist deactivation from carbonate formation. In addition, sulfated ZrO_2 (SZ) has been shown to display activity in a variety of hydrocarbon conversion reactions (e.g., cracking and isomerization). Finally, Korf *et al.*[7] and Conway *et al.*[8] have shown that enhancement of activity without significant loss of selectivity can be achieved through the additional impregnation of small quantities of metal oxide.

3.1.1 Sulfated Zirconia

Among the solid acid catalysts synthesized in Hino *et al.*'s seminal paper,[9] SZ was found to be the strongest superacid (see Figure 3.1). While debate continues[ii] regarding its superacidity,[10,11] SZ has drawn significant attention due to its superior ability to catalyze alkane isomerization and cracking. It is traditionally synthesized via adsorption of sulfate

[i] In fact, at the time of publication, it was the only catalyst in the extensive literature search to display yields above the homogeneous performance threshold.

[ii] Hino *et al.*'s initial classification of SZ's superacidity was based on Hammett indicator results, whereas infrared shifts in CO adsorption experiments indicated that while acidic promotion did occur with sulfate deposition, superacidity was not present.

ions onto amorphous zirconium hydroxide, followed by calcination above 500°C. Numerous articles have been published on the effects of synthesis parameters on the structure and function of SZ. These include studies on the impact of zirconium precursors, pH, sulfation method, aging time and calcination temperature.[12,13,14] While a number of parameters would affect the initial sulfate loading, the final degree of sulfation has been shown to be largely controlled by the final calcination temperature.[15]

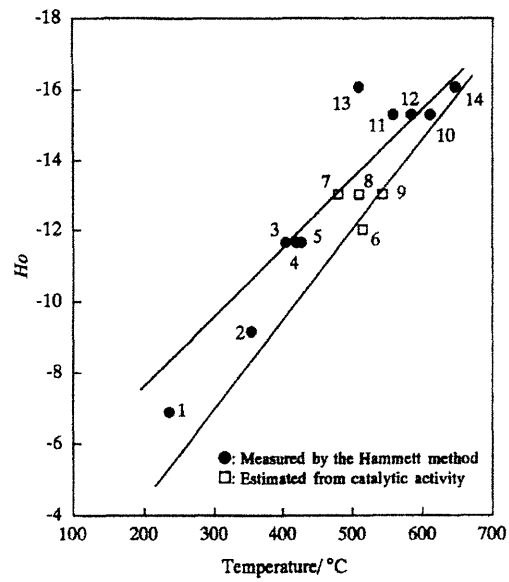

Figure 3.1. Acid strength of various sulfated metal oxides versus other solid acids, as measured by Hammett indicators and catalytic activity.[12] (1) Al_2O_3; (2, 3) ZrO_2-TiO_2; (4) SiO_2-ZrO_2; (5) SiO_2-Al_2O_3; (6) B_2O_3/ZrO_2; (7) MoO_3/ZrO_2; (8) WO_3/TiO_2; (9) sulfated Fe_2O_3; (10) sulfated Al_2O_3; (11) sulfated TiO_2; (12) WO_3/ZrO_2; (13) sulfated SnO_2; (14) sulfated ZrO_2.

3.1.2 Alternative Solid Acid Supports

Concern over the thermal stability of sulfate groups at higher temperatures has prompted research into other solid acid materials. As shown in Figure 3.1, alternative surface moieties such as MoO_x and WO_x also contain electron-deficient cations and have been shown to promote partial oxidation reactions.[16] MoO_x- and WO_x-based materials have the advantage of greater thermal stability under reaction conditions, allowing for the tailoring of surface coverage.[17] Iglesia *et al.*[16,18,19,20] have shown that depending on the support and the impregnated moiety, different coverages resulted in isolated, polydentate and/or bulk formations of MoO_x and WO_x on the surface. As the surface coverage

increases, the ability of the catalyst to delocalize electron deficiencies is enhanced. Thus, catalytic performance can be altered dramatically.

The use of zirconia as a support for anion moieties is not unique. Arata[12] and Corma *et al.*[13] have studied a wide variety of sulfated metal oxides. As seen in Figure 3.1, however, SZ possesses the highest acidity of the sulfated metal oxides. Moreover, as a support, zirconia provides attractive surface area and mechanical properties. Rather than losing these desirable properties, zirconia-based nanocomposites may be synthesized through the introduction of secondary metal cations. The incorporation of small quantities of a secondary metal cation has been shown to improve the thermal stability of the primary oxide and alter the catalytic activity. For instance, the introduction of silica is thought to stabilize zirconia against grain growth and phase transformation.[21,22] Kung *et al.*[23] have also argued that these mixed oxides generate acidity due to charge imbalances in M-O-M* bridges. Nanocomposites can be synthesized via co-precipitation or sol-gel methods. Debate still exists, however, as to the exact form these nanocomposites take — whether they are intimately mixed oxides, one oxide encapsulating the other or one component doped into the primary oxide. Existing literature on the synthesis of zirconia has been focused on the preparation of dense ceramics for structural and electrical applications.

3.1.3 Objectives

The dramatic difference in performance observed between Nd_2O_3/LiCl/SZ and LiCl/MgO (77% vs. 58% ethene yield, respectively) begs the question of how interaction with SZ enhances LiCl's performance. A closely related issue is whether we can capitalize on this interaction to further improve upon the yields attained by Wang *et al.*'s catalyst. Both questions are addressed in this chapter. Through a combination of characterization techniques, the nature and role of the LiCl-SZ interaction have been elucidated. Furthermore, this interaction has been manipulated to realize the potential of using alternative solid acid supports and zirconia nanocomposites to enhance ODHE performance.

3.2 Experimental

3.2.1 Sample Preparation

Metal oxide supports were either commercially purchased (Al_2O_3, Aldrich, > 99%) or synthesized via base precipitation. The latter were prepared by precipitating a 0.2 M aqueous solution[iii] of the metal nitrate or chloride (Alfa Aesar, > 99%) using a 50:50 volumetric dilution of concentrated ammonium hydroxide. A direct-strike method was employed, with dropwise addition of the ammonium hydroxide to the salt solution until the desired pH (9–10) was achieved. The resulting precipitate was aged for 12–18 hr prior to centrifuging and washing (twice in deionized H_2O, twice in isopropanol). The precipitate was then allowed to air dry at room temperature before drying overnight in an oven at 120°C. Afterwards, loose agglomerates of the dried precipitate were crushed in a mortar-and-pestle, followed by calcination at 700°C for 3 hr to form the crystalline metal oxide.

Doped zirconia samples were synthesized via two methods. For dopants available in the nitrate form (Sn, In, Ga and Al), preparation was performed by co-precipitation of a 0.2 M precursor solution of $ZrOCl_2$ $8H_2O$ (Alfa Aesar, 99.9%) and the appropriate nitrate (Alfa Aesar, > 99.9%) with aqueous ammonium hydroxide. Constant pH (9 ± 0.1) was maintained throughout synthesis by individually controlling the addition rates of the base and precursor solutions. Following precipitation, mixtures were aged for 12–18 hr, centrifuged and washed (twice in deionized H_2O, twice in isopropanol). For ZrO_2 doped with Ge, Si, Nb and Ta, a sol-gel method was employed. Variations of the synthesis procedure are discussed in Section 3.3.7. $Ge(OC_2H_5)_4$ (Alfa Aesar, 99.995%) or $Si(OC_2H_5)_4$ (Alfa Aesar, 99.999+%) were pre-hydrolyzed in a water/isopropanol mixture for 2 hr prior to the dropwise addition of a $Zr[O(CH_2)_2CH_3]_4$ (Alfa Aesar, 70% w/w in n-propanol)/isopropanol solution. $Nb[OCH(CH_3)_2]_5$ (Alfa Aesar, 10% w/v in 50:50 isopropanol/hexane) or $Ta[OCH(CH_3)_2]_5$ (Alfa Aesar, 10% w/v in 50:50 isopropanol/hexane) were combined with $Zr[O(CH_2)_2CH_3]_4$ and isopropanol prior to their

[iii] One exception to this was the synthesis of MgO, which was performed in an alcoholic medium to decrease the solubility of the resulting precipitate. Tetraethylammonium hydroxide was used as the base in this case.[24]

dropwise addition to a water/isopropanol solution. The resulting material was aged for 12–18 hr, centrifuged and washed twice in isopropanol. Sulfation was accomplished via wet impregnation using a 0.5 M solution of ammonium sulfate. After drying overnight at 120°C, the sulfated materials were calcined at 700°C for 3 hr. This was followed by LiCl impregnation. In catalysts containing a secondary metal oxide and/or NaCl, co-impregnation of the desired lanthanide nitrate precursor and/or NaCl was also done at this time. After impregnation, materials were dried overnight at 120°C, prior to calcination at 700°C for 3 hr to obtain the final catalyst. As a control, Nd_2O_3/LiCl/SZ was prepared via the co-precipitation method detailed above.

LiCl/Nd_2O_3/MoO_x/ZrO_2 and LiCl/Nd_2O_3/WO_x/ZrO_2 catalysts were prepared by constant-pH (10 ± 0.1) precipitation of a 0.2 M solution of $ZrOCl_2$ $8H_2O$ (Alfa Aesar, 99.9%) with aqueous ammonium hydroxide. The resulting precipitate was aged for 12–18 hr, centrifuged, washed (twice in deionized H_2O, twice in isopropanol) and dried. Incipient wet-impregnation of molybdenum oxide or tungsten oxide on the zirconium precipitate was carried out using $(NH_4)_6Mo_7O_{24}$ $4H_2O$ (STREM Chemicals) or $(NH_4)_6H_2W_{12}O_{40}$ xH_2O (STREM Chemicals). Samples were dried overnight at 120°C and calcined to 700°C. This was followed by a second wet impregnation using LiCl and $Nd(NO_3)_3$ $6H_2O$. After wet impregnation, samples were dried overnight at 120°C, prior to calcination at 700°C for 3 hr to obtain the final catalyst.

3.2.2 Sample Characterization

Surface areas of calcined materials were obtained using a five-point Brunauer-Emmett-Teller method on a Micromeritics ASAP 2000. Phase identification was accomplished by X-ray diffraction (XRD) on a Siemens D5000 θ-θ diffractometer (45 kV, 40 mA, Cu Kα). Scherrer's formula was applied using the ZrO_2 (111) and (-111) diffraction peaks to determine the average crystallite size. The XRD grain sizes agreed well with grain sizes observed in transmission electron microscopy (TEM) images (JEOL 2010, 200 kV). The volume fraction of monoclinic-to-tetragonal phase of ZrO_2 was evaluated using the calibration values of Toraya *et al.*[25] An estimate of the degree of agglomeration in each sample was made by taking the difference between geometric surface area (from Scherrer's analysis, assuming spherical crystallites) and measured (BET) surface areas, and dividing

that by the geometric surface area. To determine the LiCl molten salt transition temperature, differential thermal analysis (DTA) was carried out on a Perkin-Elmer DTA-7 with an α-Al_2O_3 reference under a flowing air stream. Samples were initially ramped to 700°C and data were collected during cooling (10°C/min).

Diffuse reflectance infrared Fourier-transform (DRIFT) spectra were collected using a Harrick HVC-DR2 diffuse reflectance cell on a Bio-Rad FTS-60A spectrometer. For pyridine desorption studies, samples were first pretreated in He for 1 hr, followed by a 30-min exposure to a pyridine-saturated He stream at room temperature. The temperature of the sample cell was then elevated to 150°C, 250°C and 350°C, with spectra being taken after a 1-hr soak at each temperature. Each spectrum was a composite of 256 scans taken at a resolution of 4 cm^{-1}. Photoacoustic Fourier-transform infrared (FTIR) spectra were obtained using a MTEC Model 200 photoacoustic cell. Raman spectroscopy was performed on a Kaiser Hololab 5000R Raman Spectrometer equipped with a Coherent CW tunable laser operated at 514.5 nm. Resulting spectra were normalized with the sample laser exposure time (1–10 ms).

X-ray photoelectron spectroscopy (XPS) data were collected with a Kratos AXIS Ultra Imaging X-ray Photoelectron Spectrometer using a Mono (Al) anode. To identify lithium species present on the catalyst surface, the Li 1s peak was analyzed for binding energies of 48–64 eV. Peaks were calibrated using the C 1s peak. Due to the weak lithium signal, 80 sweeps per sample were performed to achieve adequate signal-to-noise. $Li_2O/Li_2CO_3/ZrO_2$, Li_2CO_3/ZrO_2, $LiZrO_3$ and Li_2SO_4/ZrO_2 were also analyzed to assist in peak identification. XPS was also performed to identify the surface composition of Si-doped ZrO_2 nanocomposites using the Si 2p and Zr 3d peaks. Due to the low Si concentrations, 5–15 sweeps were performed to improve Si signal-to-noise versus 1–5 sweeps for the Zr signal.

Sulfate decomposition kinetics were determined by thermal gravimetric analysis (TGA) using a Perkin-Elmer TGA7. Rate constants for decomposition were evaluated under a He atmosphere at 775°C, 800°C, 825°C and 850°C. To facilitate rapid stabilization of the final hold temperature, samples were first ramped at 15°C/min to 10°C below the desired temperature before reducing the ramp rate to 2°C/min. To minimize the possibility of mass-transfer limitations in the TGA pan, < 20 mg of sample were used for each

experiment and the He flow rate was set to 250 mL/min. Buoyancy effects were subtracted out using data obtained from a second run at identical conditions with the previously run sample. Since significant sulfate decomposition often occurred prior to achieving the final hold temperature, an alternative integral, non-isothermal TGA method for kinetic analysis was also performed.[26,27] In this case, the sample was held at 700°C for 1 hr, followed by a 5°C/min ramp to 850°C.

3.2.3 Reactor Studies

Catalyst testing was done in a vertically mounted, fixed-bed quartz reactor tube (4 mm I.D.) operating at atmospheric pressure. Prior to testing, catalysts were ground, pressed, crushed and sieved into 35–45 mesh particles. Particles were then supported between plugs of packed quartz wool. A quartz-sheathed, K-type thermocouple positioned below the catalyst bed was used in conjunction with an Omega temperature controller and a Lindberg furnace to control the reaction temperature. A second thermocouple inserted from above was used to determine the isothermal zone of the reactor (< 5°C difference from setpoint). High-purity gases (N_2, O_2, C_2H_6 and He, BOC, 99.999%) were metered into the top of the reactor using four independently controlled mass flow controllers (MKS Instruments). N_2 was used as an internal standard to calibrate changes in moles due to reaction. Water vapor was removed via a sodium sulfate trap located in the post-reaction zone. Products were analyzed on-line using an Agilent 6890 Series gas chromatograph equipped with a 10-ft, 1/8"-O.D. molecular sieve 5Å column and a 12-ft, 1/8"-O.D. Porapak Q column. Blank reactor runs indicated that non-catalyzed homogeneous reactions were not significant at any of the experimental conditions examined. Carbon balances were calculated to be within 5% in all runs.

Initial catalyst screening was done with either 0.25 g or 0.30 g of catalyst. The flowrate of reactants was held at 60 mL/min, using a 1:1 molar ratio of C_2H_6:O_2 in a dilute feedstream of 20% reactants. While our conditions were similar to those employed by Wang *et al.*, we used He (instead of N_2) as the diluent to allow inclusion of 5 mL/min N_2 as an internal standard. Catalytic performance was typically measured at 25°C intervals from 550°C to 650°C. Catalysts were not pretreated. Products were analyzed for a minimum of 3 hr at each temperature of interest to quantify potential catalyst deactivation and to allow a

sufficient number of duplicates for statistical analysis. Catalysts typically exhibited < 1% standard deviation for both conversion and selectivity.

Because conversion and selectivity are oftentimes inversely related, it is desirable in many cases to chart the complete selectivity-conversion profile of a catalyst. This was accomplished by manipulating the space velocity at a fixed reactant composition. Trials involved 0.25–1.0 g of catalysts and were performed at 650°C. Volumetric flowrates of 20–200 mL/min were used, corresponding to space velocities of 1,200–48,000 hr^{-1}. Internal and external mass transfer limitations were found to be insignificant under these conditions.

3.3 Results and Discussion

3.3.1 ODHE Performance of LiCl-Impregnated Supports

As mentioned earlier, one of the most puzzling mysteries about LiCl/SZ is its superior performance compared to LiCl impregnated on other supports. Figure 3.2 shows the ODHE results for LiCl impregnated on SZ as well as several other common metal oxide supports. Surprisingly, LiCl/ZrO_2 (and initially LiCl/Al_2O_3) exhibited lower conversions at reduced space velocities. Normally, as space velocity is decreased, the increase in residence time would result in increased conversion. In the case of LiCl/ZrO_2 and LiCl/Al_2O_3, we attributed the abnormal selectivity-conversion behavior to the loss of lithium during reaction. This is a major concern in using any lithium-based catalyst, and similar problems with Li-promoted catalysts have been well documented for OCM.

Figure 3.2 clearly shows that the support plays a critical role in the catalyst's performance in ODHE. With a maximum yield of ~ 65%, LiCl/SZ was far superior to the other LiCl-impregnated catalysts. This might be attributed to SZ's ability to provide for a better dispersion of lithium. Because it is a light atom, however, lithium scatters electrons very poorly, making X-ray mapping nearly impossible. Nevertheless, if lithium was only present on the catalyst surface in the form of chloride for LiCl/SZ, chlorine could be used to map lithium dispersion. To assist in the identification of lithium surface species, XPS measurements were performed on various lithium compounds (oxide, carbonate, sulfate and chloride) supported on precalcined zirconia.[iv] Prior to XPS analysis, each sample was run

[iv] Li_2ZrO_3 was also examined in the event that lithium reacted with the support.

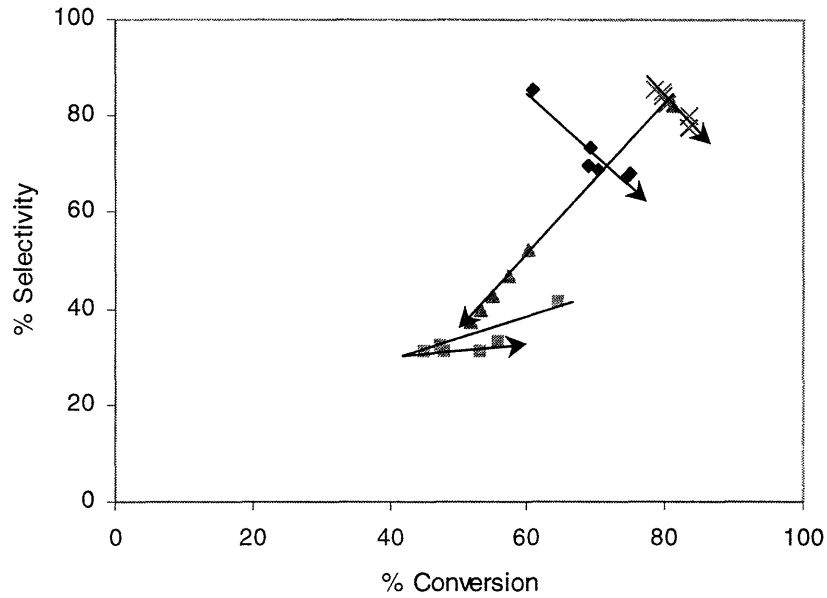

Figure 3.2. Selectivity versus conversion for (×) SZ, (♦) MgO, (▲) ZrO_2 and (■) Al_2O_3 impregnated with LiCl (5 wt% Li). C_2H_6:O_2:N_2/He = 0.1:0.1:0.8, 0.5 g catalyst, P = 1 atm, T = 650°C. Arrows indicate the direction of decreasing space velocity. Declining performance of (▲) LiCl/ZrO_2 and (■) LiCl/Al_2O_3 is attributed to lithium leaching.

under ODHE conditions (10% C_2H_6, C_2H_6/O_2 ratio = 1, flow rate = 60 mL/min, T = 650°C) for 3 hr. As shown in Figure 3.3, LiCl/ZrO_2 exhibited a solitary Li peak at 54.5 eV assigned to LiCl based on the peak locations of the control samples as well as the values for lithium binding energy obtained from NIST.[28]

Having verified that LiCl was the only form of lithium present on the ZrO_2 surface, STEM mapping of chlorine was performed on a LiCl/SZ-based catalyst (specifically, LiCl/Nd_2O_3/Si-doped SZ) and LiCl/MgO, which contained similar quantities of lithium by elemental analysis. Although the influence of overlapping particles must be taken into account, the chlorine map of LiCl/MgO showed noticeable regions where chlorine was absent, which was indicative of lithium agglomeration (see Figure 3.4(a)). In contrast, the LiCl/SZ-based catalyst showed a very uniform dispersion of chlorine on the surface (Figure 3.4(b)).

Several factors were responsible for the improved LiCl dispersion on SZ versus MgO. As a support, SZ possessed a higher surface area than MgO (80 m^2/g versus 38 m^2/g, respectively). The impregnation of SO_4^{2-} on the surface of zirconia resulted in a significant decrease in zirconia grain size with a corresponding increase in surface area. The ultrafine

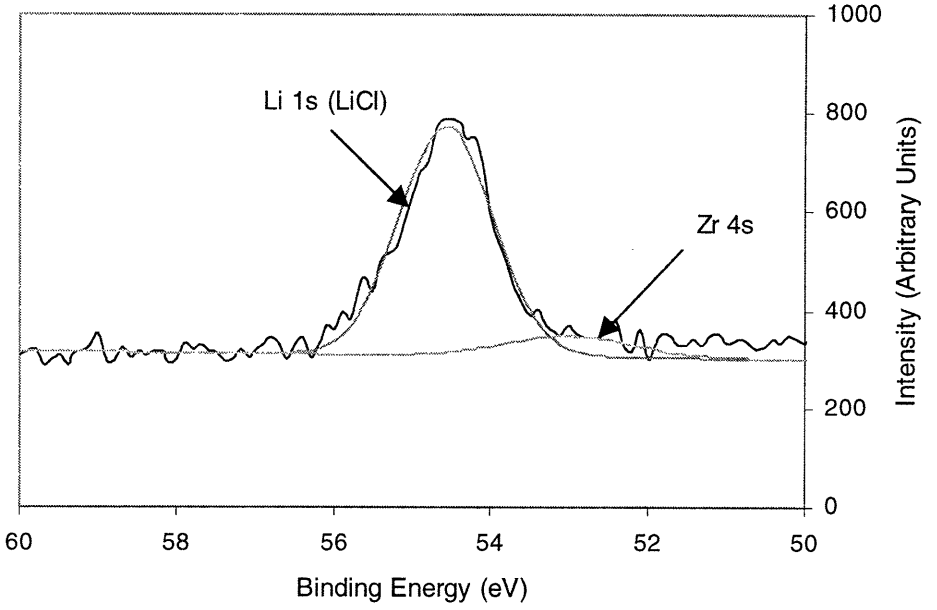

Figure 3.3. XPS spectrum of $LiCl/ZrO_2$, curve fitted with two peaks (in lighter colors) for Li 1s and Zr 4s.

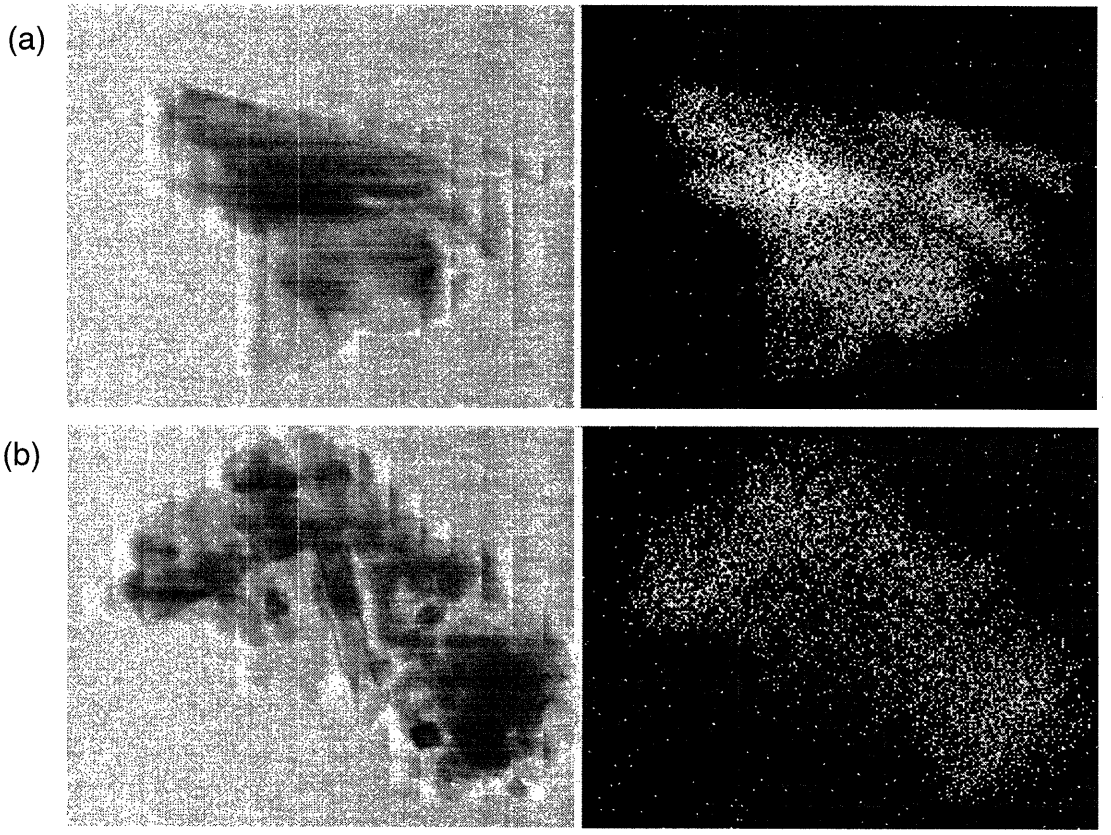

Figure 3.4. TEM images (left) and chlorine X-ray elemental maps (right) of (a) LiCl/MgO and (b) $LiCl/Nd_2O_3$/Si-doped SZ (Si/Zr = 0.05) after reaction under ODHE conditions for 3 hr.

grain size and high surface area undoubtedly allowed for improved LiCl dispersion during wet impregnation. In addition, as a support, one of the most unique features of SZ is its strong acidity. Interactions between LiCl and the acidic sites of SZ could potentially influence catalyst activity, selectivity and stability. To examine whether this was the case, SZ and LiCl/SZ catalysts were exposed to a basic probe molecule, pyridine, and DRIFT spectra were collected (see Figure 3.5). Surface pyridinium species generated by Brönsted acid interactions would give rise to a peak at 1540 cm^{-1}, while pyridine-coordinated Lewis acid sites would result in peaks at 1448 cm^{-1} and 1610 cm^{-1}.[29,30] By collecting spectra at increasing temperatures, the relative populations and strengths of different types of acid sites could be analyzed. Figure 3.5 shows that SZ exhibited strong Lewis acid sites and relatively fewer and weaker Brönsted acid sites. Upon impregnation of LiCl, however, all strong acid sites were quenched on SZ, as illustrated by the disappearance of peaks at 1448 cm^{-1}, 1540 cm^{-1} and 1610 cm^{-1} by 250°C.

Having established the interaction between SZ's acid sites and LiCl, the question remains how such interaction influences LiCl (and hence ODHE performance). One possible metric of catalyst activity is the molten salt transition temperature of LiCl (~ 613°C). This transition is what leads to the generally low surface areas for Li-impregnated

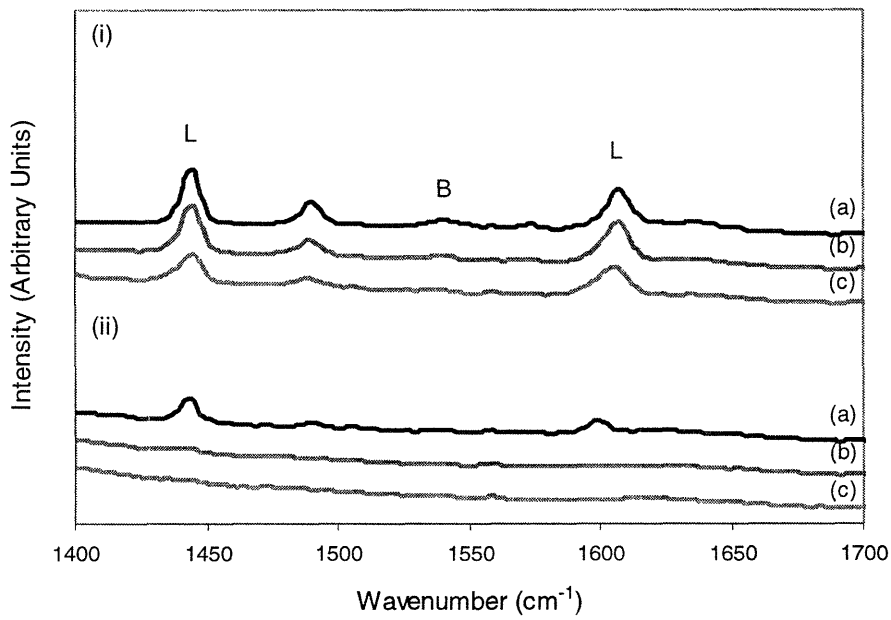

Figure 3.5. DRIFT spectra of (i) SZ and (ii) LiCl/SZ following pyridine adsorption. Spectra were taken at (a) 150°C, (b) 250°C and (c) 350°C. Lewis and Brönsted acid sites are labeled L and B, respectively.

catalysts. While we cannot explain the exact mechanism by which it occurs, it seems intuitive that reducing the LiCl molten salt temperature would result in greater catalytic activity.

Figure 3.6 shows the DTA results for various LiCl-impregnated metal oxide catalysts. The best catalyst, LiCl/SZ, had the lowest molten salt transition temperature (~ 550°C). The worst catalyst, $LiCl/Al_2O_3$, displayed a broad molten salt transition temperature range, with the exothermic peak located at the highest temperature of all samples tested (~ 590°C). We attributed the variety of molten salt temperatures to differences in the degree of interaction between LiCl and the supports.

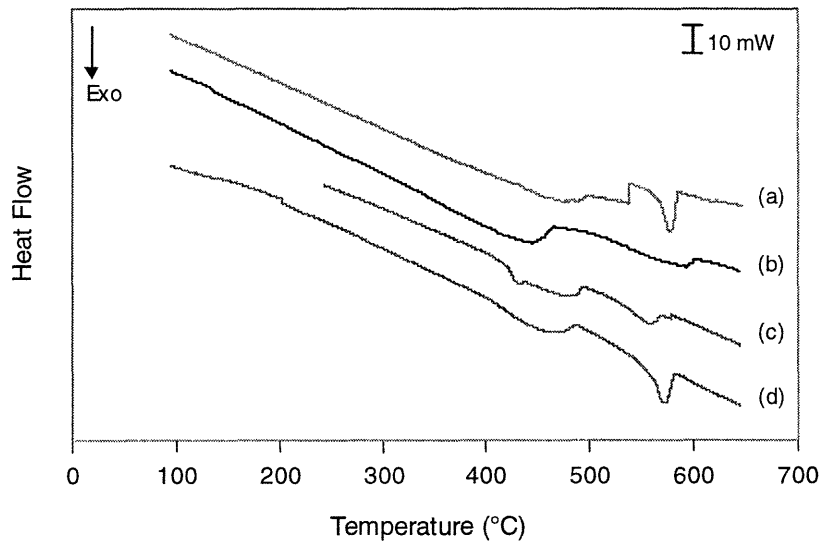

Figure 3.6. DTA of LiCl-impregnated (a) MgO, (b) Al_2O_3, (c) SZ and (d) ZrO_2 with 5 wt% nominal Li loading. Exothermic peaks between 500°C and 600°C indicate the molten salt transition temperature of supported LiCl.

3.3.2 ODHE Performance of WO_x- and MoO_x-based Materials

The strong acid-base interaction between LiCl and SZ and the significant effect of the support material suggested that modifications of the support could alter catalyst performance. Like SZ, WO_x- and MoO_x-based materials also exhibit solid acid behavior and have been successfully employed in related partial oxidation reactions. Wang *et al.*[5] included a $LiCl/WO_x/ZrO_2$ variant of their $LiCl/Nd_2O_3/SZ$ catalyst as part of an ODHE screening study on the impact of different impregnated anion species.[v] In their study, a 6

[v] A MoO_x-based variant of their catalyst, however, was not examined.

wt% nominal surface loading was employed for all anions. Chen *et al.*[16] have shown that the surface density of WO_x and MoO_x has a critical impact on the catalytic performance. They reported dramatic differences in ODHP performance that were attributed to changes in the catalyst's ability to delocalize electronic density. Since control over the WO_x and MoO_x surface density could allow us to tailor our catalyst activity, we have examined the possibility of using WO_x/ZrO_2 and MoO_x/ZrO_2 supports as alternatives to SZ.

WO_x/ZrO_2 and MoO_x/ZrO_2 supports were synthesized with a broad range of surface densities. Since impregnation of WO_x and MoO_x suppressed grain growth and agglomeration of ZrO_2, a calibration curve (not shown) correlating nominal surface loading to the resulting catalyst surface area was established. From this, the exact impregnation quantities needed to obtain the target surface densities could be calculated. Surface areas of our prepared samples are shown in Table 3.1. Since WO_x and MoO_x moieties have a tendency of wetting the surface, their resulting surface densities could be easily estimated.

XRD patterns of WO_x/ZrO_2 and MoO_x/ZrO_2 are shown in Figures 3.7 and 3.8, respectively. As expected, the addition of WO_x or MoO_x suppressed the tetragonal-to-monoclinic phase transformation of zirconia. Furthermore, a similar reduction in the ZrO_2 grain size occurred in both materials from ~ 21 nm to ~ 12 nm with the introduction of WO_x or MoO_x. Thus, supports with larger surface areas were obtained (see Table 3.1). Subsequent impregnation of LiCl and Nd nitrate followed by calcination, however, resulted in catalysts (with 5 wt% Li and 5 wt% Nd_2O_3) of low surface areas. The primary diffraction peaks for WO_3 and MoO_3 coincided with the (110) and (011) diffraction peaks of monoclinic zirconia, making it difficult to determine the exact surface density corresponding to bulk oxide phase formation. The bulk WO_3 phase emerged in WO_x-based materials at surface densities of ~ 5 W/nm^2. Although MoO_x possessed lower thermal stability compared to WO_x, none of the MoO_x-based materials showed evidence of a bulk MoO_3 phase.

To further explore the type of surface coverages exhibited by our samples, Raman spectroscopy was employed. Figure 3.9 reveals that at low WO_x surface densities, no bulk WO_3 and polytungstate structures were present. Raman bands typically associated with the formation of interconnected tungstate moieties (at 830 and 1020 cm^{-1})[31] were absent. Bands below 700 cm^{-1} were generally not considered due to interfering signals from the support.[32]

Table 3.1. BET surface areas and calculated surface densities of WO_x/ZrO_2- and MoO_x/ZrO_2-based catalysts.

Catalyst*	Support Surface Area (m^2/g)	Catalyst Surface Area (m^2/g)	Calculated Surface Density (W/nm^2 or Mo/nm^2)
Wang	95.7	7.9	—
1 W/ZrO_2	55.0	13.4	1.06
3 W/ZrO_2	81.6	14.7	2.95
5 W/ZrO_2	99.0	14.0	4.79
7 W/ZrO_2	105.8	8.8	6.29
10 W/ZrO_2	92.7	12.8	10.25
1 Mo/ZrO_2	60.0	10.3	0.95
3 Mo/ZrO_2	76.9	9.8	3.07
5 Mo/ZrO_2	94.7	12.4	4.87
7 Mo/ZrO_2	109.3	8.0	6.51
10 Mo/ZrO_2	114.7	10.9	9.69

*Catalyst impregnated with 5 wt% Li and 5 wt% Nd_2O_3.

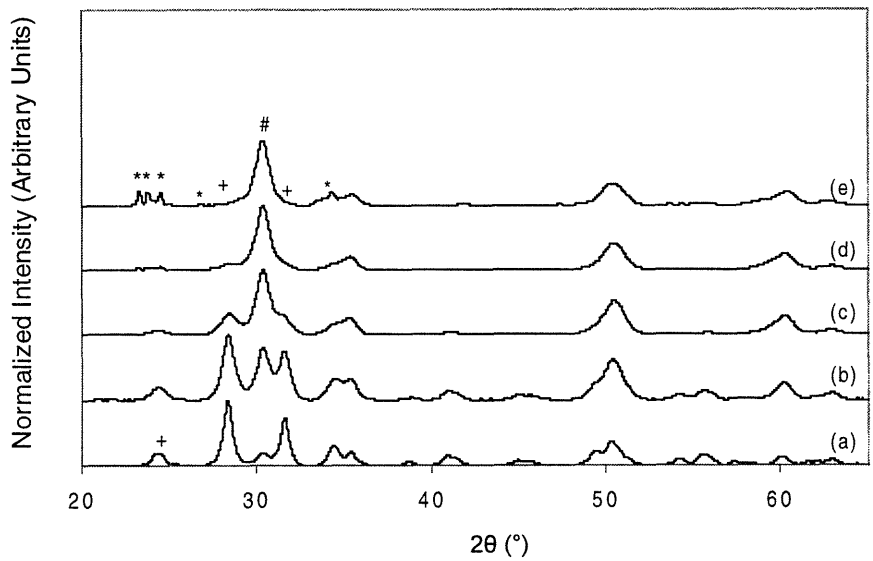

Figure 3.7. XRD patterns of WO_x/ZrO_2 with WO_x surface densities of (a) 1.06, (b) 2.95, (c) 4.79, (d) 6.29 and (e) 10.25 W/nm^2. XRD peaks for tetragonal ZrO_2, monoclinic ZrO_2 and WO_3 are denoted by #, + and *, respectively.

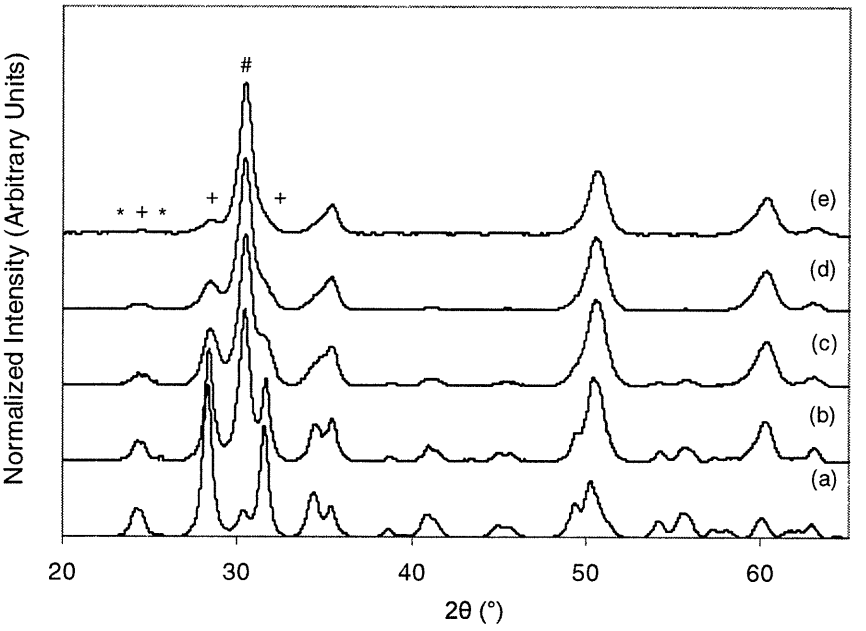

Figure 3.8. XRD patterns of MoO_x/ZrO_2 with MoO_x surface densities of (a) 0.95, (b) 3.07, (c) 4.87, (d) 6.51 and (e) 9.69 Mo/nm^2. XRD peaks for tetragonal ZrO_2, monoclinic ZrO_2 and MoO_3 are denoted by #, + and *, respectively.

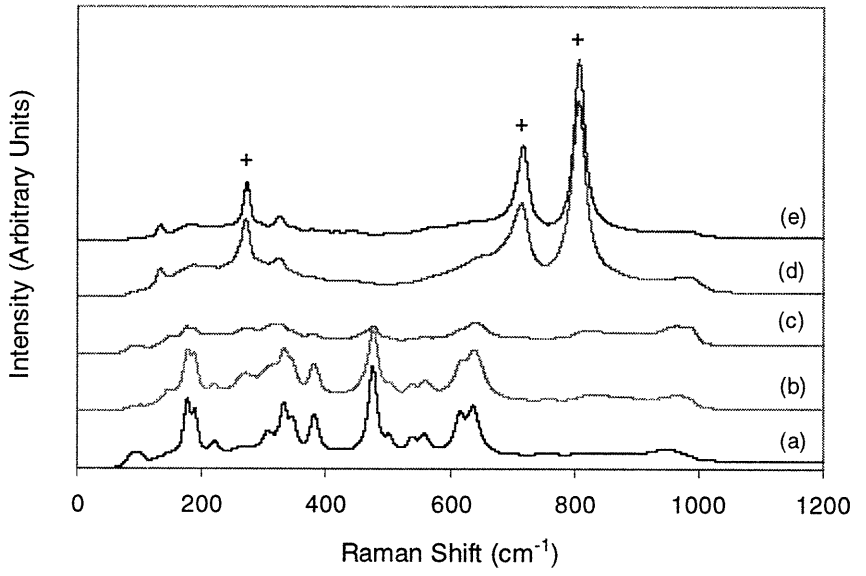

Figure 3.9. Raman spectra of WO_x/ZrO_2 with WO_x surface densities of (a) 1.06, (b) 2.95, (c) 4.79, (d) 6.29 and (e) 10.25 W/nm^2. Raman peaks for bulk WO_3 are denoted by +.

We did, however, observe a peak at 275 cm^{-1}, which has been observed in the Raman spectrum of pure WO_3. This peak was found in samples with surface WO_x densities as low

as 1.06 W/nm^2. Significant WO_3 formation seemed to take place at surface densities > 4.29 W/nm^2, as evidenced by the appearance of peaks at 720 and 808 cm^{-1}, which corresponded to the W-O stretching and W-O bending modes of bulk WO_3, respectively. This was similar to that observed by Barton *et al.*[31] While the lack of sensitivity to polytungstate features is puzzling, it is known that Raman scattering for crystalline WO_3 is much stronger than that for polytungstate species. Thus, even in cases where polytungstate species are abundant, polytungstate peaks can be dwarfed by bands from WO_3.

Unlike WO_x-based materials, MoO_x-based samples showed evidence of polymolybdate cluster formation (see Figure 3.10). At a surface density of 0.95 Mo/nm^2, Raman peaks were observed at 953 cm^{-1} and 875 cm^{-1}, which were assigned to the symmetric Mo=O and asymmetric Mo-O-Mo stretches of polymolybdate moieties, respectively.[18,33] As the MoO_x surface density increased, these bands became less distinct as shoulders to peaks that emerged at 820 cm^{-1} and 1000 cm^{-1}, which were attributed to bulk MoO_3. Unlike the XRD results, Raman spectra suggested that surface densities of > 0.95 Mo/nm^2 gave rise to bulk MoO_3 formation. Despite the anchoring properties of Mo-O-Zr linkages, it appeared that the high calcination temperature of our MoO_x/ZrO_2-based catalysts

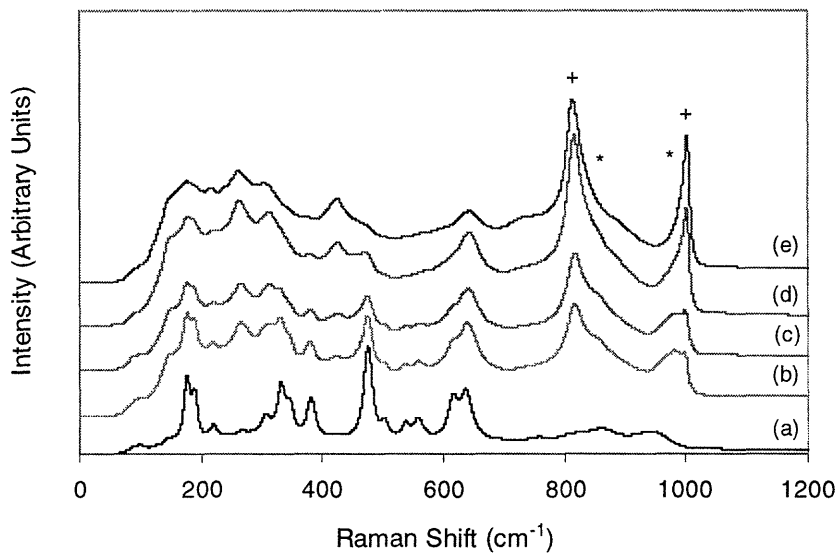

Figure 3.10. Raman spectra of MoO_x/ZrO_2 with MoO_x surface densities of (a) 0.95, (b) 3.07, (c) 4.87, (d) 6.51 and (e) 9.69 Mo/nm^2. Raman peaks for bulk MoO_3 and polydentate MoO_x are denoted by + and *, respectively.

allowed for sufficient surface mobility such that even at low loadings, agglomeration and formation of bulk MoO_3 were possible.

The performance of the various WO_x-based catalysts for ODHE is shown in Figure 3.11. We observed a maximum in ODHE activity at an intermediate WO_x surface density of 2.95 W/nm^2. Barton *et al.*[31] have categorized three distinct types of WO_x formation based on surface density. Using UV-Vis absorption edge energy measurements, they have argued that impregnated WO_x groups were largely isolated at surface densities < 4 W/nm^2.[vi] The range of surface densities of 4–8 W/nm^2 was described by growing networks of polydentate WO_x. Bulk WO_x was formed at surface densities of > 8 W/nm^2. Based on this classification, the increasing delocalizing ability of larger WO_x networks did not result in greater catalyst activity. Instead, the maximum catalytic activity corresponded to isolated WO_x groups, suggesting that exposure of Zr sites was necessary for high activity. The low activity associated with the catalyst containing 10.25 W/nm^2 was therefore attributed to the complete coverage of all Zr sites since theoretical monolayer coverage occurred at ~ 7.8 W/nm^2. Such low activity of bulk WO_3 relative to well-dispersed, polydentate WO_x has also been noted in other reactions such as isomerization.[34]

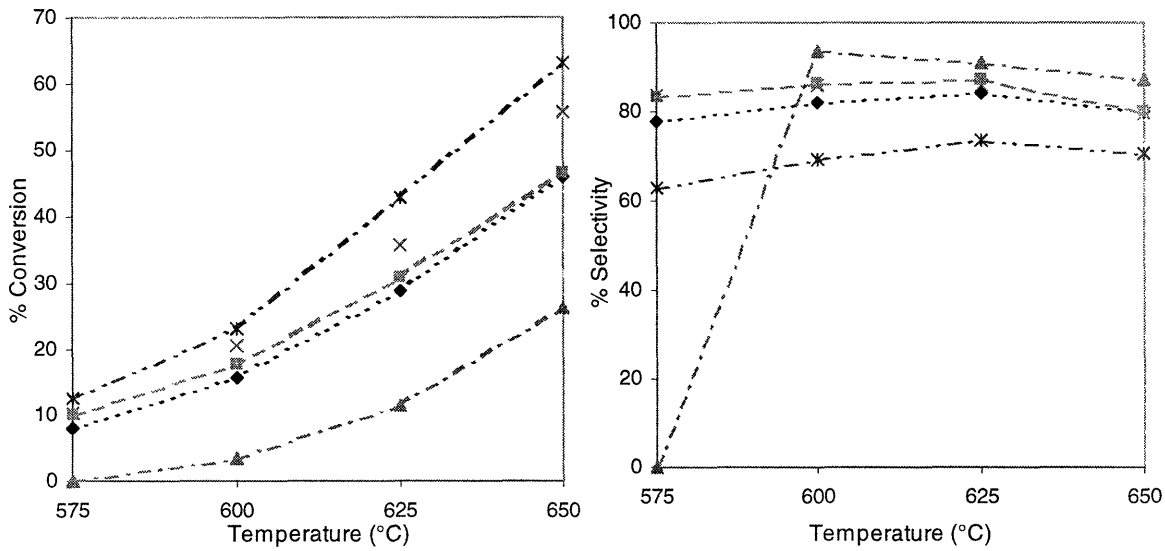

Figure 3.11. Conversion and selectivity for ODHE over $LiCl/Nd_2O_3/WO_x/ZrO_2$ with WO_x surface densities of (×) 1.06, (ж) 2.95, (♦) 4.79, (■) 6.29 and (▲) 10.25 W/nm^2. Catalyst composition: 5 wt% Li, 5 wt% Nd_2O_3. Flowrate = 60 mL/min, C_2H_6:O_2:N_2/He = 0.1:0.1:0.8, 0.3 g catalyst, P = 1 atm.

[vi] The issue of whether polydentate formation can occur at low coverages, however, is still being debated.

On the other hand, the highest selectivity at 600–650°C was achieved by the catalyst with 10.25 W/nm^2. The catalyst with 2.95 W/nm^2 displayed the lowest selectivity, despite showing the highest conversion. This inverse relationship between conversion and selectivity demonstrated over the various WO_x surface densities examined might appear to indicate that subsequent heterogeneous combustion of the desired product was occurring as in the case of OCM and oxidative dehydrogenation of propane (ODHP). However, the stable selectivity versus temperature performance (despite increasing conversion) of each catalyst argued against such interpretation. The consistent trade-off between conversion and selectivity over the WO_x-based catalysts was most likely due to changes in the branching between ODHE and ethane combustion surface reactions, which were affected by the WO_x surface density.

MoO_x-based catalysts behaved similarly to WO_x-based catalysts (see Figure 3.12) as higher surface densities of MoO_x corresponded to lower conversions. As with WO_x-based catalysts, the activity of MoO_x-based catalysts did not correlate to changes in surface area (see Table 3.1). It appeared that the optimum surface density was already achieved by 0.95 Mo/nm^2, compared to 2.95 W/nm^2 for the WO_x-based catalysts. We attributed this to

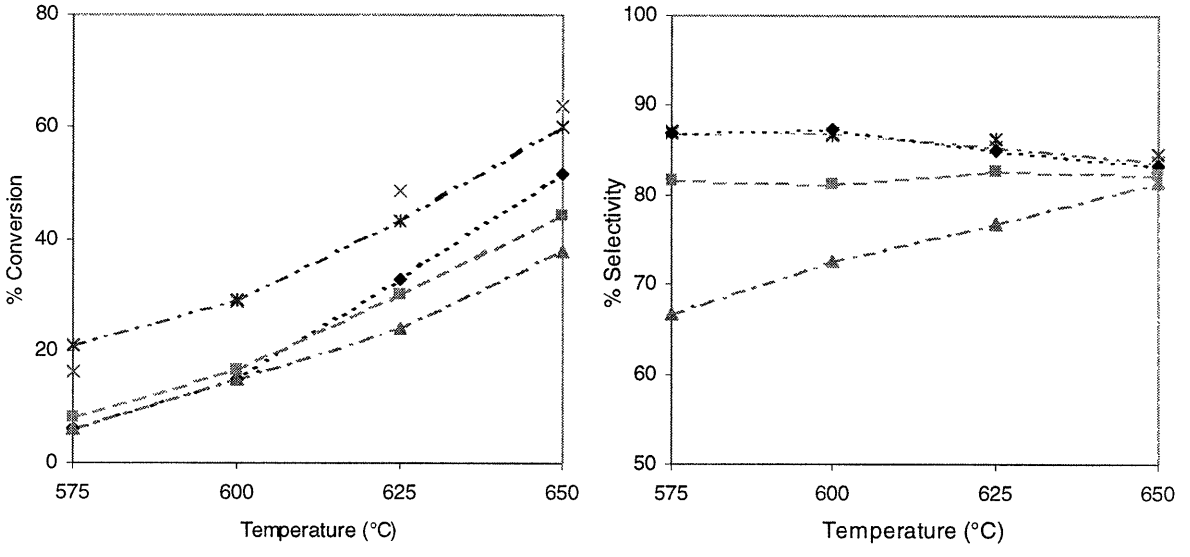

Figure 3.12. Conversion and selectivity for ODHE over $LiCl/Nd_2O_3/MoO_x/ZrO_2$ for MoO_x surface densities of (×) 0.95, (✳) 3.07, (♦) 4.87, (■) 6.51 and (▲) 9.69 Mo/nm^2. Catalyst composition: 5 wt% Li, 5 wt% Nd_2O_3. Flowrate = 60 mL/min, C_2H_6:O_2:N_2/He = 0.1:0.1:0.8, 0.3 g catalyst, P = 1 atm.

the greater mobility of MoO_x surface anions and their greater tendency to agglomerate under ODHE reaction conditions, forming bulk MoO_3 at surface densities of > 0.95 Mo/nm^2 (see Figure 3.10).

In contrast to the WO_x-based catalyst series, MoO_x-based catalyst series did not display an inverse relationship between activity and selectivity. The catalyst with 0.95 Mo/nm^2 exhibited both superior activity and selectivity, whereas the catalyst with 9.69 Mo/nm^2 was the least active and selective. At lower reaction temperatures, the catalysts with high surface coverages, 6.51 Mo/nm^2 and 9.69 Mo/nm^2, exhibited lower ODHE selectivities. As the reaction temperature increased, however, the differences in selectivity between different catalysts diminished. In studies of LiCl/metal oxides, Korf *et al.*[7] attributed the low selectivities at low temperatures to the exposure of bare metal oxide sites. At higher temperatures, they argued that greater lithium mobility resulted in the quenching of these unselective sites. A similar phenomenon might exist in this case with the exposure of unselective bulk MoO_3 active sites at low reaction temperatures. Another possibility was that at higher temperatures, the increased conversion of ethane resulted in the light-off of heterogeneous-assisted, gas-phase reactions, which began to dominate the selectivities of the various MoO_x-based catalysts examined.

To definitively compare catalyst performance, selectivity-conversion trajectories were charted for the best WO_x- and MoO_x-based catalysts according to results in Figures 3.11 and 3.12. This was compared to the performance of Wang *et al.*'s $LiCl/Nd_2O_3/SZ$ catalyst. Trajectories were generated by altering the reactant flowrate through the packed bed while maintaining a constant feed composition. To capture the behavior at higher conversions, larger quantities of catalyst (0.5 g or 0.75 g) were used. As shown in Figure 3.13, each of the three catalysts suffered a significant decrease in selectivity at different points along their selectivity-conversion trajectories, which could be attributed to the onset of Li leaching. At conversions below 75%, the $LiCl/Nd_2O_3/MoO_x/ZrO_2$ catalyst displayed superior stability to the $LiCl/Nd_2O_3/WO_x/ZrO_2$ catalyst and comparable performance as $LiCl/Nd_2O_3/SZ$. At a higher catalyst loading of 0.75 g, however, the $LiCl/Nd_2O_3/MoO_x/ZrO_2$ catalyst deactivated rapidly, resulting in a reversal of the selectivity-conversion trajectory before holding at a conversion of ~ 60%. In contrast, the $LiCl/Nd_2O_3/SZ$ showed a much less severe decline in catalyst performance while reaching

conversions of ~ 80%. Therefore, while WO_x/ZrO_2-based and MoO_x/ZrO_2-based catalysts could be tailored in anion surface density, they suffered from a lower stability compared to SZ-based catalysts.

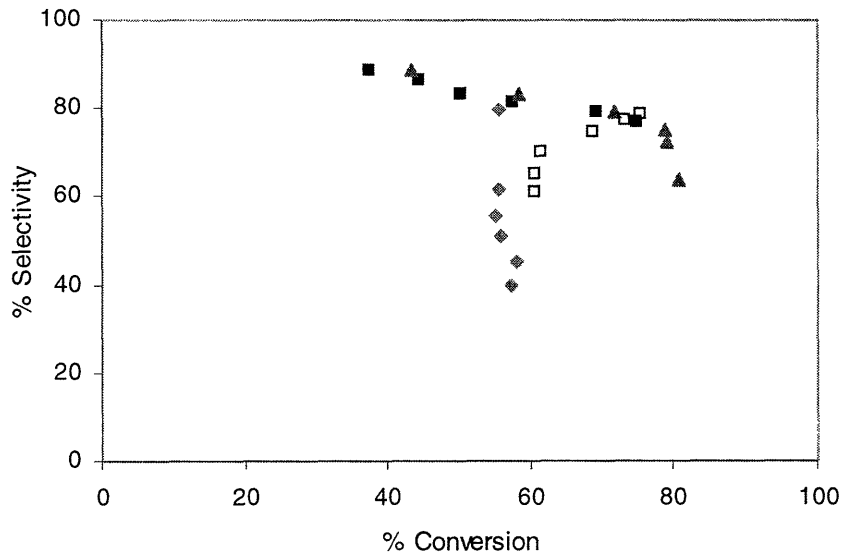

Figure 3.13. Selectivity versus conversion for (♦) $LiCl/Nd_2O_3/WO_x/ZrO_2$ (with 1.06 W/nm^2), (■,□) $LiCl/Nd_2O_3/MoO_x/ZrO_2$ (with 0.95 Mo/nm^2), and (▲) $LiCl/Nd_2O_3/SZ$. Catalyst composition: 5 wt% Li, 5 wt% Nd_2O_3. $C_2H_6:O_2:N_2/He$ = 0.1:0.1:0.8, (♦,■,▲) 0.5 g or (□) 0.75 g catalyst, P = 1 atm, T = 650°C. Declining performance of (♦) $LiCl/Nd_2O_3/WO_x/ZrO_2$ and (□) $LiCl/Nd_2O_3/MoO_x/ZrO_2$ is attributed to lithium leaching.

3.3.3 ODHE Performance of Doped Zirconia-based Nanocomposites

Another approach for enhancing catalytic performance is through manipulation of zirconia itself. Recent work has shown that doping of zirconia dramatically improved the catalytic properties of $Pt/WO_x/ZrO_2$.[35] Thus, we examined the potential impact of introducing various cationic dopants into the zirconia support for ODHE catalysts. In dopant selection, our desire was to explore the effect of various valence states as well as electronegativities. For the purposes of initial screening, the atomic ratio of the secondary cation to Zr^{4+} was fixed at 0.05. Table 3.2 lists the conversions and selectivities of several doped ZrO_2 nanocomposite catalysts in comparison to $LiCl/Nd_2O_3/SZ$. All supports were impregnated with 5 wt% Li and 5 wt% Nd_2O_3. The selectivity of our co-precipitated $LiCl/Nd_2O_3/SZ$ catalyst was similar to that published by Wang *et al.*[6] (84% versus 83%, respectively, at 650°C). We attributed the difference in conversion to the catalyst bed

loading (0.25 g versus 1.0 g) and the reactor configuration. At 600°C, a dramatic enhancement in activity could be seen with the doped materials. At 650°C, several of the nanocomposite materials showed enhanced conversion and selectivity compared to $LiCl/Nd_2O_3/SZ$. The changes in catalytic behavior appeared to correlate well to the valance state of the cationic dopant. Specifically, dopants with a similar valance state as Zr^{4+} (i.e., Sn^{4+}, Si^{4+} and Ge^{4+}) were found to exhibit enhanced activity and selectivity. Catalysts doped with cations of +3 and +5 valance states displayed significantly increased catalytic activity without substantial decrease in selectivity in most cases (except Al^{3+}).

In all cases, the introduction of dopants resulted in sulfated zirconia supports with higher surface areas. However, calcination after LiCl impregnation gave rise to a significant loss in surface areas (see Table 3.2). Some catalysts did show higher surface area than $LiCl/Nd_2O_3/SZ$, which might, in part, account for their improved catalytic activity. Surface area improvements from the incorporation of a secondary component are not uncommon, although they do raise the question of whether the secondary component is truly doped into the zirconia matrix. This issue is addressed in greater detail in Section 3.3.5 for Si-doped ZrO_2-based nanocomposite catalysts.

Table 3.2. Performance of $LiCl/Nd_2O_3$/doped SZ for ODHE.*

Dopant	Surface Area (m^2/g)	600°C		650°C	
		% Conversion	% Selectivity	% Conversion	% Selectivity
—	7.9	2	100	27	84
Ga^{3+}	12.5	22	85	61	84
In^{3+}	5.6	25	83	54	79
Al^{3+}	5.8	43	5	63	23
Sn^{4+}	12.4	19	75	52	91
Si^{4+}	8.2	13	87	42	90
Ge^{4+}	8.6	19	91	41	93
Nb^{5+}	10.3	31	70	61	80
Ta^{5+}	16.0	25	76	60	82

* Catalyst composition: 5 wt% Li, 5 wt% Nd_2O_3, dopant/Zr = 0.05. Flowrate = 60 mL/min, C_2H_6:O_2:N_2/He = 0.1:0.1:0.8, 0.25 g catalyst, P = 1 atm.

Figure 3.14 shows the selectivity-conversion trajectories of selected catalysts. Surprisingly, the $LiCl/Nd_2O_3/SZ$ control exhibited selectivities as low as 65%. In contrast, Wang *et al.*[6] recorded an ethene selectivity of 83% at an ethane conversion of 93%. We attributed this difference in performance to several reasons. Firstly, the absence of silica diluent in our catalyst bed potentially resulted in greater gas-phase contributions and LiCl volatility. Secondly, the larger bed volumes used by Wang *et al.*[3,4,5,6] might mask the catalyst deactivation arising from LiCl leaching. Thirdly, differences could arise from minor variations in the synthesis of $LiCl/Nd_2O_3/SZ$ and the reactor setup. Finally, the lack of an internal standard might have shifted Wang *et al.*'s catalyst conversions to higher values by not taking into account changes in the total number of moles in the gas stream due to reaction. Regardless, unlike $LiCl/Nd_2O_3/SZ$, the excellent selectivities of our $LiCl/Nd_2O_3$/doped SZ nanocomposite catalysts were remarkably stable up to conversions of 60–70%. In particular, the Si-doped ZrO_2-based nanocomposite catalyst displayed the best performance, maintaining 84% selectivity at 90% conversion.

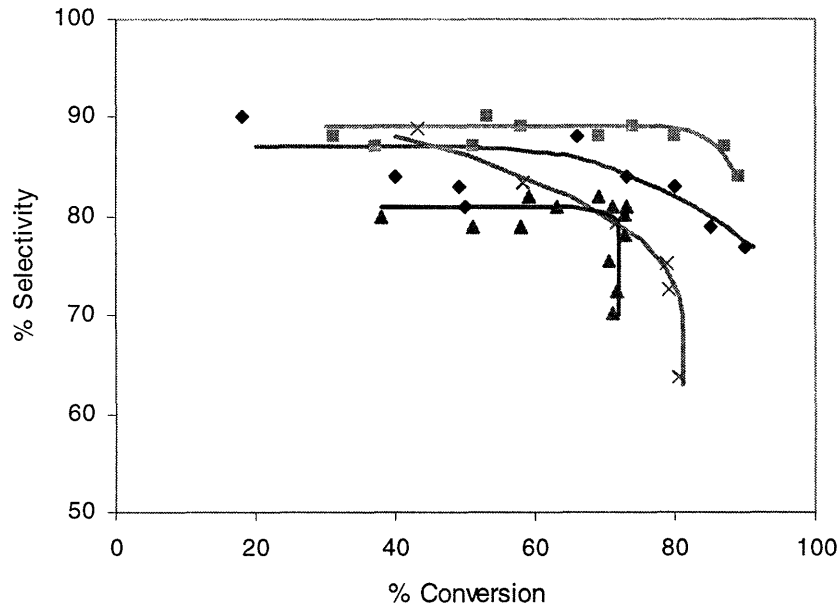

Figure 3.14. Selectivity versus conversion for $LiCl/Nd_2O_3/SZ$ with (×) no dopant, (■) Si dopant, (♦) Ge dopant and (▲) Sn dopant. Lines are drawn to guide the eye. Catalyst composition: 5 wt% Li, 5 wt% Nd_2O_3, M/Zr = 0.05. C_2H_6:O_2:N_2/He = 0.1:0.1:0.8, 0.25 g or 0.5 g catalyst, P = 1 atm, T = 650°C. Decline in trajectories observed may be influenced by lithium leaching effects.

We note that the catalysts exhibited a drop-off in selectivity at some point along their selectivity-conversion trajectory in Figure 3.14. This could be due to several reasons. Firstly, as conversion increased, the probability increased that desorbed radicals could initiate gas-phase reaction channels that were less selective. This was not believed to be the case, however, as each material exhibited a different conversion that corresponded to the drop-off in selectivity. Secondly, the drop-off in selectivity might be related to the competition between ethane and ethene for the active sites, thus linking catalytic performance to the adsorption behavior of these materials. At high conversions, insufficient ethane concentrations might have allowed unselective adsorption of ethene to occur on reaction sites, resulting in ethene combustion and decreased selectivity. Finally, with increased conversion, increasing amounts of H_2O were formed, which could react with surface chlorine to produce HCl that then desorbed from the surface. Conway and Lunsford[1] have shown that the Li concentration would adjust to maintain a stoichiometric ratio of ~ 0.9:1 with Cl. Thus, Cl loss would be quickly followed by Li loss.

3.3.4 ODHE Performance of Nanocomposite Catalysts with Alkali Salt Mixtures

With decreasing space velocity, residence time in the catalyst bed would increase, typically resulting in an increase in conversion. In charting selectivity-conversion trajectories, we occasionally observed an initial period of steady conversion decay, regardless of decreases in space velocity. Examples of such phenomenon were seen earlier in Figure 3.2 with $LiCl/Al_2O_3$ and $LiCl/ZrO_2$ catalysts, and in Figure 3.13 with the WO_x- and MoO_x-based catalysts. This behavior was not observed for our $LiCl/Nd_2O_3$/Si-doped SZ nanocomposite catalysts at reactant flowrates < 100 mL/min, but appeared at higher flowrates that would be employed in industrial operations. Figure 3.15 illustrates the steady decline in conversion with run time, which was attributed to Li volatilization. Concurrent deposition of lithium silicate on the walls of the reactor tube was observed. These effects were not reported by Wang *et al.*[3,4,5,6] and might not have been observed for several reasons. Firstly, the dilution of their reactor bed with 2.0 g of quartz sand might have eliminated hot spots wherein volatilization would more likely occur. Secondly, the increase in catalyst bed size in combination with the large quantity of catalyst used might have better accommodated the moving front of volatilized Li. Also, under the low flowrate employed

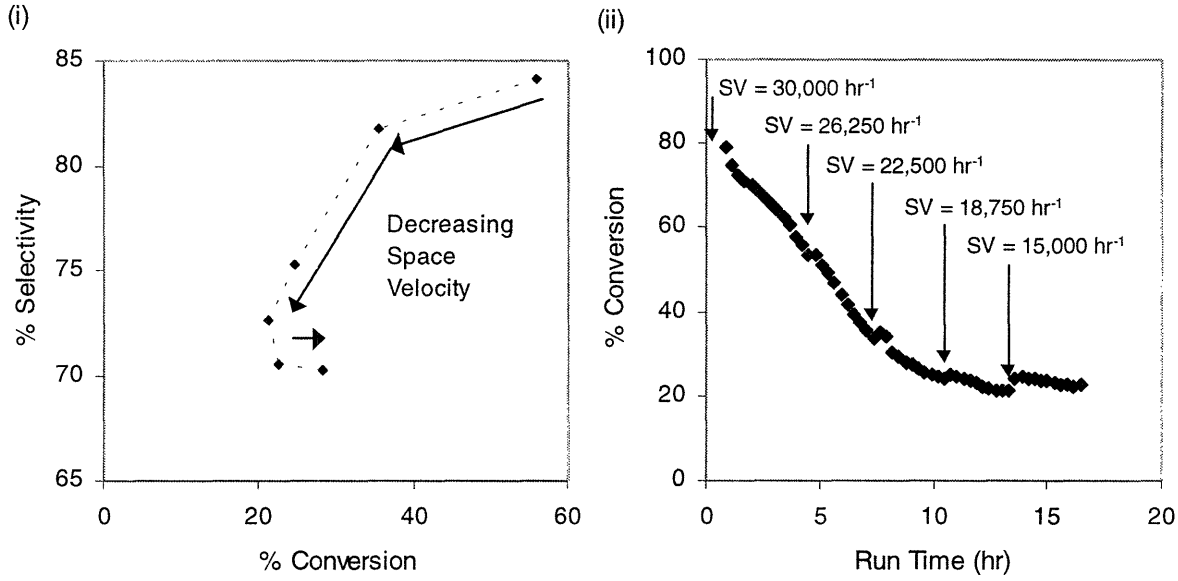

Figure 3.15. (i) Selectivity versus conversion and (ii) conversion versus run time for LiCl/ Nd_2O_3/Si-doped SZ. Catalyst composition: 5 wt% Li, 5 wt% Nd_2O_3, Si/Zr = 0.01. C_2H_6:O_2:N_2/He = 0.1:0.1:0.8, 0.5 g catalyst, P = 1 atm, T = 650°C. Space velocities in (ii) were adjusted at the points noted with arrows.

by Wang *et al.*[3,4,5,6] for ODHE studies (60 mL/min), leaching effects might have been masked.

To counter the catalyst deactivation associated with LiCl, alternative alkali chloride salts were examined as promoters (see Figure 3.16). With the exception of the CsCl-promoted material, each catalyst exhibited the typical profile of decreasing selectivity with increasing conversion. Complete consumption of O_2 was observed, however, when testing the CsCl/CeO_2/Si-doped ZrO_2 catalyst, leading to deactivation of the catalyst over time due to coke formation. The LiCl-promoted material showedthe highest selectivities at high conversions. Other alkali promoters, however, demonstrated improved thermal stability (not shown). In addition to enhanced stability, NaCl exhibited high selectivities at low conversions. We therefore explored the possibility of adding small quantities of NaCl to reduce LiCl leaching. Moreover, we have previously shown that catalyst activity for ODHE could be roughly correlated to the molten salt transition temperature. For alkali chlorides other than LiCl, this transition would typically occur well above the ODHE reaction conditions (e.g. at ~ 800°C for NaCl). By forming molten salt mixtures such as LiCl/NaCl, however, the transition temperature could be drastically reduced. Thus, otherwise inactive

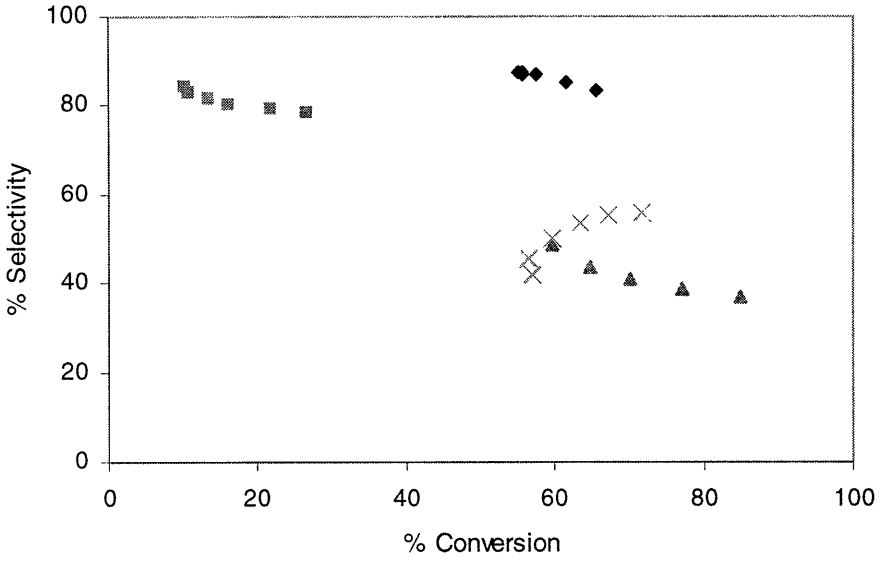

Figure 3.16. Selectivity versus conversion for CeO_2/Si-doped SZ impregnated with (♦) LiCl, (■) NaCl, (▲) KCl and (×) CsCl. Catalyst composition: 5 wt% alkali, 5 wt% CeO_2, Si/Zr = 0.05. C_2H_6:O_2:N_2/He = 0.1:0.1:0.8, 0.5 g catalyst, P = 1 atm, T = 650°C. Coking was observed in the CsCl-promoted catalyst, leading to a steady decline in ODHE conversion.

compounds such as NaCl might give high activity in combination with LiCl. To test this hypothesis, a series of LiCl catalysts (with 5 wt% Li) were co-impregnated with NaCl (with 1–10 wt% Na loadings) (Figure 3.17). Although all catalysts still experienced an initial period of deactivation, the incorporation of even small quantities of Na has a dramatic stabilizing effect on the catalyst conversion. While materials with higher Na contents gave initially lower conversions, their ability to suppress LiCl leaching resulted in excellent performance in the long run. The effectiveness of NaCl in preventing Li loss was verified via post-reaction elemental analyses (see Table 3.3).

To test whether NaCl activity was enhanced by the formation of a molten salt mixture, an alternative composition, NaCl/KCl, was employed. This allowed us to remove the convoluting effects of LiCl activity. Compared to the maximum conversion of 26% observed over NaCl/CeO_2/Si-doped SZ (5 wt% Na), NaCl/KCl/CeO_2/Si-doped SZ (5 wt% Na, 1.10 wt% K) attained ~ 48% conversion (Figure 3.18). Moreover, the selectivity corresponding to maximum conversion was increased from 78% to ~ 90% with the use of the NaCl/KCl mixture. At an increased K loading of 3.35 wt%, a small decline in catalyst selectivity was observed. Most likely, this was due to the high KCl content in this sample,

as the exposure of isolated KCl would result in a much lower ODHE selectivity (see Figure 3.16).

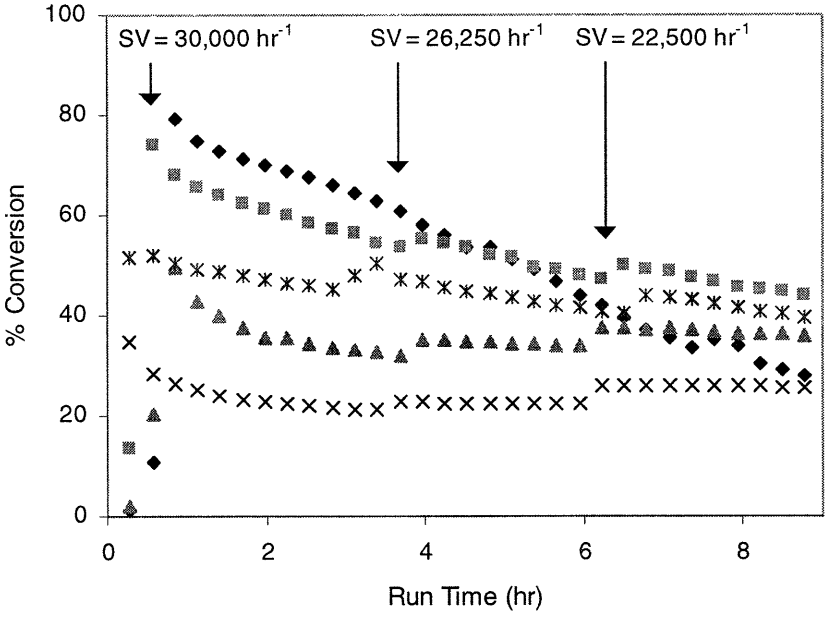

Figure 3.17. Conversion versus run time for $LiCl/Nd_2O_3$/Si-doped SZ co-impregnated with (♦) 0, (■) 1, (*) 3, (▲) 5 and (×) 10 wt% Na (nominal loadings). Catalyst composition: 5 wt% Li, 5 wt% Nd_2O_3, Si/Zr = 0.01. C_2H_6:O_2:N_2/He = 0.1:0.1:0.8, 0.5 g catalyst, P = 1 atm, T = 650°C. Space velocities were adjusted at the points noted with arrows.

Table 3.3. Pre- and post-reaction elemental analyses of Li contents in $LiCl/NaCl/Nd_2O_3$/Si-doped SZ catalysts* with different initial Na loadings.

Nominal Na Loading (wt%)	Li Content (wt%)**	
	Pre-reaction	Post-reaction***
0	2.57	0.79
1	2.56	0.83
5	1.89	1.40
10	1.92	1.45

* Catalyst composition: 5 wt% Li, 5 wt% Nd_2O_3, Si/Zr = 0.01.
** Results from AA/ICP analysis (Desert Analytics, Tucson, AZ).
*** Samples analyzed after experiments of Figure 3.17.

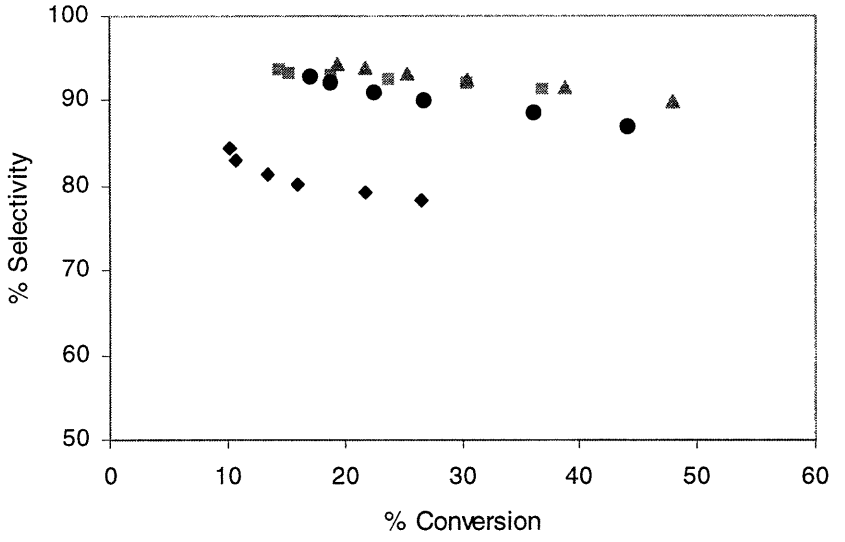

Figure 3.18. Selectivity versus conversion for NaCl/CeO_2/Si-doped SZ co-impregnated with (♦) 0.00, (■) 0.37, (▲) 1.10 and (●) 3.35 wt% K. Catalyst composition: 5 wt% Na, 5 wt% CeO_2, Si/Zr = 0.05. C_2H_6:O_2:N_2/He = 0.1:0.1:0.8, 0.5 g catalyst, P = 1 atm, T = 650°C.

3.3.5 ODHE Performance of Si-doped ZrO_2-based Nanocomposite Catalysts

Due its superior stability and ODHE performance, our subsequent examinations were focused on the Si-doped ZrO_2 nanocomposite catalysts containing the LiCl/NaCl mixture. For this system, we would like to identify the optimal Si loading level, and the nature and role of Si. First, we need to address the question of whether Si was truly doped within the ZrO_2 matrix or formed separate domains of SiO_2. The majority of prior research conducted on SiO_2-ZrO_2 binary mixtures has focused on materials with high Si contents (> 30%),[36,37] which were depicted as small domains of zirconia surrounded by an amorphous silica matrix. Recently, Del Monte *et al.*[21,22] have extended this picture to systems with low Si loadings.[vii] They have also reported that silica evolved from the composite at elevated temperatures.[22] This was illustrated by a shift in the characteristic infrared Si–O–Zr band and the evolution of a silanol peak for a series of Si-doped ZrO_2 samples calcined at increased temperatures.

In contrast to Del Monte *et al.*'s findings, TEM images (not shown) of our Si-doped SZ (Si/Zr = 0.05) displayed neither an amorphous silica coating around the particles, nor a

[vii] Evidence for this, however, seemed largely circumstantial: no silica coating was detected in the TEM images of a 2 at% Si-doped ZrO_2 composite. Furthermore, ^{29}Si NMR spectra as well as FTIR data did not show any evidence of a condensed SiO_2 network.

bulk SiO_2 phase. To corroborate these findings, XPS was also performed on Si-doped ZrO_2. By comparing XPS results to bulk composition analysis, we hoped to determine whether the slower hydrolysis/condensation rate of Si alkoxide resulted in thin SiO_2 coatings on the zirconia particles' surface. Bulk analysis via ICP/AA (Desert Analytics, Tucson, AZ) of the Si-doped ZrO_2 material revealed a Si/Zr ratio of 0.0856 ± 0.0057. Meanwhile, a Si/Zr surface ratio of 0.0845 was measured by XPS. Since surface enrichment of Si was not detected via XPS, we believed that Si was effectively doped into the ZrO_2 support using our synthesis method.

To determine the temperature at which silica evolved as a separate phase, Si-doped ZrO_2 (Si/Zr = 0.05) was calcined at 500°C, 600°C, 700°C, 900°C and 1000°C. XPS results in Table 3.4 suggested that significant surface silica evolution did not occur until > 700°C, which was above the maximum temperatures employed in our ODHE studies. Photoacoustic FTIR spectra (Figure 3.19) of samples calcined at ≤ 700°C exhibited the Si–O–Zr band[36] at 825 cm^{-1}, indicative of good homogeneity. The appearance of the silanol stretching mode[22,36] at 1050 cm^{-1}, which del Monte *et al.*[21,22] associated with the evolution of SiO_2, was only observed in the spectra of the 900°C- and 1000°C-calcined samples. These results verified that our composite supports were stable under the ODHE reaction conditions.

Table 3.4. XPS surface Si/Zr atomic ratio in Si-doped ZrO_2 (nominal Si/Zr ratio = 0.05) calcined at various temperatures.

Temperature (°C)	Si/Zr Atomic Ratio
500	0.0739
600	0.0777
700	0.0845
900	0.1750
1000	0.2265

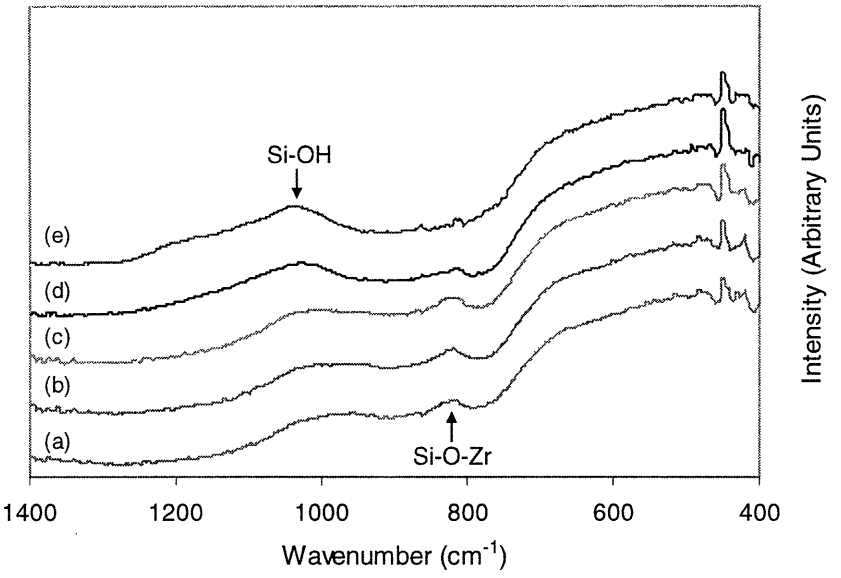

Figure 3.19. Photoacoustic FTIR spectra for Si-doped ZrO_2 (Si/Zr = 0.05) calcined at (a) 500°C, (b) 600°C, (c) 700°C, (d) 900°C and (e) 1000°C.

In our initial catalyst screening, a dopant/Zr atomic ratio of 0.05 was selected. We hypothesized that this value was large enough to reveal dopant effects, yet small enough to prevent secondary oxide formation. In Figure 3.20, we compare the ODHE performance of catalysts doped at alternative Si/Zr ratios. In agreement with earlier screening trials, we observed that the introduction of Si resulted in greatly enhanced ODHE selectivity versus LiCl/NaCl/Nd_2O_3/SZ. The catalyst with Si/Zr = 0.01 displayed the highest activity at 550–650°C. Intermediate Si/Zr ratios of 0.03–0.05 were found to exhibit the highest selectivities at 650°C. With the exception of the catalyst with Si/Zr = 0.10, selectivities for the Si-doped ZrO_2-based catalysts were found to increase with increasing reaction temperature before stabilizing at $T \geq 600$°C. This asymptotic rise in selectivity with temperature might be indicative of the necessity for LiCl to exist in the liquid form. Of the various Si-doped ZrO_2 catalysts tested, only the catalyst with Si/Zr = 0.10 exhibited a molten salt transition temperature significantly below 550°C (not shown). Increases in conversion with temperature were not accompanied by significant reductions in selectivity, suggesting that ethene combustion was not substantial at these conversions. At conversions approaching 30%, the ethene selectivity of the catalyst with Si/Zr = 0.05 exceeded 92%, compared to the 78.9% selectivity of LiCl/NaCl/Nd_2O_3/SZ. Since our emphasis was on materials with high

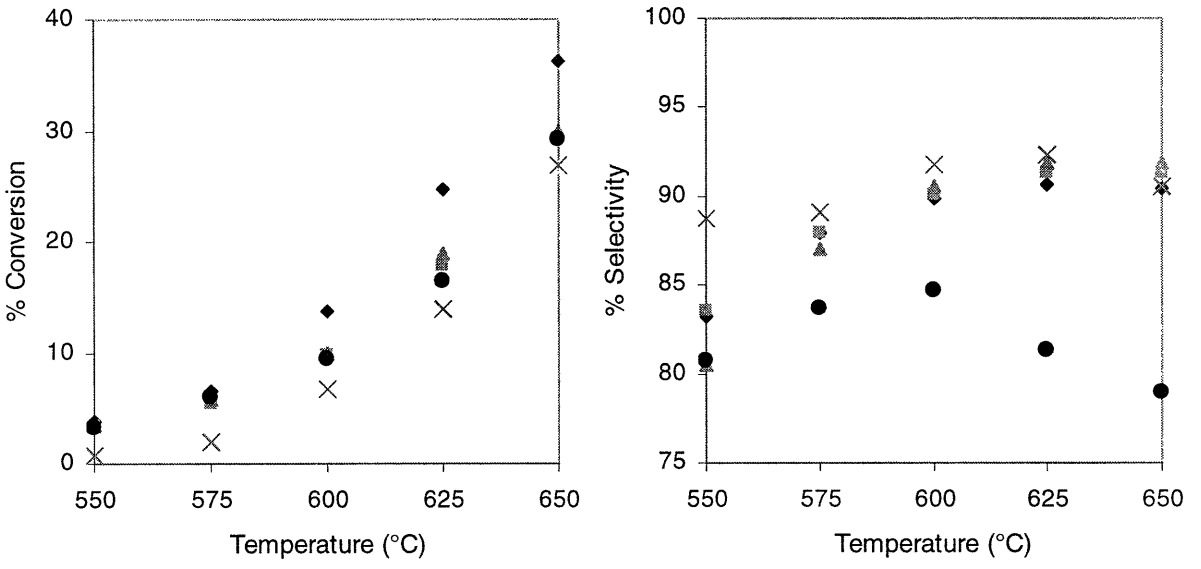

Figure 3.20. Conversion and selectivity versus temperature for LiCl/NaCl/Nd_2O_3/Si-doped SZ with Si/Zr of (●) 0.00, (♦) 0.01, (■) 0.03, (▲) 0.05 and (×) 0.10. Catalyst composition: 5 wt% Li, 5 wt% Na, 5 wt% Nd_2O_3. Flowrate = 60 mL/min, C_2H_6:O_2:N_2/He = 0.1:0.1:0.8, 0.25 g catalyst, P = 1 atm.

ODHE selectivity, a Si/Zr ratio of 0.05 was selected for further studies in subsequent sections.

The enhanced ODHE performance of the Si-doped catalysts versus LiCl/NaCl/Nd_2O_3/SZ could be attributed to the physical and chemical changes brought about by Si introduction. The XRD crystallite sizes, BET surface areas and SO_4^{2-} contents (quantified by TGA decomposition studies) for the various Si-doped catalysts are presented in Table 3.5. Reduced ZrO_2 grain sizes were observed with increased Si loadings. This, in turn, translated into larger support surface areas, which accommodated more sulfate anions, promoting improved lithium dispersion. Surface area effects alone, however, could not completely account for the conversion profiles observed. As seen in Figure 3.20, increasing Si/Zr ratios beyond 0.01 resulted in lower conversions, although they gave rise to larger surface areas.

Since the nature of the chemical synergism between the support and LiCl was established earlier to be an acid-base interaction, we tried to isolate the effect of the Si dopant on SZ by measuring the sulfate binding energetics of Si-doped SZ. The kinetics of

Table 3.5. XRD crystallite sizes, BET surface areas and SO_4^{2-} contents of LiCl/NaCl/Nd_2O_3/Si-doped SZ catalysts.*

Si/Zr Atomic Ratio**	ZrO_2 Grain Size (nm)	Catalyst Surface Area (m^2/g)	SO_4^{2-} Content (wt%)
0.00	46.9	11.0	2.77 ± 0.27
0.01	35.3	18.6	2.82 ± 0.11
0.03	16.6	22.2	2.78 ± 0.05
0.05	15.2	28.4	3.02 ± 0.08
0.10	15.0	24.2	3.15 ± 0.13

* Catalyst composition: 5 wt% Li, 5 wt% Na, 5 wt% Nd_2O_3.
** Nominal Si doping levels.

sulfate decomposition were measured via TGA at 775°C, 800°C, 825°C and 850°C. Table 3.6 shows that the initial doping of Si resulted in a significant decrease in the activation energy for sulfate decomposition from 65.0 to 36.8 kJ/mol. As the Si/Zr ratios were increased to 0.03, 0.05 and 0.10, the activation energies were increased to 52.0, 47.1 and 54.1 kJ/mol, respectively. The changes in desorption energetics appeared to correlate quite well to the trends observed in the catalyst activity shown in Figure 3.20. Thus, we concluded that the introduction of Si dopant altered the strength of sulfate interaction with the ZrO_2 support, which in turn affected the SZ support's interaction with the impregnated LiCl and NaCl.

Table 3.6. Energetics of sulfate decomposition for Si-doped SZ.

Si/Zr Atomic Ratio*	Activation Energy (kJ/mol)
0.00	65.0
0.01	36.8
0.03	52.0
0.05	47.1
0.10	54.1

* Nominal Si doping levels.

3.3.6 ODHE Performance of Nanocomposite Catalysts with Different Secondary Metal Oxides

A number of researchers[6,7,8,38] have determined that the introduction of small quantities of metal oxide in conjunction with lithium would enhance partial oxidation activity without significantly decreasing selectivity. While other metal oxides (i.e., Co and Sn oxides) have been shown to enhance performance, we elected to focus on the rare earth oxides. Despite the reported success of Dy_2O_3 and Nd_2O_3, a systematic study of the rare earth oxides has not been undertaken. Moreover, since different researchers have used their own methods for metal oxide introduction, their conclusions sometimes conflicted with each other. Thus, the function(s) of the secondary metal oxide remained uncertain. Besides possible chemical modification of the catalyst, secondary metal oxides might give rise to changes in catalyst surface area, formation of new crystalline phases, and improved lithium retention.

Figure 3.21 shows the activation curves for LiCl/NaCl/Si-doped SZ catalysts impregnated with a variety of rare earth oxides. Most catalysts showed similar activation curves, with the exception of those impregnated with Pr_xO_y and Nd_2O_3. The low-temperature activity of the Nd_2O_3-impregnated catalyst was superior, but the Pr_xO_y-impregnated catalyst exhibited the best conversion at 650°C. XRD results (not shown) suggested the sharp increase in Pr_xO_y activity was associated with the decomposition of praseodymium carbonate, which suppressed the catalytic activity at lower temperatures. Selected catalysts were subjected to further testing (see Figure 3.22). We note that the Nd_2O_3-impregnated catalyst exhibited relatively low selectivities under high conversions. The Pr_xO_y-impregnated catalyst was able to achieve very high conversions of > 80%. Overall, the CeO_2-impregnated LiCl/NaCl/Si-doped SZ exhibited the best selectivity-conversion trajectory.

Table 3.7 shows that the surface areas of the various catalysts did not vary significantly and could not explain the different conversions observed. The post-reaction lithium contents of the catalysts also did not differ substantially, although the higher Li content of the Pr_xO_y-impregnated catalyst might be partially responsible for the greater conversions achieved. The low Li content in the Nd_2O_3-impregnated catalyst might have contributed to its lower selectivity. We explored the possibility that the impregnated

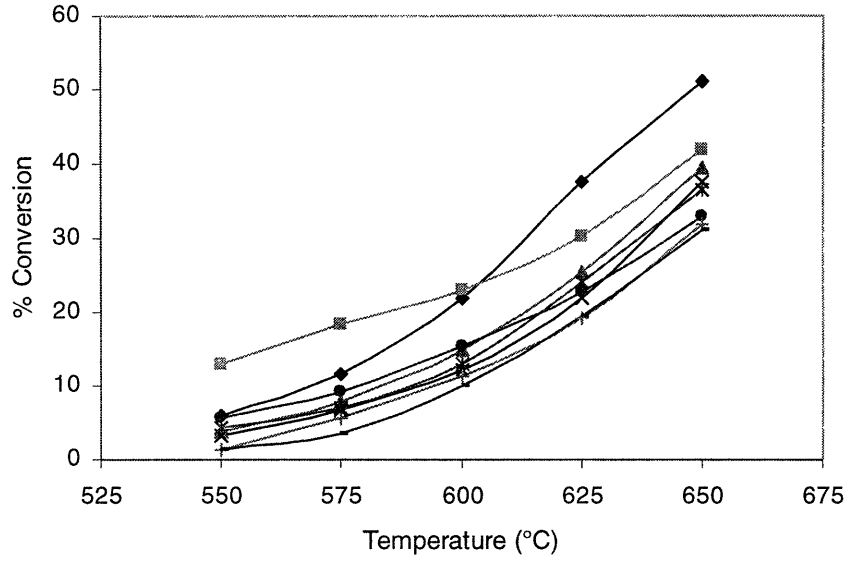

Figure 3.21. Conversion versus temperature for LiCl/NaCl/Si-doped SZ catalysts impregnated with 5 wt% (♦) Pr_xO_y, (■) Nd_2O_3, (▲) Gd_2O_3, (×) La_2O_3, (*) CeO_2, (•) Dy_2O_3, (+) Sm_2O_3 and (-) Eu_2O_3. Catalyst composition: 5 wt% Li, 5 wt% Na, Si/Zr = 0.05. Flowrate = 60 mL/min, C_2H_6:O_2:N_2/He = 0.1:0.1:0.8, 0.25 g catalyst, P = 1 atm.

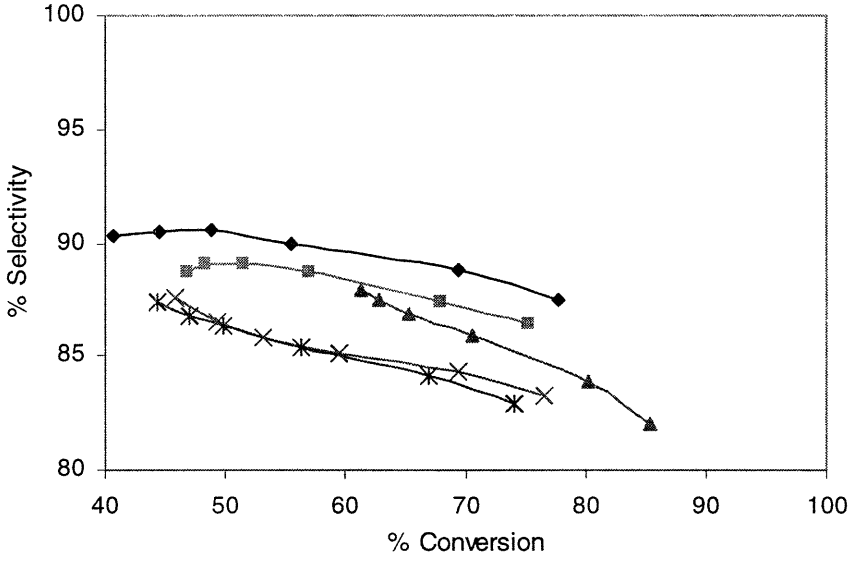

Figure 3.22. Selectivity versus conversion for LiCl/NaCl/Si-doped SZ catalysts impregnated with 5 wt% (♦) CeO_2, (■) Gd_2O_3, (▲) Pr_xO_y, (×) La_2O_3 and (*) Nd_2O_3. Catalyst composition: 5 wt% Li, 5 wt% Na, Si/Zr = 0.05. C_2H_6:O_2:N_2/He = 0.1:0.1:0.8, 0.5 g catalyst, P = 1 atm, T = 650°C.

metal oxide acted as an activating material, given its readily available source of active oxygen atoms. If this was indeed the case, the activity of the pure metal oxides would serve

as a good guide to the catalyst activity. Table 3.7 shows the ethane consumption rates of the pure oxides, as normalized by the oxide surface areas. As the pure metal oxides were highly reactive, the ODHE reaction was run at 400°C using a minimal amount of catalyst (~ 100 mg). We observed a positive correlation between the ethane consumption rates of the pure metal oxides and the ODHE conversion of the oxide-impregnated catalysts at 650°C, but the correlation was poor (R^2 = 0.22). The correlation improved at a lower ODHE temperature (600°C, R^2 = 0.35, T-stat = 1.78), suggesting that the metal oxide might be playing an activating role. At higher temperatures, gas-phase reactions might have convoluted this effect. The correlation between pure metal oxide activity and oxide-impregnated catalyst activity might also be influenced by the different reaction temperatures involved in the two studies. At lower temperatures, stable surface carbonate formation could poison the catalyst surface. XRD patterns of several metal oxides (La, Nd, Pr and Sm oxides) showed the presence of metal carbonates, which would certainly complicate the interpretation of catalyst functions.

Table 3.7. Characterization of LiCl/NaCl/Si-doped SZ catalysts impregnated with various metal oxides.*

Metal Oxide	Pure Metal Oxide Surface Area** (m^2/g)	Specific Pure Metal Oxide Reaction Rate*** ($mol/s \cdot cm^2$)	Catalyst Surface Area (m^2/g)	Li Content+ (wt%)	Catalyst ODHE Conversion++ (%)
Nd_2O_3	35.9	7.95E-5	20.7	2.54	22.9
CeO_2	29.2	6.12E-6	17.8	2.86	13.0
Gd_2O_3	21.5	1.60E-5	23.1	2.60	14.8
Eu_2O_3	19.6	4.19E-5	16.2	2.88	9.9
Dy_2O_3	27.0	2.68E-6	16.8	2.86	15.5
Pr_xO_y	34.5	5.64E-5	17.9	3.04	21.9
Sm_2O_3	39.9	3.39E-5	11.8	2.76	11.3
La_2O_3	28.4	5.19E-6	16.9	2.95	12.2

* Catalyst composition: 5 wt% Li, 3 wt% Na, 5 wt% metal oxide, Si/Zr = 0.05.
** Pure metal oxides calcined at 700°C.
*** Ethane consumption rate for pure metal oxides evaluated at 400°C.
+ Post-reaction Li content in catalysts.
++ ODHE conversion of catalyst evaluated at 600°C.

3.3.6.1 Effect of CeO_2 Loading

Having determined CeO_2 to be the optimal metal oxide, we then examined the impact of CeO_2 loading on catalyst performance. According to Korf *et al.*,[7] the co-impregnation of larger quantities of metal oxide would shift the reaction curve downwards in temperature. Thus, Wang *et al.*[6] found that higher loadings of Nd_2O_3 resulted in increased conversions for ODHE; corresponding decreases in ethene selectivity were also observed.

In Figure 3.23, we compare the performance of LiCl/NaCl/Si-doped SZ catalysts impregnated with different CeO_2 loadings. Interestingly, although conversions for catalysts with higher loadings were slightly greater, the selectivity-conversion trajectories of the catalysts did not vary substantially. Surprisingly, even at high loadings of CeO_2, selectivity of the catalysts did not decrease. Since CeO_2 was expected to combust ethane readily at these temperatures, the presence of LiCl must have suppressed such intrinsic CeO_2 oxidation characteristics.

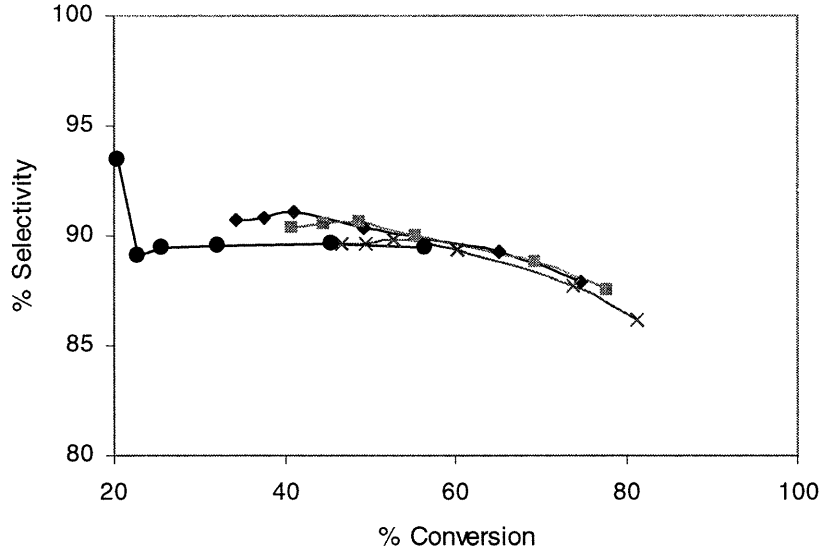

Figure 3.23. Selectivity versus conversion for LiCl/NaCl/Si-doped SZ catalysts impregnated with (●) 0.0, (♦) 2.5, (■) 5.0 and (×) 10 wt% CeO_2. Catalyst composition: 5 wt% Li, 5 wt% Na, Si/Zr = 0.05. C_2H_6:O_2:N_2/He = 0.1:0.1:0.8, 0.5 g catalyst, P = 1 atm, T = 650°C.

3.3.7 Optimization of Sol-Gel Processing of Nanocomposite Catalysts

To improve upon the ODHE performance of our Si-doped ZrO_2 nanocomposite catalyst (Si/Zr = 0.05), a series of optimization experiments was performed, focusing on the

various sol-gel parameters in synthesis. In applying sol-gel techniques to multicomponent materials synthesis, one major concern is the different hydrolysis and polycondensation rates of different metal alkoxides. Alkoxide precursors of metals with relatively low electronegativities (e.g. zirconium) undergo rapid hydrolysis and condensation. Since silicon alkoxides hydrolyze relatively slowly, formation of homogeneous silica-zirconia nanocomposites is difficult. To achieve homogeneous nanocomposites, alternative alkoxide precursors, modification of the water:alkoxide ratio,[viii] changes in the sol pH, and prehydrolysis of the Si alkoxide were examined.

3.3.7.1 Effect of Si Alkoxide Precursor

Metal alkoxides react with water due to the polar nature of the M-OR bonds. The strong electron-withdrawing properties of alkoxy groups result in metal atoms that are electrophilic in nature. This, in turn, facilitates nucleophilic attack by water molecules in the hydrolysis process. By increasing the size of the alkyl chain, the partial positive charge on the metal atom is reduced. Sterically bulky alkoxy groups also hinder the initial nucleophilic attack by water. Thus, precursors with larger alkoxyl groups have slower hydrolysis rates. Chen *et al.*[39] have also shown that the condensation rate decreases with larger alkyl chains.

We have synthesized LiCl/NaCl/CeO_2/Si-doped SZ catalysts using two different silicon alkoxides, tetraethoxysilane (TEOS) and tetramethoxysilane (TMOS). Improved ODHE selectivities were observed with the TMOS-derived catalyst (see Figure 3.24). The TMOS-derived catalyst displayed lower activity due in part to its lower surface area (15.9 m^2/g) compared to the TEOS-derived catalyst (21.6 m^2/g). Further tests using a larger quantity of the TMOS-derived catalyst (0.65 g instead of 0.5 g) confirmed that at equivalent conversions, the TMOS-derived catalyst possessed superior selectivity (see Figure 3.24). Photoacoustic FTIR spectra indicated that a higher loading of Si was incorporated by using a TMOS precursor (not shown). Thus, Si alkoxide hydrolysis and condensation were accelerated by the use of a smaller alkoxyl group, leading to improved Si incorporation and chemical homogeneity.

[viii] The impact of water:alkoxide ratio was determined to be fairly minor and the results will not be presented.

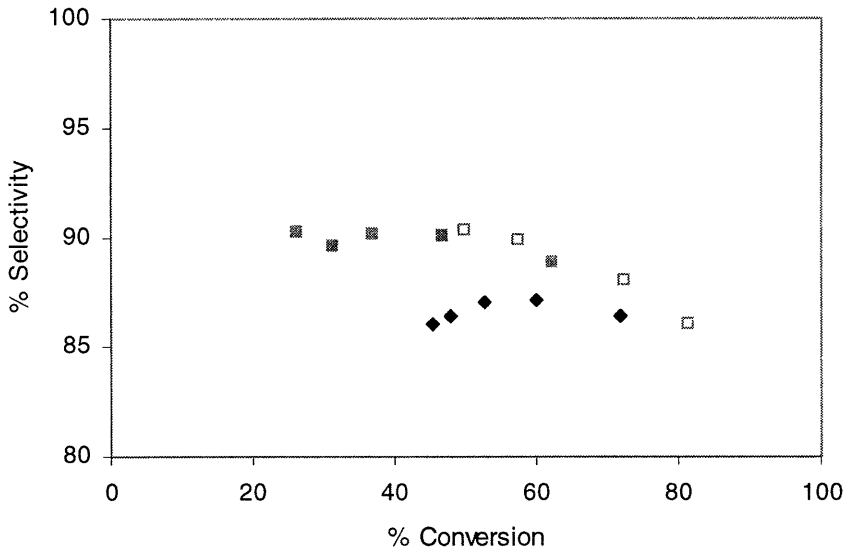

Figure 3.24. Selectivity versus conversion for LiCl/NaCl/CeO_2/Si-doped SZ synthesized using (♦) TEOS and (■,□) TMOS precursors. Catalyst composition: 5 wt% Li, 5 wt% Na, 5 wt% CeO_2, Si/Zr = 0.05. C_2H_6:O_2:N_2/He = 0.1:0.1:0.8, (♦,■) 0.5 g or (□) 0.65 g catalyst, P = 1 atm, T = 650°C.

3.3.7.2 Effect of Sol pH

The addition of small quantities of acid and base has been demonstrated to catalyze sol-gel reactions.[40] Acids such as HNO_3 have been introduced during hydrolysis to facilitate proton donation to the alkoxo leaving group, significantly increasing the hydrolysis rate. During condensation, protonation most likely occurs at the terminal alkoxo groups based on charge distribution analyses. The end result is a highly linear material. The outcome of base-catalyzed sol-gel synthesis varies depending on the particular base employed. Coordination or nucleophilic addition can occur, resulting in either a decrease or an increase in the charge density of the metal atom, which influences the hydrolysis rate. The condensation rate is always enhanced under basic conditions since the formation of $M\text{-}O^-$ species facilitates subsequent nucleophilic attack. Materials synthesized under basic conditions are highly crosslinked.[40,41]

ODHE results for LiCl/NaCl/CeO_2/Si-doped SZ catalysts synthesized under various pH conditions are shown in Figure 3.25. Data for $[HNO_3]/[M]$ = 1.0 are not shown since condensation did not occur in that case. The catalyst synthesized at $[HNO_3]/[M]$ = 0.05 displayed inferior ODHE performance. The poor performance of this material could not be

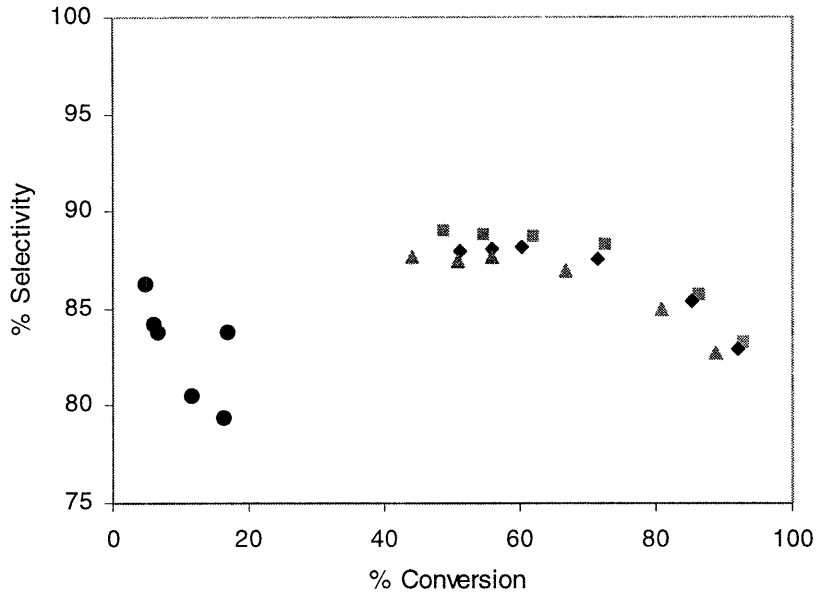

Figure 3.25. Selectivity versus conversion for LiCl/NaCl/CeO_2/Si-doped SZ synthesized with (•) $[HNO_3]/[M] = 0.05$, (▲) no acid or base catalyst, (♦) $[NH_4OH]/[M] = 0.05$ and (■) $[NH_4OH]/[M] = 1.0$, where [M] represents the total cation concentration, $[Si^{4+} + Zr^{4+}]$. Catalyst composition: 5 wt% Li, 5 wt% Na, 5 wt% CeO_2, Si/Zr = 0.05. C_2H_6:O_2:N_2/He = 0.1:0.1:0.8, (•) 0.5 g or (▲,♦,■) 0.75 g catalyst, P = 1 atm, T = 650°C.

ascribed to either the catalyst surface area or sulfate loading (see Table 3.8), which were comparable to the other samples. It was most likely due to the lower degree of Si dopant incorporation, which was indicative of poorly matched reaction rates between the TEOS and

Table 3.8. Characteristics of LiCl/NaCl/CeO_2/Si-doped SZ catalysts* synthesized with acid or base.

$[H^+]/[M]$** or $[OH^-]/[M]$	Sol-Gel Catalyst	Catalyst Surface Area (m^2/g)	SO_4^{2-} Content (wt%)	Si Incorporation*** (wt%)
0.05	HNO_3	15.3	2.85	1.18
—	—	21.6	2.77	1.23
0.05	NH_4OH	23.5	2.55	1.24
1.00	NH_4OH	17.5	3.24	1.36

* Catalyst composition: 5 wt% Li, 5 wt% Na, 5 wt% CeO_2, Si/Zr = 0.05.
** [M] represents the total molar cation concentration, $[Si^{4+} + Zr^{4+}]$.
*** As determined by ICP/AA.

the Zr n-propoxide precursors at low pH. In contrast, the base-catalyzed materials exhibited superior ODHE performance. Under basic conditions, the hydrolysis and condensations rates were both increased for the alkoxide precursors. This led to improved Si incorporation versus the acid-catalyzed material and an improved chemical homogeneity similar to that observed in the TMOS-derived catalyst.

3.3.7.3 Optimal Catalyst Performance

Figure 3.26 shows the performance of two of our best LiCl/NaCl/CeO_2/Si-doped SZ catalysts (5 wt% Li, 5 wt% Na, 5 wt% CeO_2, Si/Zr = 0.05, water:alkoxide = 5), one prepared using a TMOS precursor and the other prepared with a basic catalyst ([NH_4OH]/[M] = 1.0). For comparison, two runs using 0.5 g and 0.75 g of LiCl/Nd_2O_3/SZ were performed. Interestingly, they displayed different selectivity-conversion trajectories. This was in contrast to the observed behavior of our nanocomposite catalysts, wherein the selectivity-conversion trajectories remained similar for runs using different amounts of catalyst. This was because the rapid LiCl loss over LiCl/Nd_2O_3/SZ was prevented over our optimized catalysts. The LiCl/NaCl/CeO_2/Si-doped SZ synthesized with a basic catalyst

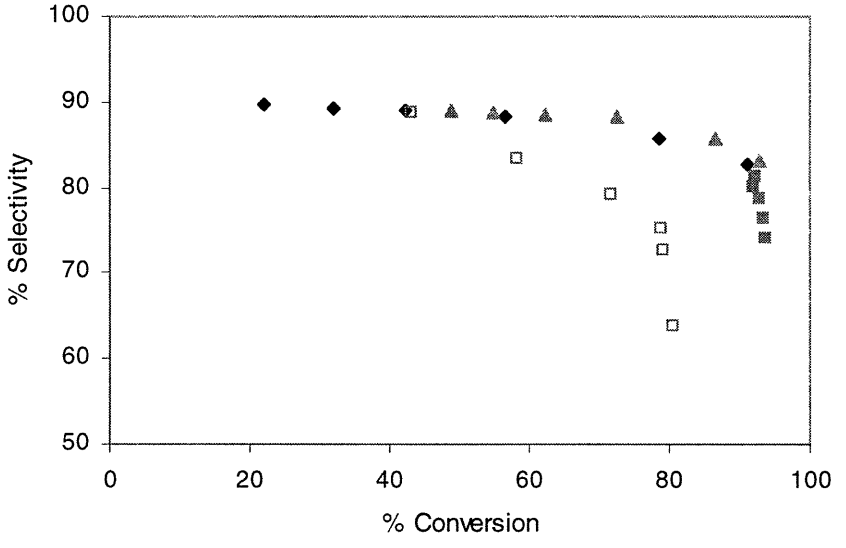

Figure 3.26. Selectivity versus conversion for LiCl/NaCl/CeO_2/Si-doped SZ prepared with (▲) [NH_4OH]/[M] = 1.0 and (♦) TMOS precursor, and (□,■) LiCl/Nd_2O_3/SZ. Catalyst composition: (▲,♦) 5 wt% Li, 5 wt% Na, 5 wt% CeO_2, Si/Zr = 0.05; (□,■) 5 wt% Li, 5 wt% Nd_2O_3. C_2H_6:O_2:N_2/He = 0.1:0.1:0.8, (□) 0.5 g or (▲,♦,■) 0.75 g catalyst, P = 1 atm, T = 650°C.

performed slightly better than that derived from TMOS, achieving an excellent yield of 77.2% from 92.8% conversion and 83.2% selectivity. These values clearly exceeded the target for economic viability (yield: 56%). Our optimized system demonstrated superior performance to $LiCl/Nd_2O_3/SZ$ under the same reaction conditions and displayed far better stability than Wang *et al.*'s catalysts.[3,4,5,6]

3.4 Summary

Wang *et al.*'s $LiCl/Nd_2O_3/SZ$ catalyst has demonstrated superb ODHE performance. We attributed the excellent activity of this catalyst to two effects. Firstly, we have found that the impregnation of SO_4^{2-} (as well as MoO_x and WO_x) anions would suppress grain growth, leading to a nanocrystalline, high surface area ZrO_2 support that provided for an optimal lithium dispersion. Secondly, through DRIFT studies of pyridine adsorption, we have established that a strong acid-base interaction existed between the SZ support and LiCl. This interaction further resulted in a reduction in the molten salt transition temperature for LiCl, which was correlated to enhanced catalyst activity.

To further improve catalyst conversion and selectivity, we have examined means of manipulating the Li-support interaction. We investigated alternative solid acid catalyst supports, namely MoO_x/ZrO_2 and WO_x/ZrO_2, instead of SZ. The use of MoO_x and WO_x allowed for a superior control of anion surface density and the synthesis of catalysts with comparable ODHE performance as $LiCl/Nd_2O_3/SZ$ at low conversions. However, the performance of MoO_x/ZrO_2 and WO_x/ZrO_2 impregnated with LiCl and Nd_2O_3 was found to degrade more quickly at high conversions compared to $LiCl/Nd_2O_3/SZ$. Alternatively, we attempted to modify the Li-support interaction through the doping of ZrO_2. The resulting $LiCl/Nd_2O_3$/doped SZ nanocomposite catalysts demonstrated enhanced activity, selectivity and stability.

Si-doped nanocomposites, in particular, were found to exhibit exceptional ODHE performance. TEM, XPS and photoacoustic FTIR results verified that the Si was truly doped into the ZrO_2 matrix instead of forming a separate SiO_2 phase. The Si dopant was shown to affect the sulfate interaction with the ZrO_2 support, altering its solid acid strength. Kinetic studies of Si-doped SZ showed a decrease in the activation energy for sulfate decomposition with Si doping, which corresponded to a significant increase in ODHE

activity. We have also impregnated the nanocomposite catalysts with secondary metal oxides from the lanthanide series instead of Nd_2O_3. CeO_2 was found to be the optimal secondary metal oxide. Increased CeO_2 loadings were found to improve the catalyst activity, without compromising the ODHE selectivity. Lastly, a number of sol-gel synthesis parameters was examined, including water:alkoxide ratio, alkoxide precursor and sol pH. Improvements in catalyst surface area and homogeneity were achieved through optimization of the sol-gel synthesis parameters, giving rise to enhanced catalytic activity and selectivity.

While initially very active for ODHE, $LiCl/Nd_2O_3/SZ$ was found to deactivate rapidly due to the loss of LiCl, requiring large quantities of catalyst to maintain stable performance. In contrast, our nanocomposite catalysts exhibited greater stability. We have further co-impregnated our nanocomposites with 5 wt% Na to successfully enhance catalyst stability and performance for ODHE. The formation of LiCl/NaCl binary mixtures on the surface allowed us to adjust the molten salt transition temperature of NaCl, which would otherwise be too high for ODHE activity, while preventing LiCl leaching. Our $LiCl/NaCl/CeO_2$/Si-doped SZ catalysts showed superior catalytic stability to $LiCl/Nd_2O_3/SZ$, with changes of less than 3% versus 15.9% conversion for $LiCl/Nd_2O_3/SZ$ over a 12-hr period (not shown). Using our optimized $LiCl/NaCl/CeO_2$/Si-doped SZ (Si/Zr = 0.05) catalyst, promising conversions of > 92% were achieved with ethene selectivities in excess of 83%, with a maximum ODHE yield of 77%.

3.5 References

[1] Conway, S. J., and Lunsford, J. H., *J. Catal.* **131**, 513 (1991).

[2] Burch, R., and Crabb, E. M., *Appl. Catal. A* **97**, 49 (1993).

[3] Wang, S., Murata, K., Hayakawa, T., Hamakawa, S., and Suzuki, K., *Catal. Lett.* **59**, 173 (1999).

[4] Wang, S., Murata, K., Hayakawa, T., Hamakawa, S., and Suzuki, K., *Chem. Comm.* **2**, 221 (1997).

[5] Wang, S., Murata, K., Hayakawa, T., Hamakawa, S., and Suzuki, K., *J. Chem. Tech. Biotech.* **74**, 988 (1999).

[6] Wang, S., Murata, K., Hayakawa, T., Hamakawa, S., and Suzuki, K., *Catal. Lett.* **62**, 191 (1999).

[7] Korf, S. J., Roos, J. A., Veltman, L. J., Vanommen, J. G., and Ross, J. R. H., *Appl. Catal.* **56**, 119 (1989).

[8] Conway, S. J., Wang, D. J., and Lunsford, J. H., *Appl. Catal.* **79**, L1 (1991).

[9] Hino, M., Kobayashi, S., and Arata, K., *J. Am. Chem. Soc.* **101**, 6439 (1979).

[10] Bensitel, M., Saur, O., and Lavalley, J. C., *Mater. Chem. Phys.* **28**, 309 (1991).

[11] Morterra, C., Cerrato, G., Bolis, V., Ciero, S. D., and Signoretto, M., *J. Chem. Soc. Farad. Trans.* **93**, 1179 (1997).

[12] Arata, K. *Appl. Catal. A* **146**, 3 (1996).

[13] Corma, A., Martinez, A., and Martinez, C., *Appl. Catal. A* **144**, 249 (1996).

[14] Morterra, C., Cerrato, G., and Signoretto, M., *Catal. Lett.* **41**, 101 (1996).

[15] Farcasiu, D., and Liu, J. Q., *Appl. Catal. A* **128**, 97 (1995).

[16] Chen, K., Bell, A. T., and Iglesia, E., *J. Phys. Chem. B* **104**, 1292 (2000).

[17] Arata, K., and Hino, M., *Mater. Chem. Phys.* **26**, 213 (1990).

[18] Chen, K., Xie, S., Bell, A. T., and Iglesia, E., *J. Catal.* **195**, 244 (2000).

[19] Chen, K., Xie, S., Bell, A. T., and Iglesia, E., *J. Catal.* **198**, 232 (2001).

[20] Khodakov, A., Yang, J., Su, S., Iglesia, E., and Bell, A. T., *J. Catal.* **177**, 343 (1998).

[21] del Monte, F., Larsen, W., and Mackenzie, J. D., *J. Am. Ceram. Soc.* **83**, 1506 (2000).

[22] del Monte, F., Larsen, W., and Mackenzie, J. D., *J. Am. Ceram. Soc.* **83**, 628 (2000).

[23] Kung, H. H., *J. Solid State Chem.* **52**, 191 (1984).

[24] Sangar, N., and Ying, J. Y., Massachusetts Institute of Technology, unpublished results (2001).

[25] Toraya, H., Yoshimura, M., and Somiya, S., *J. Am. Ceram. Soc.* **67**, C-119 (1984).

[26] Lee, T. V., and Beck, S. R., *AIChE J.* **30**, 517 (1984).

[27] Li, C.-H., *AIChE J.* **31**, 1036 (1985).

[28] NIST, *NIST X-ray Photoelectron Spectroscopy Database*, 4 February 2003, < http://srdata.nist.gov/xps/> (26 June 2003).

[29] Parvulescu, V., Coman, S., Grange, P., and Parvulescu, V. I., *Appl. Catal. A* **176**, 27 (1999).

[30] Zaki, M. I., Hasan, M. A., Al-Sagheer, F. A., Pasupulety, L., *Coll. Surf. A* **190**, 261 (2001).

[31] Barton, D. G., Shtein, M., Wilson, R. D., Soled, S. L., and Iglesia, E., *J. Phys. Chem. B* **103**, 630 (1999).

[32] Kim, D. S., Ostromecki, M., and Wachs, I. E., *J. Molec. Catal. A: Chem.* **106**, 93 (1996).

[33] Kim, D. S., Wachs, I. E., and Segawa, K., *J. Catal.* **146**, 268 (1994).

[34] Kuba, S., Lukinskas, P., Grasselli, R. K., Gates, B. C., and Knozinger, H., *J. Catal.* **216**, 353 (2003).

[35] Xu, J., and Ying, J. Y., Massachusetts Institute of Technology, unpublished results (2001).

[36] Lopez, T., Navarrete, J., Gomez, R., Novaro, O., Figueras, R., and Armendariz, H., *Appl. Catal. A* **125**, 217 (1995).

[37] Gomez, R., Lopez, T., Tzompantzi, F., Garciafigueroa, E., Acosta, W., and Novaro, O., *Langmuir* **13**, 970 (1997).

[38] Ji, L., Liu, J., Chen, X., and Li, M., *React. Kinet. Catal. Lett.* **62**, 121 (1997).

[39] Chen, K. C., Tsuchiya, T., and Mackenzie, J. D., *J. Non-Cryst. Solids* **81**, 227 (1986).

[40] Brinker, C. J., and Scherer, G. W., "Sol-Gel Science: The Physics and Chemistry of Sol-Gel Processing." Academic Press, Boston, 1990.

[41] Ying, J. Y., Benziger, J. B., and Navrotsky, A., *J. Am. Ceram. Soc.* **76**, 2571 (1993).

Chapter 4 — Oxidative Dehydrogenation of Propane

4.1 Introduction

4.1.1 Vanadium- and Molybdenum-based Catalysts

Two of the most promising elements utilized in heterogeneous ODHP catalysts are vanadium and molybdenum, both of which have either been impregnated on supports or incorporated in binary composites. For instance, Kung and co-workers[1,2] reported propene yields in excess of 25% using a V/MgO catalyst. $K/Mo/SiO_2/TiO_2$ catalyst was shown by Watson and Ozkan[3] to exhibit yields of ~ 30%. Wang *et al.*,[4] in testing a variant of their $Nd_2O_3/LiCl/SZ$ ODHE catalyst, attained propene yields of ~ 10% in ODHP over a NiO/LiCl/SZ catalyst.

A wide variety of metal oxide supports (TiO_2, MgO, Al_2O_3, ZrO_2, etc...) have been examined with various VO_x and MoO_x surface densities.[5,6] Supported catalysts offer improved mechanical strength and thermal stability, avoiding the severe sintering often observed with pure V_2O_5 and MoO_3. VO_x and MoO_x supported on basic metal oxides exhibited superior alkene selectivities[6,7] that have been linked to changes in dispersion. For instance, agglomeration of VO_x to form bulk V_2O_5 has been found to occur at even low vanadium coverages on acidic metal oxide supports. In contrast, isolated VO_4 tetrahedra were still observed on basic supports at near monolayer coverage. In fact, at higher loadings on basic supports, the formation of metal vanadate and molybdate was preferred over the appearance of V_2O_5 and MoO_3. The issue of VO_x and MoO_x dispersion on supports has significant ramifications since both Chen *et al.*[5] and Khodakov *et al.*[6,8] have attributed superior ODHP performance to the greater delocalization abilities of larger MoO_x and VO_x domains.

ODHP catalyst activity has generally been correlated to the availability and reactivity of lattice oxygen. Kung[9] argues that the likelihood a catalyst forms a C-O bond with an adsorbed hydrocarbon determines one critical branching step in the degree of ODHP versus propane combustion. Should C-O bond formation occur, the result is either combustion or formation of unwanted oxygen-containing products (i.e., acetaldehyde), both of which would reduce the ODHP selectivity. One major concern in utilizing supported VO_x and MoO_x catalysts is that increasing catalyst activity requires the formation of large polydentate/bulk domains. Kung argues that at high VO_x surface densities, the presence of closely neighboring vanadate groups can facilitate surface combustion.[9] This has spurred research efforts toward alternative means of manipulating the surface oxygen reactivity, including the synthesis of mixed oxides.[9,10,11,12,13,14]

4.1.2 Alkali Modification

The introduction of alkali metals represents one attempt to improve vanadium- and molybdenum-based catalyst performance. Such metals have been employed in other partial oxidation processes, generally resulting in large selectivity increases accompanied by reductions in catalytic activity. Several researchers have explored the impact of alkali metal addition at both submonolayer[15] as well as multilayer coverages[16] of VO_x and MoO_x for ODHP. The molar ratios of alkali metals and Mo or V were typically maintained below 0.2 to avoid formation of alkali molybdates and vanadates. In titrating alkali metal oxides on MoO_x/ZrO_2, Chen *et al.*[15] have determined that the rate of propane consumption did not scale with a one-to-one poisoning of active sites. Therefore, it is unlikely that the impregnation of alkali species simply acted to block active sites. Grabowski *et al.*[16] have found from isopropanol decomposition studies that alkali impregnation would decrease the surface acidity. Among the various alkali metals examined, the extent of basic promotion was ranked in the order of decreasing electronegativity. Corresponding to the loss of surface acidity was an improvement in propene selectivity. Grabowski *et al.* have reported that at 10% conversion, the propene selectivity of various alkali-impregnated VO_x/TiO_2 catalysts increased in the order: $V/TiO_2 < Li/V/TiO_2 < K/V/TiO_2 < Rb/V/TiO_2$. Similar results were obtained by Chen *et al.*[15] with alkali-impregnated MoO_x/ZrO_2 catalysts. Both groups ascribed the increase in propene selectivity to a reduction in secondary propene combustion. Because of its π-bond, propene is more electron-rich than propane, leading to stronger interactions with acidic sites. Thus, a decrease in propene surface residence times would arise from a weakening of the Mo^{6+} acid strength.[15] A similar finding was reported by Martin *et al.*,[17] who observed no chemisorbed propene on a sodium-doped, titania-supported vanadium catalyst, unlike the corresponding sodium-free catalyst. By deconvoluting the surface rate parameters, Chen *et al.*[15] have determined that the ratio of secondary propene combustion versus oxidative dehydrogenation decreased with alkali addition. Thus, the selectivity-conversion trajectory for ODHP was altered by alkali addition. However, they have also determined that reductions in acid strength accompanying alkali addition would eventually cease to impact ODHP performance.

4.1.3 Homogeneous ODHP

Like ethene, propene is currently generated by homogeneous pyrolysis. Initiation of this radical-based mechanism occurs via cleavage of a C-C bond. The resulting radicals then promote further reaction, abstracting hydrogen from the remaining propane molecules. Two forms of propyl radicals are generated: a n-propyl radical and an isopropyl radical. The isopropyl radical is believed to undergo a C-H beta-scission to yield propene and a hydrogen radical, whereas the n-propyl radical tends to undergo C-C beta scission to give ethene and a methyl radical. The dehydrogenation of paraffins is strongly endothermic, requiring temperatures well above 600°C. By optimizing parameters such as reactor temperature, flow rate and propane-to-air ratio, Burch and Crabb have obtained propene yields as high as 18%.[18]

4.1.4 Coupled Heterogeneous-Homogeneous Systems

Given the ordinarily poor conversions of current heterogeneous catalysts, researchers have entertained the possibility of coupling heterogeneous and homogeneous oxidative dehydrogenation. Several of the best heterogeneous ODHP results, in fact, have been reported at higher reactor temperatures where catalyst-promoted homogeneous contributions could be occurring. Nguyen and Kung[2] were the first to attempt to characterize the surface enhancement of homogeneous reactions in ODHP by examining the impact of post-catalyst void volume on the performance of a V/MgO wafer. They hypothesized that the desorbed intermediates from the catalyst assisted in homogeneous oxidative pyrolysis. By isolating contributions from the catalyst and void volume, Nguyen and Kung determined that conversions for the combined catalyst wafer/void volume system were consistently higher than the sum of their independent contributions. Based on separate oxidative pyrolysis experiments, they also concluded that thermal effects could not adequately explain the additional conversion attained. By comparing their experimental results to a simple gas-phase model of the void volume, Nguyen and Kung indicated that the desorbed intermediates primarily responsible for activating homogeneous pathways were propyl radicals.[19]

4.1.5 Short Contact Time

Unlike the traditional packed-bed approaches, Schmidt and co-workers[20,21] have explored the use of Pt-coated α-Al_2O_3 monoliths for ODHP in short contact time reactions. By controlling

factors such as diluent concentration, gas preheating, flow rate and propane:oxygen ratio, they have obtained autothermal reaction at ~ 1000°C, resulting in the highly selective transformation of propane to propene and ethene. Promising total olefin selectivities (for ethene + propene) of up to 65% were achieved at nearly 100% propane conversion. At high conversions, however, the proportion of propene obtained relative to ethene was small. A maximum propene selectivity of $\leq$ 30% was obtained at a propane conversion of ~ 65%.

One very promising feature of this system was that due to the high flow rates employed, drastic reductions in reactor size were possible. Unlike pyrolysis, the product distribution was found to be very selective towards ethene and propene. Furthermore, shorter residence times were required for comparable conversions, and catalyst coking was not observed. Interestingly, despite the high reaction temperature, Schmidt and co-workers[20,21] argued against a significant contribution from homogeneous reactions in their studies. They cited the reduction of bimolecular reaction steps as the primary reason for the higher selectivities observed. Since their reactive ends were bound to the surface, adsorbed alkyls could not easily react with gas molecules, allowing unimolecular reactions such as beta-hydrogen elimination to occur. In discussing their results, Schmidt and co-workers[20,21] did not address the possibility of heterogeneous-initiated, homogeneous reaction. Moreover, the extent to which oxygen was involved in combustion versus partial oxidation remained unknown. A potentially beneficial integration between combustion and oxidative dehydrogenation might be occurring, wherein H_2O generated early on from combustion might have prevented coking due to pyrolysis. Pt/Al_2O_3 and $Pt/Sn/Al_2O_3$ catalysts were known to demonstrate excellent activity and selectivity in non-oxidative propane dehydrogenation prior to coking.[22]

4.1.6 Objectives

Akin to OCM, several challenges exist for economically feasible catalytic conversion of propane to propene. Studies by Iglesia and co-workers,[5,6,23] Kung,[9] and others have confirmed the inherent difficulty in obtaining good yields in a reaction where the product bond energies were weaker than the reactant bond energies. While VO_x- and MoO_x-based catalysts have been shown to be the most active and selective catalysts thus far, it seems that the sites responsible for propane activation must also activate propene combustion pathways. Thus, an inherent yield maxima may exist that has yet to be determined. Meanwhile, based on the results of Chen *et*

al.[5,15] and Grabowski *et al.*,[16] it appeared that ODHP performance was primarily influenced by the energetics of propane hydrogen abstraction and propene adsorption. On supported materials, these values can be manipulated by changing the VO_x and MoO_x surface density and by impregnating alkali metals. As mentioned earlier, however, Kung[9] has argued that high densities of neighboring VO_x and MoO_x groups might result in decreased selectivity. Thus, in this chapter, we attempted to utilize nanocomposite supports to achieve a similar influence on the catalyst energetics without relying on high VO_x and MoO_x surface densities. ZrO_2 was selected as the support to modify since, out of all the supports examined thus far, the ZrO_2-supported vanadia catalysts have shown the highest oxidative dehydrogenation rates.[8] Moreover, as shown in Chapter 3, secondary metal cations could be doped into zirconia.[24] In this chapter, we have specifically focused on the potential of MoO_x-based, doped zirconia catalysts. Finally, based on previous work by Burch and Crabb,[18] ODHP carried out at conditions whereby only heterogeneous processes would occur could be unfeasible. Systems such as the one described by Nguyen and Kung,[2,19] whereby heterogeneously generated radicals initiated homogeneous reaction channels, have exhibited more promising results. We have previously shown that our $LiCl/MO_x$/doped SZ catalysts displayed ODHE activity at temperatures below 600°C.[24] These catalysts were investigated for ODHP in this chapter.

4.2 Experimental Studies

4.2.1 Sample Preparation

Doped zirconia was synthesized via the co-precipitation or sol-gel procedures outlined in Section 3.2.[24] Synthesis of the low-temperature MoO_x/doped ZrO_2 nanocomposite catalysts involved incipient wet-impregnation of molybdenum on the doped ZrO_2 nanocomposite support using $(NH_4)_6Mo_7O_{24}$ $4H_2O$ (STREM Chemical). For initial catalyst screening, MoO_x/M-doped ZrO_2 catalysts were impregnated with 2.5 wt% Mo. In later experiments focusing on MoO_x/Nb-doped ZrO_2, the surface density of MoO_x was calibrated via the procedure described in Section 3.3.2.[24] Following wet impregnation, samples were dried overnight at 120°C and then calcined under flowing air to 700°C to obtain the final catalyst.

Preparation of high-temperature $LiCl/MO_x$/doped SZ catalysts was accomplished by first sulfating the doped ZrO_2 nanocomposite support via wet impregnation, using a 0.5 M solution of ammonium sulfate. The resulting material was dried overnight at 120°C, followed by calcination

at 700°C for 3 hr. A second wet impregnation, co-impregnating an alkali salt ($LiCl{\cdot}H_2O$, NaCl, KCl or CsCl (Alfa Aesar, > 99.95%)) and a metal nitrate ($Nd(NO_3)_3{\cdot}6H_2O$, $Cr(NO_3)_3{\cdot}9H_2O$ or $Ni(NO_3)_2{\cdot}6H_2O$ (Alfa Aesar, > 99.9%)) was then performed. After impregnation, materials were dried overnight at 120°C, prior to calcination at 700°C for 3 hr to obtain the final catalyst.

4.2.2 Sample Characterization

Surface areas of calcined materials were calculated using a five-point Brunauer-Emmett-Teller method on a Micromeritics ASAP 2000. Phase identification was accomplished by X-ray diffraction (XRD) on a Siemens D5000 θ-θ diffractometer (45 kV, 40 mA, Cu Kα). Scherrer's formula was applied using the ZrO_2 (111) and (-111) diffraction peaks to determine the average crystallite size. Raman spectroscopy was performed on a Kaiser Hololab 5000R Raman Spectrometer equipped with a Coherent CW tunable laser operated at 514.5 nm. Resulting spectra were normalized with the sample laser exposure time (1–10 ms). X-ray photoelectron spectroscopy (XPS) data were collected with a Kratos AXIS Ultra Imaging X-ray Photoelectron Spectrometer using a Mono (Al) anode. To identify Mo species present on the catalyst surface, the Mo peak was analyzed across binding energies of 225–245 eV. Peaks were calibrated using the C 1s peak. 10 sweeps per sample for Mo and 20 sweeps per sample for C were performed to achieve adequate signal-to-noise.

Propene combustion kinetics were conducted by flowing 3% C_3H_6 and 3% O_2 at 80 mL/min over 50 mg of catalyst sieved for 80/120 mesh. The catalyst packed bed was diluted with 50 mg of SiO_2 to minimize contributions from hot spots and to quench the light-off of gas-phase homogeneous reactions. Propene conversions were obtained at 25°C intervals from 300°C to 400°C, holding for at least 2 hr at each temperature.

Water desorption kinetics were performed using a Perkin-Elmer TGA7. To minimize mass transfer limitations, the thermal gravimetric analysis (TGA) data were collected under 250 mL/min of flowing He (BOC Gases, Grade 5.0) using < 20 mg of catalyst held in a Pt sample pan. Helium was used to avoid introducing moisture to the sample. Samples were pretreated at 100°C for 2 hr to desorb physisorbed water, prior to ramping the temperature at 2°C/min to 200°C. The sample was then cooled to 100°C in flowing He and allowed to stabilize for 1 hr. A second ramp at 2°C/min to 200°C was then conducted to obtain a baseline for buoyancy

subtraction. The activation energy was determined with an expression derived by Coats and Redfern.[25]

4.2.3 Reactor Studies

Details regarding the basic reactor and product analysis setup were previously described in Section 3.2.3.[24] Initial catalyst screening of low-temperature MoO_x/M-doped ZrO_2 catalysts and high-temperature $LiCl/MO_x$/doped SZ catalysts was performed using 0.30 g of catalyst. The flowrate of reactants was held at 60 mL/min, using a 1:1 molar ratio of C_3H_8:O_2 in a dilute feedstream of 20% reactants. A N_2 flow of 5 mL/min was included as an internal standard. Low-temperature ODP performance was measured at 25°C intervals from 400°C to 500°C. High-temperature ODP performance was measured at 575°C and 600°C. In both cases, catalysts were held at each temperature of interest for a minimum of 2 hr to quantify potential catalyst deactivation and to provide a sufficient number of duplicates for statistical analysis. In several cases, to account for the inverse relationship between conversion and selectivity, reactor data were supplemented with additional measurements at various space velocities. Trials involved either 0.3 g or 0.5 g of catalyst and were performed at 425°C and 575°C/600°C for MoO_x/M-doped ZrO_2 and $LiCl/MO_x$/M-doped SZ catalysts, respectively. Volumetric flowrates between 30 and 120 mL/min were employed, encompassing space velocities between ~ 3,600 and 24,000 hr^{-1}.

4.2.4 Modeling Studies

The data for gas-phase kinetic and thermodynamic properties used in simulations were based on a mechanism by Marinov *et al.*[26] Originally developed for propane combustion, this homogeneous model contained over 90 species with ~ 550 reactions. The Marinov *et al.* mechanism was selected over a mechanism compiled by Mims *et al.*[27] (used in our earlier oxidative coupling of methane (OCM) simulations[28]) because of its emphasis on propane reactions and its more up-to-date rate parameters. In Figure 4.1, we compare the selectivity-conversion trajectories of the two different gas-phase mechanisms at T = 600°C using an identical surface mechanism ($|\Delta H_{ads}|$ = 250 kJ/mol, ΔH_{abs} = 125 kJ/mol).

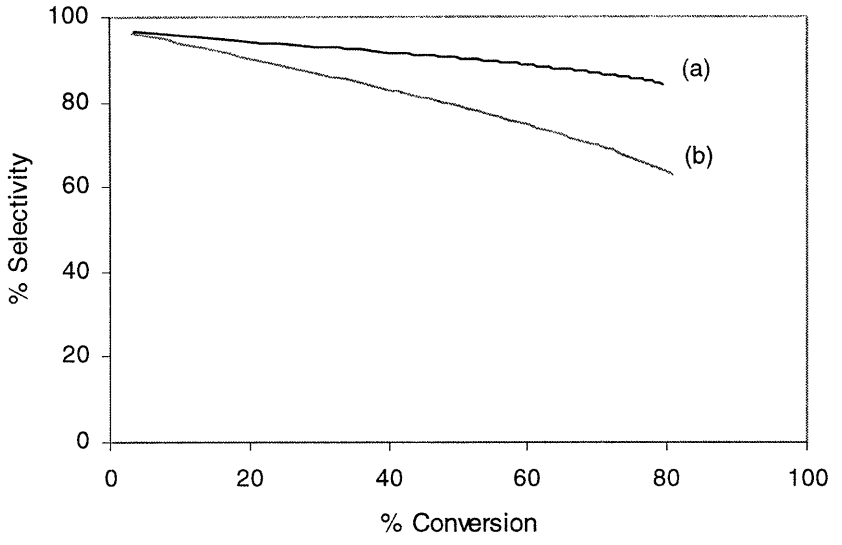

Figure 4.1. Influence of the (a) Marinov *et al.*[26] and (b) Mims *et al.*[27] gas-phase mechanisms on ODHP selectivity-conversion trajectories. Modeling conditions: $|\Delta H_{ads}|$ = 250 kJ/mol, ΔH_{abs} = 125 kJ/mol, C_3H_8:O_2:Ar feed ratio = 0.1:0.1:0.8, P = 1 atm, T = 600°C. The lower selectivity-conversion trajectory for the Mims *et al.* mechanism indicates that certain important gas-phase reactions are missing in the Marinov *et al.* mechanism.

As shown in Figure 4.1, it appears that several important degradation reactions are missing from the Marinov *et al.* mechanism. To isolate these critical gas-phase reactions, C_3H_6 sensitivity and rate-of-production analyses were performed using AURORA™. Specifically, PLUG™ concentration values at X_{C3H8} = 0.5 were input into the AURORA™ CSTR module and run at short residence times ($\tau \sim 1$ ms) to obtain a snapshot of the catalytic activity. The Mims *et al.* kinetic library[27] was found to contain a more expansive treatment of allene and propyne, two important product intermediates. Moreover, the C_3H_6 rate-of-production analysis on the Mims *et al.* mechanism PLUG™ output highlighted the importance of HO_2 reactions as degradation channels for propene. These reactions are largely ignored by the Marinov *et al.* mechanism.[26] Thus, reactions for allene, propyne and HO_2 were incorporated in the Marinov *et al.* mechanism using the Mims *et al.* kinetic library as a source. A complete list of the reactions added is included in Appendix 4-A.

The surface kinetics involved in ODHP were considered to follow a Mars-van Krevelen mechanism.[5,8,9,29] The reactions are as follows:

$$O_2 + 2V^* \leftrightarrow O^* + O^* \quad (1)$$

$$C_3H_8 + O^* \leftrightarrow C_3H_8O^* \quad (2)$$

$$C_3H_8O^* + O^* \leftrightarrow C_3H_7O^* + OH^* \quad (3)$$

$$C_3H_7O^* + O^* \leftrightarrow C_3H_6O^* + OH^* \quad (4)$$

$$C_3H_6O^* \leftrightarrow C_3H_6 + O^* \quad (5)$$

$$2OH^* \leftrightarrow H_2O + O^* + V^* \quad (6)$$

In the elementary mechanism proposed above, O* designates a lattice oxygen, V* represents a surface vacancy, and the remaining "*" compounds are indicative of surface adsorbed species. Reaction (1) describes the formation of active oxygen species from the dissociative adsorption of gas-phase oxygen. Upon propane adsorption on this surface (reaction (2)), hydrogen abstraction occurs via a neighboring oxygen atom (reaction (3)). A second hydrogen abstraction (reaction (4)) follows, resulting in the formation of $C_3H_6O^*$, which then desorbs as propene from the surface in reaction (5). In addition, each hydrogen abstraction step results in the formation of a surface hydroxyl group, which may combine via reaction (6) to form water, O* and a surface vacancy. The catalytic cycle is completed when the surface vacancies are regenerated to O* via reaction (1).

In addition to the main catalytic cycle described by reactions (1)-(6), several reactions were included to account for the products observed in our experimental studies. In reactor runs at 425°C, CO, CO_2 and C_3H_6 were identified as the major products. Moreover, although ethene was observed at longer residence times and higher temperatures, ethane was never observed. Thus, ethene formation must occur directly, without undergoing ODHE. In addition, the fact that ethene formation did not occur initially alongside CO, CO_2 and C_3H_6, but instead required longer residence times, suggested that its source was propene rather than propane. Furthermore, it is important to note that without specific surface-mediated reaction channels, simulated product distributions would not have sufficient quantities of ethene. Methane was also occasionally observed, although not in conjunction with ethene formation. At 425°C, methane formation occurred only in cases where propane combustion achieved light-off. Therefore, the reactions involved in methane and ethene formation did not appear to be similar.

In considering possible reaction channels leading to CO, CO_2, ethene and methane formation, we focused on the role of subsequent reactions. As was the case with OCM, such reactions are likely unavoidable even under the most idealized circumstances. Since we expected methane and ethene to be largely unreactive at ODHP reaction temperatures, we focused on possible reactions involving propene. Similar to propane, we assumed that once

adsorbed, propene could undergo hydrogen abstraction (reaction (7)). The result is a surface allyl species that was postulated to undergo one of three reactions. Surface allyl groups could either desorb (reaction (8)), undergo further hydrogen abstraction to form C_3H_4 (reaction (9)), or undergo a C-C bond cleavage to form formaldehyde and a vinyl radical (reaction (10)). Reaction (10) was included as a probable route for surface-mediated ethene formation. Methane formation was assumed to arise from gas-phase mediated reaction channels.

$$C_3H_6O^* + O^* \leftrightarrow C_3H_5O^* + OH^* \quad (7)$$

$$C_3H_5O^* \leftrightarrow C_3H_5 + O^* \quad (8)$$

$$C_3H_5O^* + O^* \leftrightarrow C_3H_4 + OH^* + V^* \quad (9)$$

$$C_3H_5O^* \leftrightarrow V^* + CH_2O + C_2H_3 \quad (10)$$

In addition to consecutive product reaction, competitive surface reactions for propane combustion have also been observed. For instance, through pulse experiments on V/MgO, Zanthoff *et al.*[30] have discovered that gaseous oxygen has a limited residence time on the surface before inclusion into the catalyst lattice. Correlating the appearance of undissociated oxygen on the surface with changes in product distribution, they attributed increases in CO_2 formation to the buildup of molecular oxygen. Some successful attempts have been made to control/eliminate surface combustion reactions. For example, the selective poisoning of sites responsible for alkane combustion using SiO_x has been reported.[31] Since our ultimate goal was to obtain an upper bound on ODHP, we did not include in our mechanism competing surface reactions directly responsible for propane combustion.

Paralleling reaction (9), an Eley-Rideal-type reaction involving gas-phase allyl species was also included for the formation of allene (reaction (11)). As discussed in the next section, this reaction was determined to have important consequences for ODHP performance. In addition, to account for the possibility of heterogeneous-initiated, gas-phase reactions, surface isopropyl groups were allowed to desorb into the gas phase (reaction (12)).[2] Finally, as with OCM, surface radical quenching reactions for HO_2 were also included (reactions (13) and (14)).

$$C_3H_5 + O^* \leftrightarrow C_3H_4 + OH^* \quad (11)$$

$$C_3H_7O^* \leftrightarrow C_3H_7 + O^* \quad (12)$$

$$HO_2 + V^* \leftrightarrow O^* + OH \quad (13)$$

$$HO_2 + O^* \leftrightarrow OH^* + O_2 \quad (14)$$

The approach to determining an upper bound for ODHP was undertaken in a similar manner to OCM (see Chapter 2).[28] Arrhenius pre-exponential factors were calculated using either collision theory or transition state arguments. Similarly, no additional barriers to reaction were considered beyond those required by thermochemistry. In the case of endothermic reactions, the activation energy was set equal to the enthalpy of reaction, while exothermic steps were assumed to be barrierless. Unlike the OCM case study, however, the larger pool of surface species resulted in a larger number of independent parameters. Our efforts to reduce the dimensional search space are described in the following section.

To simulate flow through a packed bed, the bed was visualized as a series of parallel, non-interacting, isothermal cylinders. As per arguments in Chapter 2,[28] the site density was adjusted to ~ 1×10^{-7} mole/cm^2 to conserve the total number of active sites. For ODHP, temperatures ranging from 425 to 600°C were examined at a propane-to-oxygen molar feed ratio of 1:1. A dilute feedstream of 20% reactants in argon was employed. Concentration profiles output from PLUG™ simulations were used in calculating propane conversion and C_3 selectivities down the catalyst bed. Yield versus axial position was then calculated, and the maximum yield was selected.

4.3 Results and Discussion

4.3.1 Upper Bound on ODHP

Compared with OCM, the larger number of surface species in ODHP required us to make additional assumptions to make this study more tractable. Based on physical reasoning, several steps were fixed at experimentally determined values to reduce the dimensionality of the search space. Several of these fixed values were either found to be nearly constant across a broad range of materials or were reactions to which ODHP performance was relatively insensitive. For example, since propane contains only sigma bonds, the initial interaction of propane with the surface (reaction (2)) is essentially physisorption. The maximum heat of adsorption can be bounded by values obtained from zeolitic materials, whose small pore diameters allow for greater interaction with the propane molecule. Zhu *et al.*[32] have determined that propane adsorption occurring on silicalite-1 is ~ 41 kJ/mol. Meanwhile, Kämper *et al.*[33] have reported a propane adsorption enthalpy of ~ 33.3 kJ/mol on the (001) surface of V_2O_5. As expected for physisorption, the propane adsorption value seems relatively insensitive to the catalyst, therefore,

we have fixed it at 40 kJ/mol. Finally, in measuring the activation energy for water desorption across a variety of MoO_x/ZrO_2 catalysts (see Appendix 4-B for details), values were found to only vary over a small range. Thus, a barrier of ~ 50 kJ/mol was fixed for reaction (6).

Given the hypothesized importance of reaction (5), $C_3H_6O^* \leftrightarrow C_3H_6 + O^*$, in determining catalyst selectivity,[15,16,17] we examined the influence of this value on ODP performance. Yield trajectories (not shown) changed only slightly depending on this barrier. The lack of any significant effect suggests that reaction (5) is in equilibrium, and is not kinetically significant in propene combustion. Based on the experimental propene adsorption measurements on MoO_2 performed by Wu and Tysoe,[34] we initially fixed the propene desorption enthalpy at 61.5 kJ/mol. In later yield map calculations, however, we reduced the barrier for propene desorption to a lower limit of 40 kJ/mol, equivalent to the barrier for propane desorption. Given propene's π-orbital, it is highly unlikely that propene would be more weakly bound to the surface than propane.

Similar to OCM, the first major independent input was the enthalpy of reaction (1), ΔH_{ads}, which described the formation of active oxygen species. A range of oxygen adsorption enthalpies between -100 kJ/mol and -300 kJ/mol was examined; this encompassed the literature values obtained for oxygen adsorption on a wide variety of metal oxides.[35] Enthalpies within this range were examined at intervals of 50 kJ/mole. The second independently specified parameter, ΔH_{abs}, described the initial hydrogen abstraction step from the adsorbed $C_3H_8O^*$ molecule (reaction (3)). We explored enthalpy values for this step centered around experimental results for the ODHP barrier of VO_x/Al_2O_3 obtained by Argyle *et al.*,[23] which encompassed a range between 75 kJ/mol and 150 kJ/mol. ΔH_{abs} values were initially examined at intervals of 25 kJ/mol, with additional simulations performed to improve the yield map resolution where necessary.

Since reactions (2), (5) and (6) were set to the values mentioned earlier, once the two independent parameters, ΔH_{ads} and ΔH_{abs}, were set, the remaining values for the reaction mechanism were automatically specified. The overall thermodynamics of ODP was used to specify the thermochemistry for reaction (4), and it was assumed that there was no barrier to this exothermic reaction. The thermochemistry for the remaining surface abstraction steps, such as those involving surface propene and allyl (reactions (7) and (9)–(11), respectively), were scaled according to differences in the C-H bond energies of these species relative to propane. It was

initially assumed that there were no additional barriers beyond the endothermicity of these reactions; this led to an upper bound on conversion. In calculating the barriers for these reactions, CH_2O and C_3H_4 surface formation was assumed to be accompanied by an immediate, barrierless desorption. For more details regarding the calculation of surface reaction barriers, please refer to Appendix 4-C. One example set of surface parameter data is also shown in Table 4.1.

Simulations using the aforementioned descriptions of surface kinetics resulted in poor selectivities even at minimal conversions (see Figure 4.2(c) as an example). The abnormally low propene selectivities were traced to the fast reactions (9) and (11), which converted allyl radicals to allene. (The oxidative chemistry of allene is not well understood, and both the Marinov *et al.* and the Mims *et al.* models are missing reaction pathways for allene. Here, it was assumed that allene was rapidly and essentially irreversibly consumed under our reaction conditions, and a global reaction of allene + O_2 → products was added to force this behavior in the model.) In initial simulations, the barrier for reaction (11) was set to 0 kJ/mol, since the reaction was calculated to be mildly exothermic. To obtain a refined estimate of the possible barrier for this

Table 4.1. Proposed surface mechanism for ODHP[†]

	Reaction	A_f[‡]	E_f (kJ/mol)	A_r	E_r (kJ/mol)
(1)	$O_2 + 2V^* \leftrightarrow O^* + O^*$	3.40E+18	0.0	2.39E+18	250.0
(2)	$C_3H_8 + O^* \leftrightarrow C_3H_8O^*$	1.45E+11	0.0	1.46E+13	40.0
(3)	$C_3H_8O^* + O^* \leftrightarrow C_3H_7O^* + OH^*$	1.23E+19	125.0	1.21E+18	0.0
(4)	$C_3H_7O^* + O^* \leftrightarrow C_3H_6O^* + OH^*$	1.23E+18	0.0	1.26E+19	165.8
(5)	$C_3H_6O^* \leftrightarrow C_3H_6 + O^*$	1.45E+11	0.0	1.46E+13	40.0
(6)	$2OH^* \leftrightarrow H_2O + O^* + V^*$	2.25E+18	50.0	4.53E+18	0.0
(7)	$C_3H_6O^* + O^* \leftrightarrow C_3H_5O^* + OH^*$	1.26E+19	79.5	1.23E+18	0.0
(8)	$C_3H_5O^* \leftrightarrow C_3H_5 + O^*$	1.46E+13	70.3	1.50E+11	0.0
(9)	$C_3H_5O^* + O^* \rightarrow C_3H_4 + O^* + OH^*$	1.27E+18	97.4		
(10)	$C_3H_5O^* \rightarrow V^* + CH_2O + C_2H_3$	1.46E+13	204.2		
(11)	$C_3H_5 + O^* \rightarrow C_3H_4 + OH^*$	1.50E+11	50.0		
(12)	$C_3H_7 + O^* \leftrightarrow C_3H_7O^*$	1.47E+11	9.7	1.46E+13	0.0
(13)	$HO_2 + O^* \leftrightarrow O_2 + OH^*$	1.67E+11	0.0	1.70E+11	44.8
(14)	$HO_2 + V^* \leftrightarrow O^* + OH$	1.67E+11	0.0	2.33E+11	90.5

[†] A-Factor and E_a values shown are for the case where ΔH_{ads} = -250.0 kJ/mol and ΔH_{abs} = 125 kJ/mol.
[‡] A-Factors in cm, mole, s units.

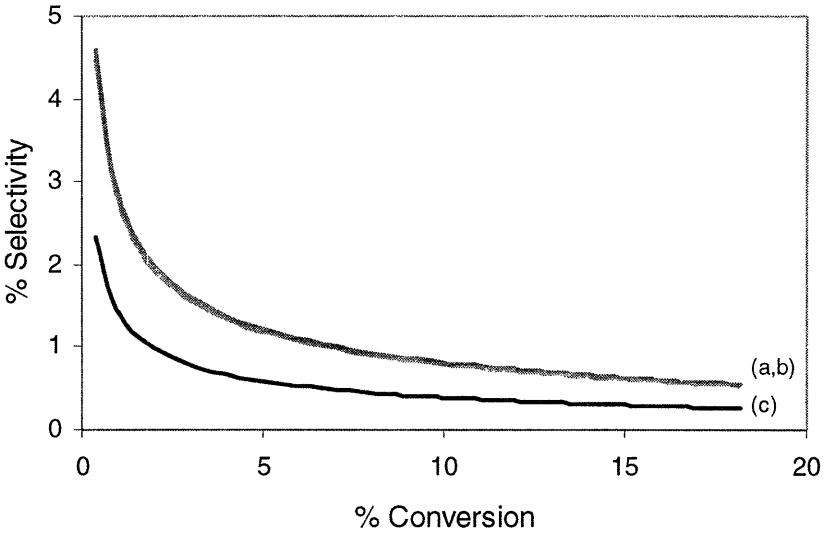

Figure 4.2. Influence of $C_3H_5 + O^* \leftrightarrow C_3H_4 + OH^*$ on ODP performance at a barrier height of (a) 50, (b) 25 and (c) 0 kJ/mol, assuming C_3H_4 is rapidly destroyed. Modeling conditions: $|\Delta H_{ads}| = 250$ kJ/mol, $\Delta H_{abs} = 125$ kJ/mol, $C_3H_8:O_2:Ar$ feed ratio = 0.1:0.1:0.8, P = 1 atm, T = 425°C.

reaction, we turned to the related gas-phase reactions. Depending on the assisting species, the barrier for tranforming allyl to allene can vary significantly. Unassisted, the beta scission of the allyl radical is very energetically expensive ($E_a \sim 260$ kJ/mol).[36] When reacting with a second radical species, however, no barrier to reaction is often reported.[37] Given the less reactive nature of surface O* with allyl radicals (compared to gas-phase radical + allyl reactions), we expected a small barrier would exist. Figure 4.2 shows the selectivity-conversion profiles for simulations performed using barrier heights ranging from 0 to 50 kJ/mol for reaction (11). In the original formulation (where $E_a = 0$ kJ/mol), the Eley-Rideal reaction (11) was a dominant reaction channel, resulting in selectivities of < 3% at conversions of < 20%. The addition of 25 kJ/mol barrier to this step, however, did not result in a dramatic improvement in selectivity. As the barrier for the Eley-Rideal step was increased, the surface reaction, $C_3H_5O^* + O^* \rightarrow C_3H_4 + OH^*$, became the rate-determining step for allyl degradation. Figure 4.3 shows the effect of increasing the barrier for reaction (9) by small increments beyond what was originally established via thermochemical arguments. By supplementing the barrier for this reaction by even 25 kJ/mol, dramatic enhancements in propene selectivity were observed.

Because of the sensitivity of ODP performance to both Eley-Rideal and Mars-van Krevelen channels for allyl degradation (reactions (11) and (9), respectively), to calculate an

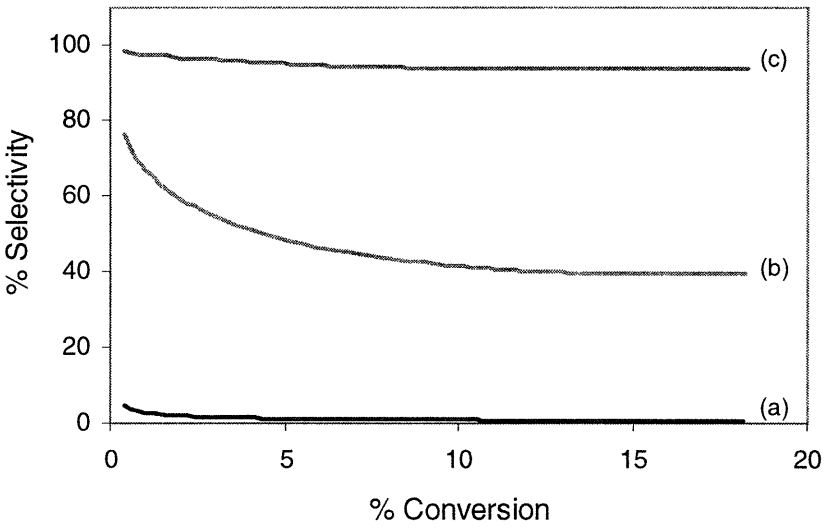

Figure 4.3. Influence of $C_3H_5O^* + O^* \rightarrow C_3H_4 + OH^* + O^*$ on ODP performance at a barrier height of (a) 68.85, (b) 93.85 and (c) 118.85 kJ/mol, assuming C_3H_4 is rapidly destroyed. Modeling conditions: $|\Delta H_{ads}|$ = 250 kJ/mol, ΔH_{abs} = 125 kJ/mol, C_3H_8:O_2:Ar feed ratio = 0.1:0.1:0.8, P = 1 atm, T = 425°C. High yields are possible if the barriers to hydrogen abstraction from chemisorbed allyl and physisorbed propane are comparable.

upper bound on ODP performance, we estimated the maximum possible increases in barrier height for these two (exothermic or slightly endothermic) reaction steps that were physically plausible. This corresponded to an increase of ~ 50 kJ/mol in E_a for both reactions. One caveat to this increase, however, was that the final barrier for either allyl reaction was not allowed to exceed the barrier for reaction (3), the initial hydrogen abstraction from propane. This was to ensure physical consistency, as propane is much less reactive than allyl. In cases where the 50 kJ/mol increase discussed above did lead to a barrier exceeding that of reaction (3), the barrier was simply set equal to the barrier for reaction (3). With these modifications, the maximum yields of the aforementioned subspace of $|\Delta H_{ads}|$ and ΔH_{abs} energies were tabulated in yield maps such as Figures 4.4 and 4.5 for reactions at 425°C and 600°C, respectively. As mentioned earlier, the propene desorption enthalpy was minimized to 40 kJ/mol, which was equivalent to the propane desorption enthalpy. Remaining surface energy values were left unchanged.

Initial results from simulations showed an unrealistic build-up in allene due to a lack of appropriate outlet combustion reactions in our mechanism. As a result, convoluting effects brought about by the equilibration of allene in reactions such as $2\ C_3H_5 \leftrightarrow C_3H_6 + C_3H_4$ resulted in selectivity-conversion trajectories not seen experimentally. An additional global reaction,

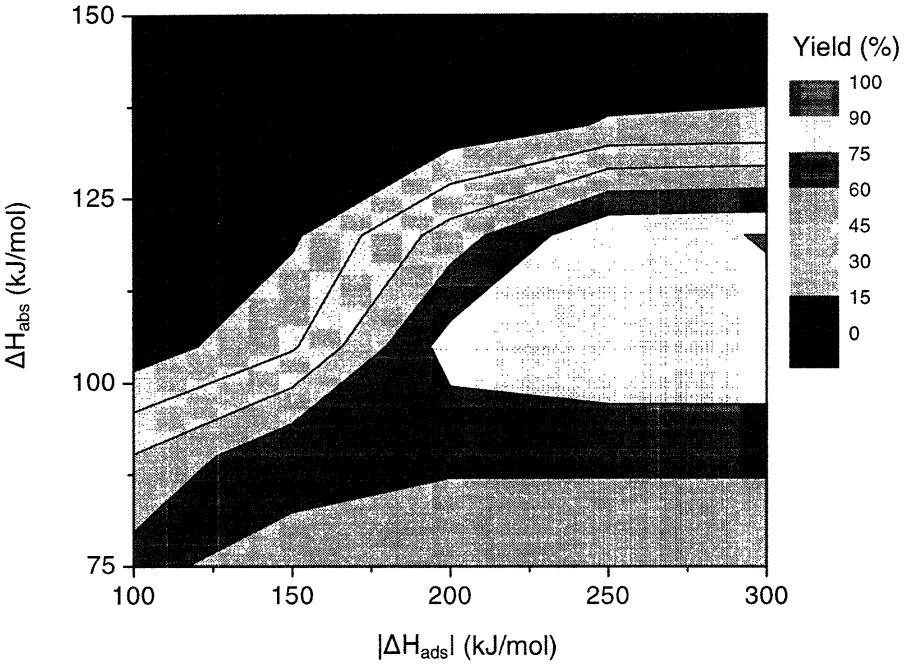

Figure 4.4. ODP yield bound at T = 425°C as determined by a plug flow approximation, as a function of the energetics of the major surface intermediates. The yield bound is quite sensitive to the activity of the catalyst (i.e., the enthalpy of reaction (3)), and moderately sensitive to the O_2 dissociative adsorption enthalpy (reaction (1)). As shown in Figures 4.2 and 4.3, the yield bound is also sensitive to the oxidation kinetics of the allyl radical. C_3H_8:O_2:Ar feed ratio = 0.1:0.1:0.8, P = 1 atm.

$C_3H_4 + O_2 \rightarrow CH_3CHO + CO$, was therefore inserted into the gas-phase mechanism with a rate constant of 1E+12 cm^3/mol·s to force combustion of allene. We believed that allene was even more reactive than propene, and so it would be consumed very rapidly, but certainly the process was much more complicated than the single-step reaction used here, and undoubtedly involves urface reactions.

As seen in Figures 4.4, yields in excess of 90% were predicted in some regions. Optimal catalyst performance was observed under conditions where the difference between the barriers for propane hydrogen abstraction and allyl reaction were minimized. In active ODP, allyl and propene were nearly in equilibrium. Thus, it is allyl loss, and hence the barriers heights for the surface reactions (9) and (11), that were critical to determining the yield obtained. In most cases, at a propane hydrogen abstraction value of 75 kJ/mol, the consistency constraint that propane must be less reactive than allyl significantly increased the allyl consumption rate; since allyl was essentially equilibrated with propene, this led to a significant reduction in yield. Thus, the yields

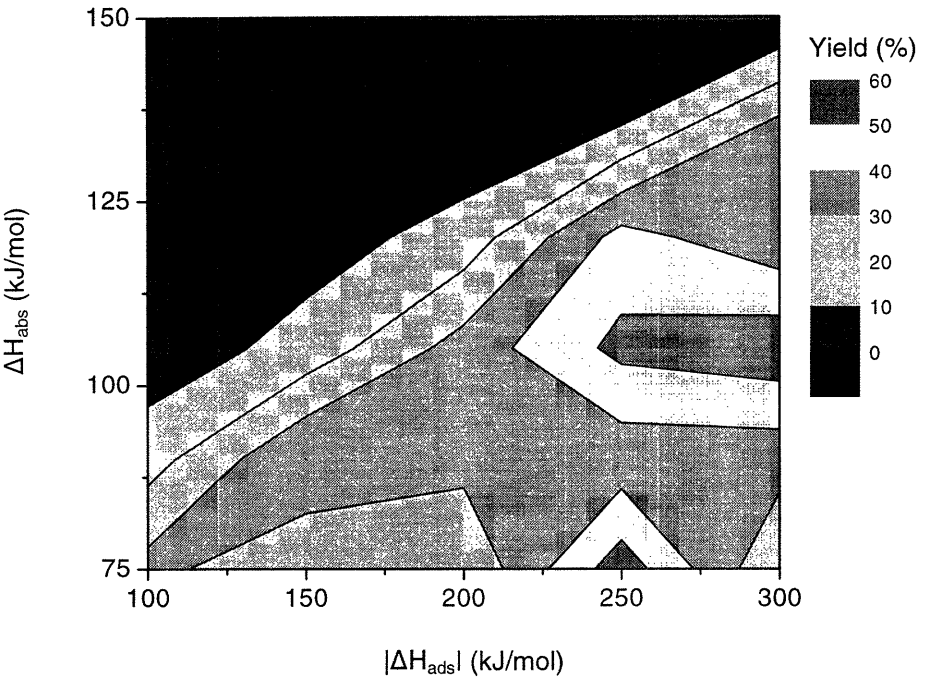

Figure 4.5. ODP yield bound at T = 600°C as determined by a plug flow approximation. The modeling conditions employed are otherwise identical to those used in generating Figure 4.4. C_3H_8:O_2:Ar feed ratio = 0.1:0.1:0.8, P = 1 atm.

bounds were highest at intermediate values of propane hydrogen abstraction. Catalysts with propane hydrogen abstraction barriers above 125 kJ/mol were found to be largely inactive for ODP. As expected, catalyst activity was significantly higher at 600°C than at 425°C, but the increased contribution of less selective gas-phase reactions reduced the attainable yields (maximum yield ~ 57%). Even under conditions where homogeneous reactions could be avoided, however, heterogeneous degradation of propene into CO_x must be considered. We have found propene selectivity to be very sensitive to the unknown barrier heights for the Eley-Rideal reaction $C_3H_5 + O^* \leftrightarrow C_3H_4 + OH^*$ and the corresponding Mars-van Krevelen reaction $C_3H_5O^* + O^* \leftrightarrow C_3H_4 + OH^* + O^*$. Additional barriers of > 25 kJ/mol beyond the estimated endothermicities for these reactions resulted in dramatic improvements in propene selectivity. The yield maps in Figures 4.4 and 4.5 suggested that very high yields might be possible for ODP if catalysts could be found that reacted slowly with allyl radical. An implicit assumption in our study was that allene was rapidly oxidized to CO_x under ODP conditions. This was not 100% certain due to incomplete understanding of allene combustion routes either on surfaces or in the gas phase. Our inability to set tight lower bounds on these undesirable reactions limited our ability to construct a tight upper bound on ODP yield. Regardless, these results showed that

there could be significant improvements in ODP performance to be gained by manipulating the catalyst surface energies.

4.3.2 MoO_x/Doped ZrO_2 Nanocomposite Catalysts

Figure 4.6 shows the ODHP screening results for various metal-doped zirconia nanocomposite catalysts (M/Zr = 0.05) impregnated with 2.5 wt% Mo. Depending on the catalyst surface area, Mo surface densities of 1-3 Mo/nm^2 were achieved. As mentioned earlier, while higher Mo surface densities were known to display superior conversions, our objective was to examine whether dopant addition could achieve enhanced ODHP activity without incurring the possible loss of selectivity accompanying highly clustered MoO_x moieties. A wide range of dopants was explored, sampling cations of alternative valence states and from different parts of the periodic table.

Similar to our studies with sulfated zirconia nanocomposites,[24] dopants were found to alter the resulting catalyst surface area. This effect was particularly pronounced at low surface coverages of MoO_x. As a consequence, depending on the particular dopant incorporated, the final MoO_x surface density varied between catalysts. As a control, a MoO_x/ZrO_2 catalyst with a higher surface density (3 Mo/nm^2) was selected for comparison. While the higher surface

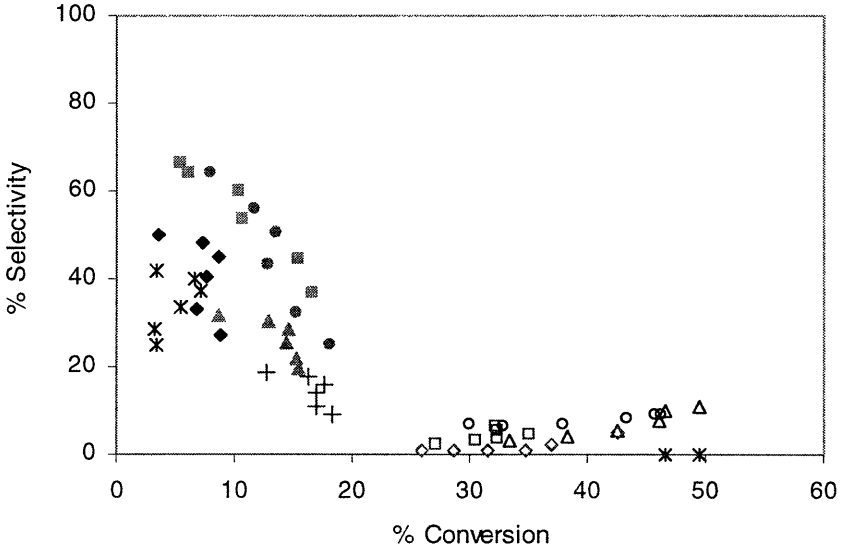

Figure 4.6. Selectivity versus conversion for MoO_x/M-doped ZrO_2 catalysts with M = (▪) no dopant, (•) Nb, (♦) Si, (▲) Ce, (*) Mg, (+) Ga, (o) Co, (Δ) Fe, (□) In and (◊) Sn. Catalyst composition: 2.5 wt% Mo, M/Zr = 0.05. C_3H_8:O_2:N_2/He = 0.1:0.1:0.8, 0.3 g catalyst, P = 1 atm, T = 425°C.

density favorably biased the control's results, our objective in catalyst screening was simply to identify a promising dopant candidate. As shown in Figure 4.6, with the exception of MoO_x/Nb-doped ZrO_2, all MoO_x/M-doped ZrO_2 catalysts exhibited lower propene selectivities than the control. The introduction of Nb to a VO_x/TiO_2 catalyst has been previously shown to improve ODHP performance.[38]

Having identified a potential candidate, more detailed studies were done on the MoO_x/Nb-doped ZrO_2 nanocomposite. Figure 4.7 shows the impact of MoO_x surface density on the performance of the Nb-doped material (Nb/Zr = 0.05). Mo surface densities were calibrated using the method described in Section 3.3.2.[24] As shown in Figure 4.7, larger MoO_x surface densities generally exhibited higher conversions. The optimal surface loading was determined to be 5 Mo/nm^2. The corresponding ODHP performance of MoO_x/ZrO_2 catalysts is shown in Figure 4.8. Compared to the Nb-doped catalysts, the undoped catalysts exhibited a much greater sensitivity to the MoO_x surface density. At surface densities higher than 5 Mo/nm^2, propane combustion appeared to be initiated. Similar to previously reported results,[15,39] the best ODHP performance was observed at intermediate MoO_x surface densities. Taking into consideration the influence of MoO_x surface density, we returned to the issue of whether the Nb dopant truly

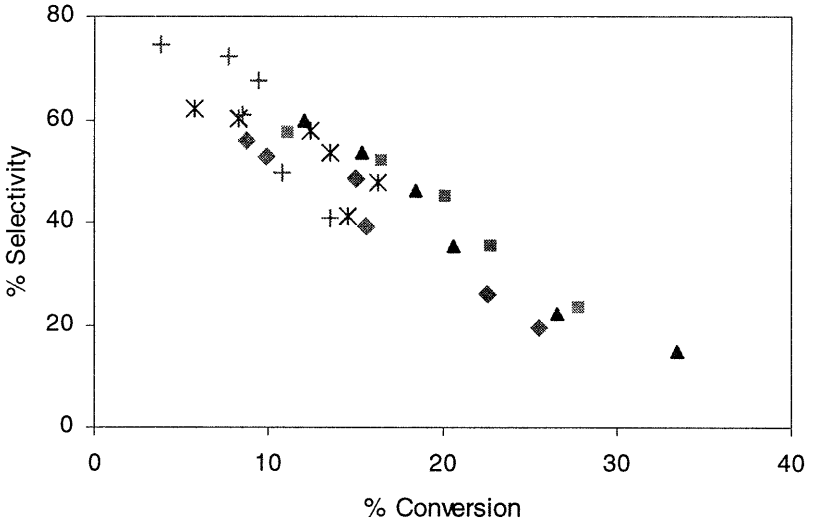

Figure 4.7. Selectivity versus conversion for MoO_x/Nb-doped ZrO_2 catalysts with (✳) 1 Mo/nm^2, (+) 2.5 Mo/nm^2, (■) 5 Mo/nm^2, (♦) 7 Mo/nm^2 and (▲) 10 Mo/nm^2. Catalyst composition: Nb/Zr = 0.05. C_3H_8:O_2:N_2/He = 0.1:0.1:0.8, 0.3 g catalyst, P = 1 atm, T = 425°C.

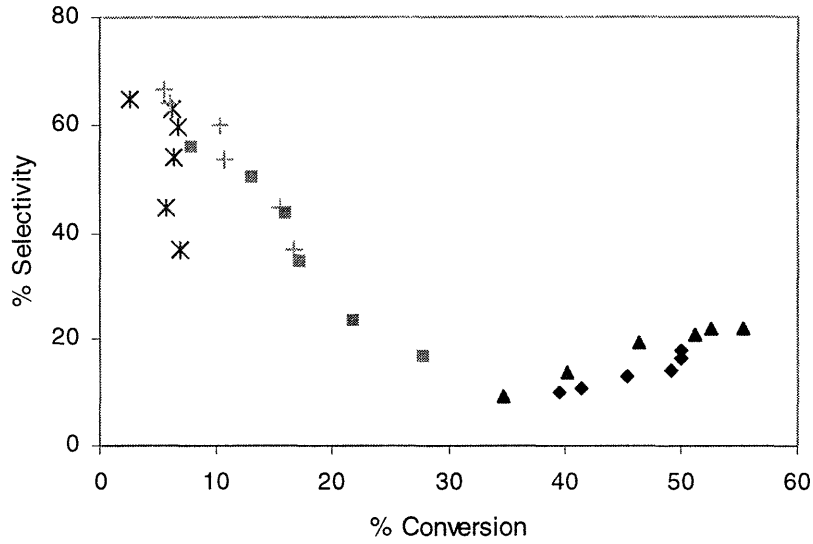

Figure 4.8. Selectivity versus conversion for MoO_x/ZrO_2 catalysts with (✳) 1 Mo/nm^2, (+) 3 Mo/nm^2, (■) 5 Mo/nm^2, (♦) 7 Mo/nm^2 and (▲) 10 Mo/nm^2. C_3H_8:O_2:N_2/He = 0.1:0.1:0.8, 0.3 g catalyst, P = 1 atm, T = 425°C.

enhanced ODHP performance. In Figure 4.9, we compared the performance of MoO_x/Nb-doped ZrO_2 catalysts with 5 Mo/nm^2 and various Nb/Zr doping ratios. At Nb/Zr = 0.01, the catalyst exhibited evidence of propane combustion light-off. Nb/Zr ratios of 0.05 and 0.10, however, displayed propene selectivities superior to the undoped material. At Nb/Zr = 0.15, however, the catalytic activity and selectivity began to tail off. Of the Nb/Zr ratios examined, Nb/Zr = 0.05 displayed the highest propene selectivity. As shown in Figure 4.10, we see a clear improvement in propene selectivity with the Nb-doped material. The maximum yields observed were 9.1% and 6.1% for MoO_x/Nb-doped ZrO_2 and MoO_x/ZrO_2, respectively. To determine the cause of this improved performance, kinetic experiments were conducted to isolate the relative rates of ODHP, propane combustion and secondary propene combustion. Independent propene combustion experiments showed that the Nb-doped material possessed a similar barrier height as the undoped material (103.0 ± 8.3 kJ/mol versus 106.8 ± 12.2 kJ/mol). The activation energy barrier for ODHP dehydrogenation was determined from initial selectivity values. By extrapolating propene selectivity to t = 0, we could remove the convoluting effect of secondary propene combustion. In order to accomplish this, the propene selectivity was measured as a function of space velocity for a small quantity of catalyst (0.05 g). This was repeated at each reaction temperature where a rate constant for ODHP was desired. Figure 4.11 shows that

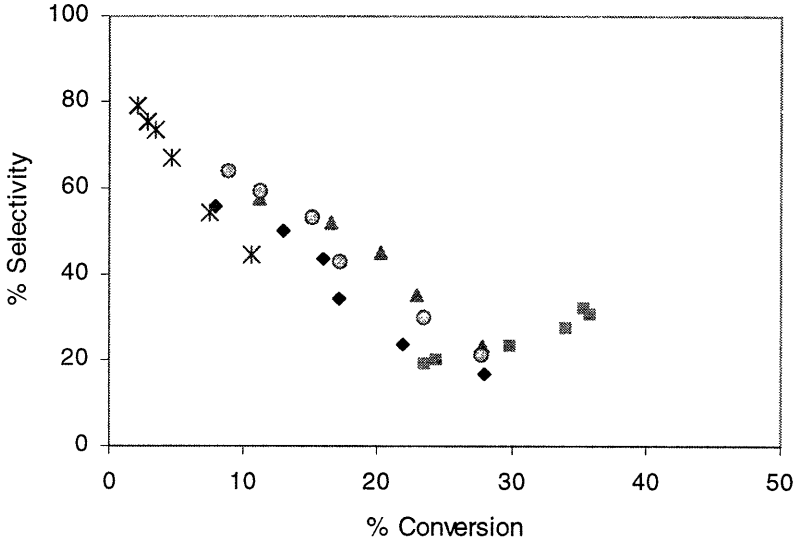

Figure 4.9. Selectivity versus conversion for MoO_x/Nb-doped ZrO_2 catalysts with Nb/Zr = (♦) 0.00, (■) 0.01, (▲) 0.05, (●) 0.10 and (✳) 0.15. Catalyst composition: 5 Mo/nm^2. C_3H_8:O_2:N_2/He = 0.1:0.1:0.8, 0.3 g catalyst, P = 1 atm, T = 425°C.

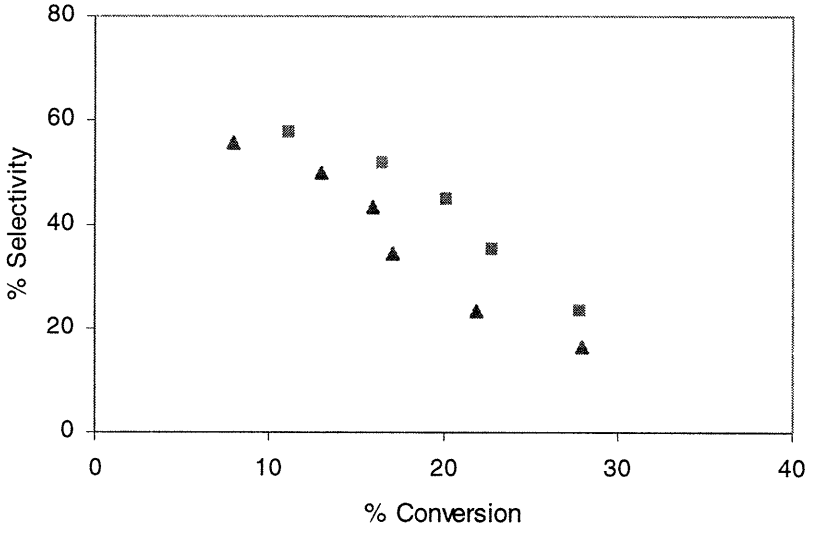

Figure 4.10. Selectivity versus conversion for (■) MoO_x/Nb-doped ZrO_2 (Nb/Zr = 0.05) and (▲) MoO_x/ZrO_2 catalysts. Catalyst composition: 5 Mo/nm^2. C_3H_8:O_2:N_2/He = 0.1:0.1:0.8, 0.3 g catalyst, P = 1 atm, T = 425°C.

propene selectivities rose and then reached a plateau as residence times were decreased. Once the initial propene selectivity was determined, the proportion of propane consumption leading to propene formation could be calculated. After measuring values across a range of temperatures, the activation energy barrier for ODHP could be determined. Chen *et al.*[39] have previously reported a value of 117 kJ/mol for 11 wt% MoO_x/ZrO_2 (~ 3.5 Mo/nm^2). While this MoO_x

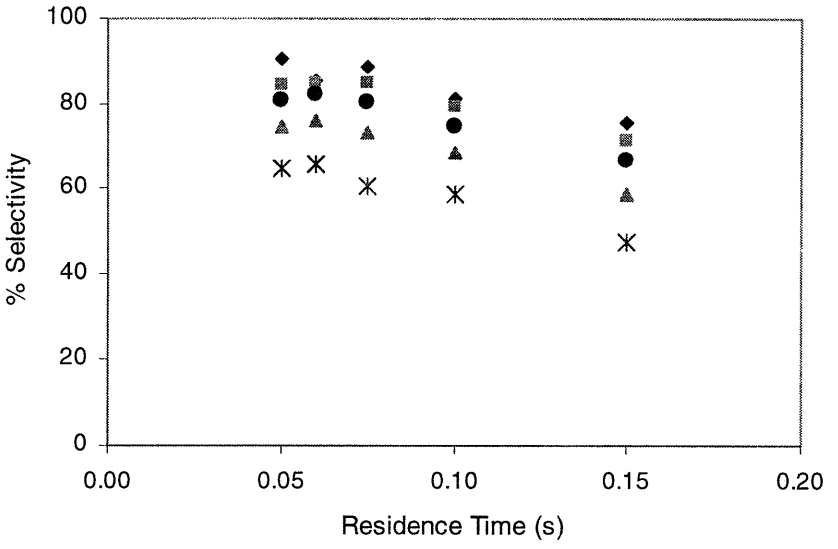

Figure 4.11. Propene selectivity versus residence time for MoO_x/Nb-doped ZrO_2 at (♦) 400°C, (■) 425°C, (●) 450°C, (▲) 475°C and (✳) 500°C. Catalyst composition: 5 Mo/nm^2, Nb/Zr = 0.05. C_3H_8:O_2:N_2/He = 0.1:0.1:0.8, 0.05 g catalyst diluted with 0.05 g SiO_2, P = 1 atm.

surface density was slightly lower than our control catalyst, related work done by Argyle *et al.*[23] on VO_x/Al_2O_3 showed that the apparent ODHP activation energy was relatively insensitive to surface density. In contrast to Chen *et al.*'s reported value,[39] the activation energy for our MoO_x/Nb-doped ZrO_2 catalyst was determined to be 94.7 ± 7.0 kJ/mol. Thus, the incorporation of Nb dopants in the ZrO_2-based catalyst resulted in a decrease in the ODHP activation energy without a corresponding decrease in the barrier for combustion.

Upon removing the convoluting effect of MoO_x surface density, we have shown that doping MoO_x/ZrO_2 with Nb resulted in improved ODHP performance. Furthermore, by isolating the surface kinetics of propane dehydrogenation from propane and propene combustion, we have found that the Nb dopant achieved this improvement by altering the surface chemistry. As hoped, the barrier for ODHP was significantly reduced without resorting to higher surface coverages of MoO_x. An ODHP yield of 9.1% was attained with the optimal MoO_x/Nb-doped ZrO_2 catalyst (Nb/Zr = 0.05, 5 Mo/nm^2) versus 6.1% from the corresponding MoO_x/ZrO_2 catalyst. Despite the enhancement in ODHP performance, however, this still fell short of the performance of the best ODHP catalysts reported in the literature. Ultimately, while our earlier simulations indicated that the highest possible propene selectivities were attainable at low temperatures where only heterogeneous processes were active, we were unable to obtain

selectivity-conversion profiles comparable to those seen in either short contact time or the homogeneous/heterogeneous-coupled system.

4.3.3 Lithium-based Catalysts

Given the enhanced low-temperature activity of $LiCl/MO_x$/doped SZ catalysts for ODHE, these nanocomposites were also examined for high-temperature ODHP. Of the various $LiCl/Nd_2O_3$/doped SZ catalysts listed in Table 3.2,[24] superior ODHP performance was obtained with In doping (20.4% propene yield) (see Figure 4.12). Subsequent efforts were devoted to the optimization of the In-doped SZ nanocomposites. Figure 4.13 shows the impact of various alkali promoters on the ODHP performance of Nd_2O_3/In-doped SZ (In/Zr = 0.05) catalysts. The LiCl-promoted material displayed the highest activity (> 46%), while maintaining a propene selectivity of > 43% and a total alkene selectivity of ~ 72.5%. Figure 4.14 shows the effect of impregnated metal oxides. NiO[4] and Cr_2O_3[40] were selected as possible alternatives to Nd_2O_3 due to previous reports of their superior ODHP performance. However, Cr_2O_3 was found to promote propane combustion, while NiO impregnation resulted in ODHP performance inferior to Nd_2O_3.

The effect of In loading on catalytic performance was examined in Figure 4.15. While an intermediate In loading (In/Zr = 0.05) exhibited the best propene selectivity, the $LiCl/Nd_2O_3$/In-

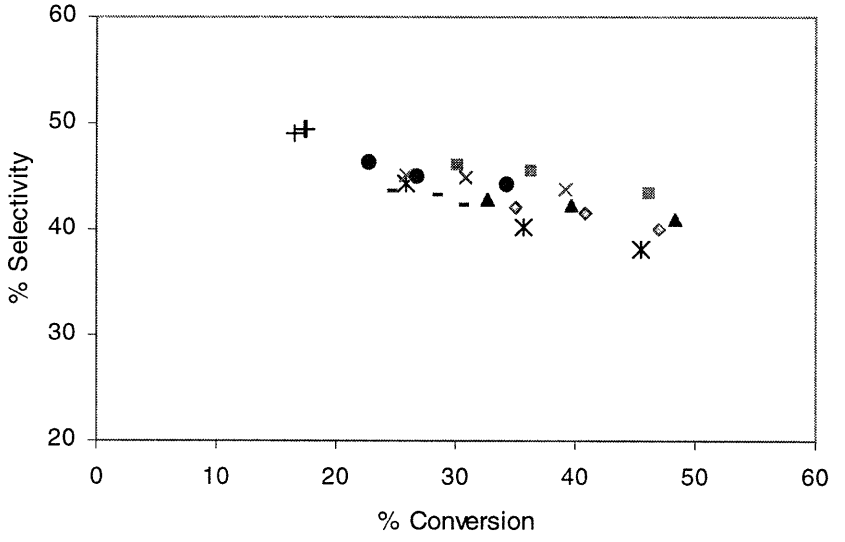

Figure 4.12. Selectivity versus conversion for $LiCl/Nd_2O_3$/M-doped SZ with M = (•) no dopant, (■) In, (▲) Al, (♦) Ga, (Ж) Sn, (×) Nb, (–) Ta and (+) Si. Catalyst composition: 5 wt% Li, 5 wt% Nd_2O_3, M/Zr = 0.05. C_3H_8:O_2:N_2/He = 0.1:0.1:0.8, 0.3 g catalyst, P = 1 atm, T = 600°C.

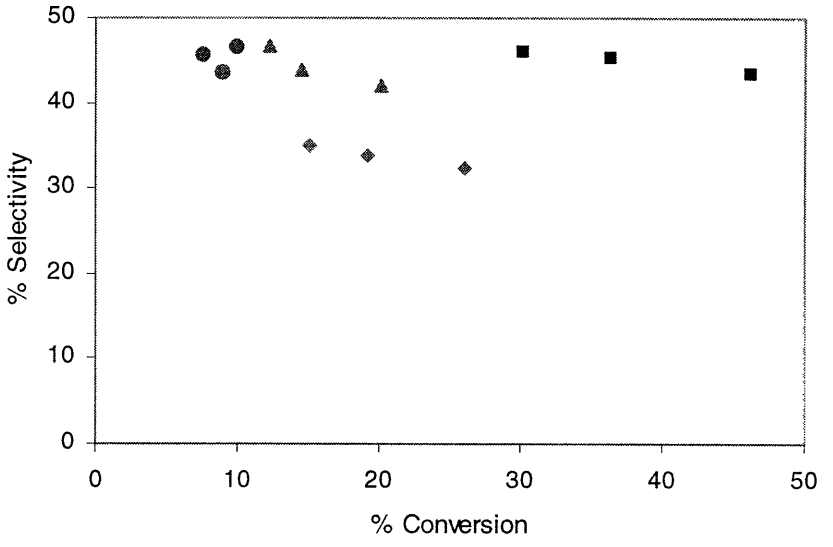

Figure 4.13. Selectivity versus conversion for Nd_2O_3/In-doped SZ impregnated with (■) LiCl, (◆) NaCl, (▲) KCl and (●) CsCl. Catalyst composition: 5 wt% alkali, 5 wt% Nd_2O_3, In/Zr = 0.05. C_3H_8:O_2:N_2/He = 0.1:0.1:0.8, 0.3 g catalyst, P = 1 atm, T = 600°C.

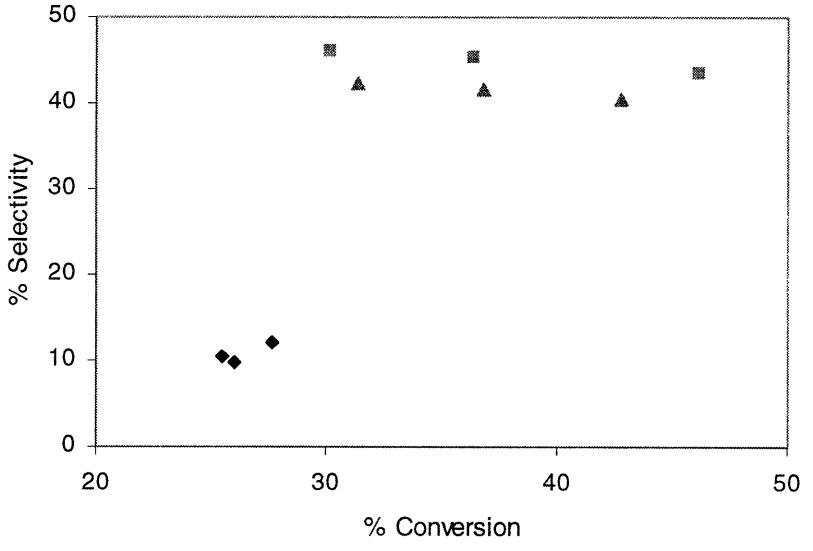

Figure 4.14. Selectivity versus conversion for LiCl/In-doped SZ impregnated with 5 wt% (■) Nd_2O_3, (▲) NiO and (♦) Cr_2O_3. Catalyst composition: 5 wt% Li, In/Zr = 0.05. C_3H_8:O_2:N_2/He = 0.1:0.1:0.8, 0.3 g catalyst, P = 1 atm, T = 600°C.

doped SZ catalysts with In/Zr = 0.01 and In/Zr = 0.10 displayed superior activity. Propene yields were maximized (22.3%) over LiCl/Nd_2O_3/In-doped SZ (In/Zr = 0.10). Figure 4.16 shows

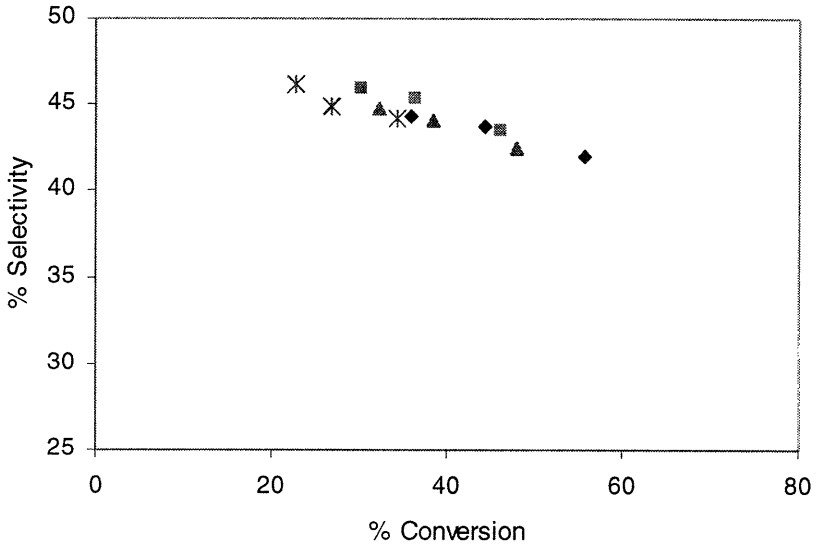

Figure 4.15. Selectivity versus conversion for $LiCl/Nd_2O_3$/In-doped SZ with In/Zr = (✳) 0.00, (▲) 0.01, (■) 0.05 and (♦) 0.10. Catalyst composition: 5 wt% Li, 5 wt% Nd_2O_3. C_3H_8:O_2:N_2/He = 0.1:0.1:0.8, 0.3 g catalyst, P = 1 atm, T = 600°C.

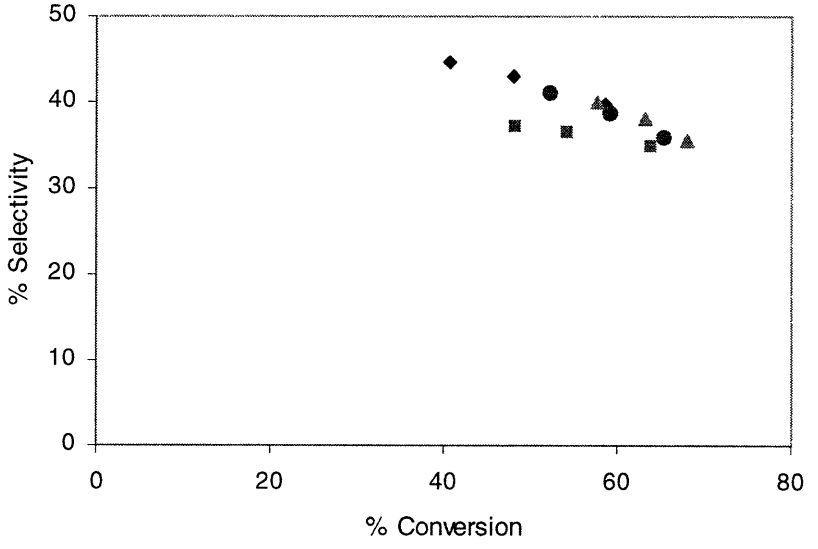

Figure 4.16. Selectivity versus conversion for LiCl/In-doped SZ impregnated with (♦) 0, (●) 1, (▲) 5 and (■) 10 wt% Nd_2O_3. Catalyst composition: 5 wt% Li, In/Zr = 0.10. C_3H_8:O_2:N_2/He = 0.1:0.1:0.8, 0.5 g catalyst, P = 1 atm, T = 600°C.

the impact of Nd_2O_3 loading on the $LiCl/Nd_2O_3$/In-doped SZ (In/Zr = 0.10) catalyst.[i] Loadings of < 10 wt% Nd_2O_3 appeared to follow the same selectivity-conversion trajectory, with larger

[i] Please note that in Figure 4.16, a larger quantity of catalyst (0.5 g) was employed.

Nd_2O_3 loadings achieving higher conversions. At 10 wt% Nd_2O_3, however, the ODHP activities decreased, which could be due to the exposure of Nd_2O_3. A maximum yield of 24.3% was observed using a $LiCl/Nd_2O_3$/In-doped SZ catalyst (5 wt% Nd_2O_3, In/Zr = 0.10). This is significantly higher than the 18% propene yield obtained by Burch and Crabb[18] for the optimized homogeneous ODHP.

4.4 Summary

In this chapter, both the experimental and modeling techniques developed in Chapter 2[28] and Chapter 3[24] were employed towards ODHP. Similar to our motivation for OCM, the previous lack of success in catalyst development prompted if there existed an inherent limit to propene yield. Furthermore, there is still debate as to whether heterogeneous reaction or heterogeneous-initiated, homogeneous reaction is preferable. The larger number of parameters in ODHP required a greater degree of experimental inputs. Simulation results showed that for near-ideal catalysts, the selectivity in ODHP was controlled by the competition between the rate-limiting attack on propane, and the undesirable consumption of allyl radicals, which was likely the rate-limiting step in propene combustion (on catalysts active for ODHP). Our inability to tightly bound the rates of the reactions that consumed allyl radicals (and the later steps in this reaction sequence) limited our ability to set a tight upper bound on the ODP yield.

Alongside our modeling efforts, we have also explored the possibility of employing zirconia-based nanocomposites for ODHP. Through the introduction of dopants, we endeavored to improve the low-temperature ODHP activity without having to rely on high MoO_x surface densities. Specifically, the introduction of a Nb dopant effectively enhanced the ODHP selectivity of MoO_x/ZrO_2, giving maximum propene yields of > 9% at 425°C. Based on kinetic studies, the improved performance of MoO_x/Nb-doped ZrO_2 was traced to a reduction in the difference in the activation energy barriers between ODHP and secondary propene combustion. Conversions of MoO_x/Nb-doped ZrO_2, however, remained lower than those achievable in short contact time or heterogeneous/homogeneous-coupled systems. Thus, catalysts operating at higher temperatures, where homogeneous reaction pathways might play a greater role, were examined in depth. In particular, $LiCl/MO_x$/doped SZ catalysts were tested, since these nanocomposites were found to display superior ODHE activity at lower temperatures.[24] In-doped SZ was found to be a promising support for ODHP, and Nd_2O_3 impregnation has led to

the optimal selectivity-conversion trajectory. The optimized LiCl/Nd_2O_3/In-doped SZ catalyst (5 wt% Li, 5 wt% Nd_2O_3, In/Zr = 0.10) achieved an excellent propene yield of 24.3% at 600°C.

4.5 References

[1] Chaar, M. A., Patel, D., and Kung, H. H., *J. Catal.* **109**, 463 (1988).

[2] Nguyen, K. T., and Kung, H. H., *J. Catal.* **122**, 415 (1990).

[3] Watson, R. B., and Ozkan, U. S., *J. Catal.* **191**, 12 (2000).

[4] Wang, S., Murata, K., Hayakawa, T., Hayakawa, S., and Suzuki, K., *Chem. Lett.*, 25 (1999).

[5] Chen, K., Xie, S., Bell, A. T., and Iglesia, E., *J. Catal.* **198,** 232 (2001).

[6] Khodakov, A., Olthof, B., Bell, A. T., and Iglesia, E., *J. Catal.* **181**, 205 (1999).

[7] Blasco, T., and Lopez-Nieto, J. M., *Appl. Catal. A: Gen.* **157**, 117 (1997).

[8] Khodakov, A., Olthof, B., Bell, A. T., and Iglesia, E., *J. Catal.* **177**, 343 (1998).

[9] Kung, H. H., *Adv. Catal.* **40**, 1 (1994).

[10] Bettahar, M. M., Costentin, G., Savary, L., and Lavalley, J. C., *Appl. Catal. A: Gen.* **145**, 1 (1996).

[11] Gao, X., Ruiz, P., Xin, Q., Guo, X., and Delmon, B., *J. Catal.* **148**, 56 (1994).

[12] Ueda, W., Lee, K. H., Yoon, Y.-S. and Moro-oka, Y., *Catal. Today* **44**, 199 (1998).

[13] Lee, K. H., Yoon, Y.-S., Ueda, W., and Moro-oka, Y., *Catal. Lett.* **46**, 267 (1997).

[14] Cadus, L. E., Gomez, M. F., and Abello, M. C., *Catal. Lett.* **43**, 229 (1997).

[15] Chen, K., Xie, S., Bell, A. T., and Iglesia, E., *J. Catal.* **195**, 244 (2000).

[16] Grabowski, R., Grzybowska, B., Samson, K., Sloczyński, J., Stoch, J., and Wcisło, K., *Appl. Catal. A: Gen.* **125**, 129 (1995).

[17] Martin, C., Rives, V., and Gonzalez-Elipe, A. R., *J. Catal.* **114**, 473 (1988).

[18] Burch, R., and Crabb, E. M., *Appl. Catal. A: Gen.* **100**, 111 (1993).

[19] Nguyen, K. T., and Kung, H. H., *Ind. Eng. Chem. Res.* **30**, 352 (1991).

[20] Huff, M., and Schmidt, L. D., *J. Catal.* **149**, 127 (1994).

[21] Huff, M., Torniainen, P. M., and Schmidt, L. D., *Catal. Today* **21**, 113 (1994).

[22] Barias, O. A., Holmen, A., and Blekkan, E. A., *J. Catal.* **158**, 1 (1996).

[23] Argyle, M. D., Chen, K., Bell, A. T., and Iglesia, E., *J. Catal.* **208**, 139 (2002).

[24] Su, Y. S., Green, W. H., Jr., and Ying, J. Y., to be submitted to *J. Catal.*

[25] Coats, A. W., and Redfern, J. P., *Nature* **201**, 68 (1964).

[26] Marinov, N. M., Pitz, W. J., Westbrook, C. K., Vincitore, A. M., Castaldi, M. J., Senkan, S. M., *Comb. Flame* **114**, 192 (1998).

[27] Mims, C. A., Mauti, R., Dean, A. M., and Rose, K. D., *J. Phys. Chem.* **98**, 13357 (1994).

[28] Su, Y. S., Ying, J. Y., and Green, W. H., Jr., *J. Catal.* **218**, 321 (2003).

[29] Chen, K., Khodakov, A., Yang, J., Bell, A. T., and Iglesia, E., *J. Catal.* **186**, 325 (1999).

[30] Zanthoff, H. W., Buchholz, S. A., Pantazidis, A., and Mirodatos, C., *Chem. Eng. Sci.* **54**, 4397 (1999).

[31] Zanthoff, H. W., Lahmer, M., Baerns, M., Klemm, E., Seitz, M., and Emig, G., *J. Catal.* **172**, 203 (1997).

[32] Zhu, W., Kaptejin, F., and Moulijn, J. A., *Phys. Chem. Chem. Phys.* **2**, 1989 (2000).

[33] Kämper, A., Auroux, A., and Baerns, M., *Phys. Chem. Chem. Phys.* **2**, 1069 (2000).

[34] Wu, G., Tysoe, W. T., *Surf. Sci.* **391**, 134 (1997).

[35] Arnaud, Y. P., *Appl. Surf. Sci.* **62**, 37 (1992).

[36] Davis, S. G., Law, C. K., Wang, H., *J. Phys. Chem. A* **103**, 5889 (1999).

[37] NIST Chemical Kinetics Database, *Standard Reference Database 7, Version 7.0 (Web Version)*, <http://kinetics.nist.gov/index.php?PHPSESSID=52df41086f34a1b9019c8d32d6bc35da> (10 November, 2003).

[38] Viparelli, P., Ciambelli, P., Lisi, L., Ruoppolo, G., Russo, G., and Volta, J. C., *Appl. Catal. A: Gen.* **184**, 291 (1999).

[39] Chen, K., Bell, A. T., Iglesia, E., *J. Phys. Chem. B* **104**, 1292 (2000).

[40] Grabowski, R., Grzybowska, B., Samson, K., Sloczyński, J., and Wcisło, K., *React. Kinet. Catal. Lett.* **57**, 127 (1996).

Appendix 4-A Supplemental Gas-Phase Kinetic Data[‡]

	A-Factor	n	E_a
Reactions Involving Allene:			
C*C*C + CH_3 ↔ C#CC. + CH_4	0.37E+00	0.0	7438.0
H + C*C*C ↔ C*CC.	5.66E+22	-3.026	7536.0
H + C*C*C ↔ CC*C.	6.38E+25	-4.047	14693.0
CH_3 + C_2H_2 ↔ C*C*C + H	7.32E+27	-4.395	38603.0
H + C#CC ↔ C*C*C + H	1.04E+20	-1.821	17854.0
C_2H_5 + C*CC. ↔ C*C*C + C_2H_6	2.40E+12	0.0	0.0
C*CC. + C*CC. ↔ C*CC + C*C*C	1.00E+12	0.0	0.0
C*CC. + CY13PD5. ↔ C*C*C + CY13PD	2.40E+12	0.0	0.0
Reactions Involving Propyne:			
CC.*C ↔ C#CC + H	1.84E+38	-5.155	48281.0
H + C#CC ↔ CC*C.	2.59E+34	-6.587	12401.0
H + C#CC ↔ C*CC.	3.23E+28	-4.487	16297.0
CH_3 + C#CC ↔ C*CC.C	7.09E+55	-12.504	46211.0
Reactions Involving HO_2:			
CCCOO. ↔ C*CC + HO_2	5.75E+71	-17.647	53511.0
CC.COOH ↔ C*CC + HO_2	1.39E+35	-7.184	20817.0
C_2COO. ↔ C*CC + HO_2	7.10E+61	-14.903	47943.0
C_2.COOH ↔ C*CC + HO_2	2.54E+40	-8.557	29152.0
Miscellaneous Reactions:[‡‡]			
CCC. + O_2 ↔ CCCOO.	1.34E+56	-13.370	17668.0
CCCOO. ↔ CCCHO + OH	4.76E+50	-11.805	52865.0
CC.COOH ↔ CCCOO.	4.71E+33	-7.296	20534.0
CCC. + O_2 ↔ CC.COOH	3.21E+55	-13.456	21915.0
CC.C + O_2 ↔ C_2COO.	2.66E+57	-13.764	17830.0
C_2COO. ↔ OH + C_2C*O	6.24E+56	-13.673	54187.0
C_2.COOH ↔ C_2COO.	1.10E+40	-8.761	26633.0
CC.C + O_2 ↔ C_2.COOH	8.22E+57	-13.870	25377.0
C_2.COOH ↔ CH_3 + C*COOH	5.93E+36	-7.337	40110.0
CCC. + O_2 ↔ CCCHO + OH	6.79E+20	-2.848	16506.0
CC.C + O_2 ↔ OH + C_2C*O	1.93E+18	-2.222	12720.0
CC.C + O_2 ↔ CH_3 + C*COOH	2.31E+28	-4.767	24554.0

*Source: Mims, C. A., Mauti, R., Dean, A. M., and Rose, K. D., J. Phys. Chem. **98**, 13357 (1994). Units [=] mol/cal/s.*

[‡] Nomenclature rules: "*" [=] double bond, "#" [=] triple bond. Hydrogen atoms are implied. Thus, "CCC" represents C_3H_8. The location of radicals in larger hydrocarbons is indicated by a "." next to the appropriate carbon atom. Example: "CCC." [=] n-propyl radical. For basic radicals, such as OH and CH_3, the existence of a radical species is understood. "C_2" indicates that the two carbon atoms branch off from the same atom, instead of being connected linearly. Example: "C_2C*O" [=] acetone. CY13PD represents cyclopentadiene and CY13PD5. represents cyclopentadiene radical.

[‡‡] Reactions were included to define outlet (degradation) channels for larger compounds never observed experimentally.

Appendix 4-B Calculation of Hydroxyl Recombination Activation Energy Barrier

Non-isothermal kinetic water desorption data collected via TGA, once corrected for buoyancy effects, were analyzed via the equation derived by Coats and Redfern:[25]

$$\log\left[\frac{1-(1-\alpha)^{1-n}}{(1-n)T^2}\right] = \log\left[\frac{ZR}{\beta E_a}\left(1-\frac{2RT}{E_a}\right)\right] - \frac{E_a}{2.303RT}$$

where α represents the degree of water desorption (from 0 to 1), n is the reaction order, T is the temperature, R is the universal gas constant, Z is the reaction pre-exponential factor, and β is the heating rate. Assuming water desorption follows reaction (6),

$$2OH^* \leftrightarrow H_2O + O^* + V^*$$

n was set equal to 2. By plotting

$$y = \log\left[\frac{1-(1-\alpha)^{1-n}}{(1-n)T^2}\right]$$

versus x = 1/T, the activation energy can be calculated by multiplying the slope by –2.303R. An example plot is shown below in Figure 4-B.1:

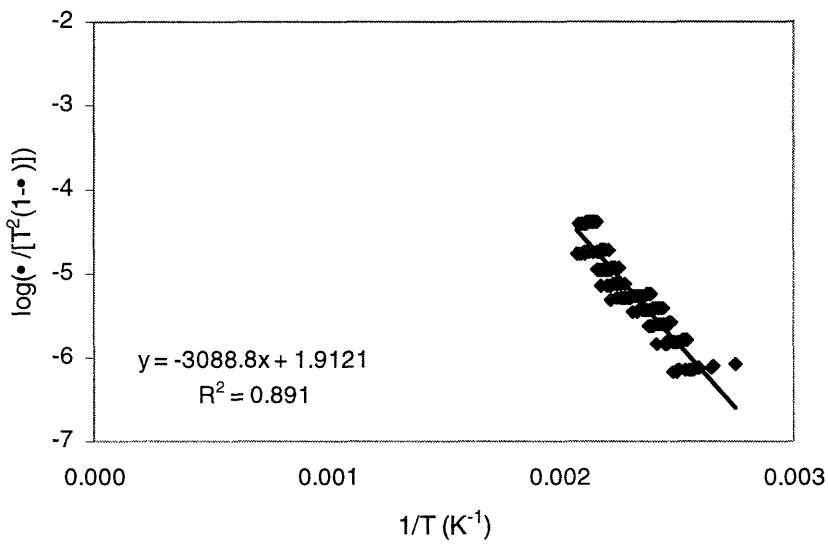

Figure 4-B.1. Activation energy barrier calculation (E_a ~ 59.1 kJ/mol) for water desorption on MoO_x/ZrO_2 catalyst with 10 Mo/nm^2. Reaction conditions are described in Section 4.2.2.

The activation barrier for reaction (6) was measured on MoO_x/ZrO_2 catalysts with various MoO_x surface densities (see Table 4-B.1). Also listed was the value obtained for the MoO_x/Nb-doped ZrO_2 catalyst with 5 Mo/nm^2.

Table 4-B.1. Activation energy barriers for water desorption over various MoO_x/ZrO_2 catalysts.

Catalyst	MoO_x Surface Density (Mo/nm^2)	Activation Energy (kJ/mol)
MoO_x/ZrO_2	1	69.1
MoO_x/ZrO_2	3	45.5
MoO_x/ZrO_2	5	48.5
MoO_x/ZrO_2	10	59.1
MoO_x/Nb-doped ZrO_2*	5	60.7

*Nb/Zr = 0.05.

Appendix 4-C Calculation of Surface Reaction Enthalpies for ODHP

The reactions involved in the main catalytic cycle for ODHP are:

(1)	$O_2 + 2V^* \leftrightarrow O^* + O^*$	ΔH_{ads}
(2)	$C_3H_8 + O^* \leftrightarrow C_3H_8O^*$	$\Delta H_{MO\text{-}C3H8}$
(3)	$C_3H_8O^* + O^* \leftrightarrow C_3H_7O^* + OH^*$	ΔH_{abs}
(4)	$C_3H_7O^* + O^* \leftrightarrow C_3H_6O^* + OH^*$	ΔH_{abs2}
(5)	$C_3H_6O^* \leftrightarrow C_3H_6 + O^*$	$-\Delta H_{MO\text{-}C3H6}$
(6)	$OH^* + OH^* \leftrightarrow H_2O + O^* + V^*$	ΔH_{recomb}

The overall reaction is given by:

$$C_3H_8 + \tfrac{1}{2}\, O_2 \leftrightarrow C_3H_6 + H_2O \qquad \Delta H_{overall}$$

$\Delta H_{overall}$ involves only gas-phase species with known heats of formation. As discussed in Section 4.3.1, to reduce the number of independent parameters, $\Delta H_{MO\text{-}C3H8}$, $\Delta H_{MO\text{-}C3H6}$ and ΔH_{recomb} were fixed at the experimentally determined values (-40 kJ/mol, -61.5 kJ/mol and 50 kJ/mol, respectively). Upon independently fixing reactions (1) and (3), the enthalpy for reaction (4) is determined by:

$$\Delta H_{abs2} = \Delta H_{overall} - \tfrac{1}{2}\,\Delta H_{ads} - \Delta H_{MO\text{-}C3H8} - \Delta H_{abs} - \Delta H_{recomb} + \Delta H_{MO\text{-}C3H6}$$

We can then employ these values to specify the bond strength of surface species, which are used to define enthalpies for the remaining surface reactions.

The formation of O* species on the surface is defined via reaction (1). This involves the dissociative adsorption of oxygen on the surface (ΔH_{ads}), the result of which is the formation of two active O* species.

$$\Delta H_{M\text{-}O} = (\Delta H_{ads} - BDE_{O2})/2$$

where BDE_{O2} is simply the bond dissociation energy of O_2 in the gas phase at the reaction temperature of interest. The energy associated with the transformation of O* to OH* ($\Delta H_{MO\text{-}H}$) can be defined by:

$$\Delta H_{MO\text{-}H} = \tfrac{1}{2}\,(\Delta H_{abs} + \Delta H_{abs2} - \Delta H_A - \Delta H_{MO\text{-}C3H6} - \Delta H_{MO\text{-}C3H8} - \Delta H_B)$$

where ΔH_A and ΔH_B are known enthalpies associated with the reactions,

$C_3H_7 \leftrightarrow C_3H_6 + H$	ΔH_A
$C_3H_8 \leftrightarrow C_3H_7 + H$	ΔH_B

Once $\Delta H_{MO\text{-}H}$ is defined, $\Delta H_{MO\text{-}C3H7}$ can be obtained as follows:

$$\Delta H_{MO\text{-}C3H7} = -\Delta H_{abs2} + \Delta H_A + \Delta H_{MO\text{-}C3H6} + \Delta H_{MO\text{-}H}$$

Furthermore, we can define $\Delta H_{M\text{-}OH}$ by

$$\Delta H_{M\text{-}OH} = -\Delta H_{MO\text{-}H} - \Delta H_{recomb} + \Delta H_C$$

where ΔH_C is associated with the reaction,

$$H + OH \leftrightarrow H_2O \qquad \Delta H_C$$

This allows the reactions involved in HO_2 radical quenching to be determined. These are:

$$HO_2 + V^* \leftrightarrow O^* + OH \qquad \Delta H_{13}$$

$$HO_2 + O^* \leftrightarrow O_2 + OH^* \qquad \Delta H_{14}$$

The corresponding reaction enthalpies are:

$$\Delta H_{13} = \Delta H_{M\text{-}O} + \Delta H_D$$

$$\Delta H_{14} = \Delta H_{MO\text{-}H} + \Delta H_E$$

where ΔH_D and ΔH_E correspond to the reactions,

$$HO_2 \leftrightarrow O + OH \qquad \Delta H_D$$

$$HO_2 \leftrightarrow H + O_2 \qquad \Delta H_E$$

Enthalpy for reaction (7), the first of the consecutive reactions involving propene, is calculated via:

$$\Delta H_7 = \Delta H_{abs} + \Delta H_B - \Delta H_F$$

where ΔH_F corresponds to the reaction,

$$C_3H_6 \leftrightarrow C_3H_5 + H \qquad \Delta H_F$$

$\Delta H_{MO\text{-}C3H5}$ is calculated as:

$$\Delta H_{MO\text{-}C3H5} = \Delta H_7 + \Delta H_{MO\text{-}C3H6} - \Delta H_F - \Delta H_{MO\text{-}H}$$

Reaction (9) is defined as:

$$\Delta H_9 = \Delta H_7 + \Delta H_F - \Delta H_G$$

where ΔH_G represents the reaction enthalpy for:

$$C_3H_5 \leftrightarrow C_3H_4 + H \qquad \Delta H_G$$

In determining ΔH_9, C_3H_4 is assumed to desorb from the surface without any barrier. Reaction (10) is calculated as:

$$\Delta H_{10} = \Delta H_I - \Delta H_{MO\text{-}C3H5} - \Delta H_{M\text{-}O}$$

where ΔH_I represents the reaction enthalpy for:

$$C_3H_5 + O \leftrightarrow CH_2O + C_2H_3$$

In determining ΔH_{10}, CH_2O is assumed to desorb from the surface without any barrier.

Finally, the Eley-Rideal abstraction of hydrogen from gas-phase allyl radicals, $C_3H_5 + O^* \leftrightarrow C_3H_4 + OH^*$, is determined according to:

$$\Delta H_{11} = \Delta H_{MO\text{-}H} + \Delta H_G$$

Chapter 5 – Conclusions and Recommendations for Future Work

5.1 Conclusions

This thesis explores the potential application of partial oxidation in alkane-to-alkene transformation. While attractive in principle, partial oxidative routes have not seen much commercial success stemming from an inability to prevent unwanted CO_x formation. The challenge of controlled oxidation has rebuffed numerous attempts by researchers to synthesize economically viable catalysts.

It is in the context of these previous efforts that the notion of a fundamental upper bound on performance has arisen. Alongside this is the complementary issue of what role the catalyst plays in influencing the selectivity-conversion trajectory. In OCM and ODHP, we began from simple formalisms of thermodynamic and physical consistency to construct surface mechanisms encompassing a range of hypothetical catalysts. By utilizing a simulation approach, we were able to methodically manipulate our catalyst surface kinetics and isolate limiting constraints. This allowed us to explain why maxima in yield occurred, to determine which reactions were critical, to isolate basic catalyst properties associated with high yields, to see how current catalysts compared to what was potentially possible, and to evaluate whether these partial oxidation reactions were economically viable.

Hand in hand with trying to understand the consequences of manipulating the catalyst surface energetics is possessing the ability to do so in real systems. In examining catalysts for ODHE and ODHP, we focused on incorporating dopants into the support as one possible option. In Chapter 2, we showed strong evidence that our synthesis method achieved the successful doping of Si into ZrO_2. Furthermore, we tied the incorporation of dopants to specific changes in the catalyst surface energetics, with resultant changes in the performance and stability of LiCl/NaCl/CeO_2/Si-doped SZ, and MoO_x/Nb-doped ZrO_2 and LiCl/Nd_2O_3/In-doped SZ for ODHE and ODHP, respectively. Thus, we were able to achieve yields that matched or surpassed those of the best reported literature values.

Ultimately, our objective would be the rational design of catalysts through a combination of simulations and creative synthesis. While we are still far away from

combining simulation and experiment in designing custom-made catalysts, we have taken a few steps towards this important goal.

5.2 Recommendations for Future Work

The construction of yield bounds represents an exciting endeavor and, in some ways, a new way of looking at catalyst development. We have only just begun to tap into the potential of this approach. As with any first attempt, we have relied heavily on readily available tools such as the CHEMKIN™ software.[1] One direct consequence of this was that we were forced to ignore microporosity in representing the catalyst packed bed. It is our firm belief that the effects of catalyst microporosity deserve a more thorough treatment than given here. In principle, catalyst microporosity can be taken into account by the dusty gas model,[2] which treats the catalyst as an agglomeration of large, immobile dust molecules. In terms of practical implementation, however, this means separating from the use of CHEMKIN™ modules. Several options exist that may facilitate this transition. One approach would be to build from modules such as Twopoint™ and ckinterp.f, which are a boundary value problem solver and a reaction rate generation program, respectively. Their source codes are available from an older, open-source version of CHEMKIN™. Alternatively, the dusty gas model can be constructed in FEMLAB™, which would allow us to take advantage of several helpful MATLAB™ routines, including the efficient uploading, databasing, and reaction-constructing routines incorporated in the open source toolbox, ReactionLab™.[3]

In our work on ODHE, we have touched on four methods for manipulating the LiCl-support interaction, namely, (i) the use of alternative anions such as MoO_x and WO_x, (ii) the incorporation of dopants, (iii) the use of alkali salt mixtures, and (iv) the impregnation of secondary metal oxides. Of the four methods, it appeared that the potential of alkali mixtures has been the least explored. Existing phase diagrams of binary alkali mixtures, while providing an initial guide to phenomenon such as the molten salt transition temperature, do not take into consideration the significant influence of the underlying support. Given the sensitivity of the molten salt transition temperature to the alkali mixture composition, however, a more detailed mapping of alkali mixtures should be undertaken. Similarly, while initial efforts to enhance ODHP performance through the

use of binary mixtures of alkali salts (e.g. LiCl/NaCl and LiCl/CsCl) have thus far proven unsuccessful (not shown), given their dramatic impact on ODHE performance, a more detailed exploration is warranted.

Work also remains in terms of improving the kinetic model for ODHP. Here, automated reaction-generating mechanism techniques[4,5] (e.g. RMG[6]) may provide insights into the missed reaction channels for allene degradation. *Ab initio* calculations can then be used to improve reaction parameter estimates for reactions that are particularly sensitive. Our research has also shown that allyl chemistry deserves much greater attention. While we admittedly have an incomplete understanding of allene combustion routes, quantum calculations of $C_3H_5 + O^* \leftrightarrow C_3H_4 + OH^*$ over a representative sample of metal oxides could allow us to set a stricter bound on ODHP.

Finally, in terms of a practical system for propene generation, the short contact time approach developed by Huff and Schmidt[7] remains very promising. It would be of interest to follow up their work, giving a more detailed analysis of the kinetics involved. In particular, the possibility of heterogeneous-initiated, homogeneous reaction should be considered more thoroughly. Calculation of a yield bound for this system would also be of interest since Huff and Schmidt[7] have speculated that different metals or metal alloys could be used to enhance performance. For metal-catalyzed systems, reference data (i.e., for O_2 and alkane chemisorptions) and techniques (i.e, BOC-MP) are readily available for providing good estimates of barrier heights.

5.3 References

[1] Kee, R. J., Rupley, F. M., Miller, J. A., Coltrin, M. E., Grcar, J. F., Meeks, E., Moffat, H. K., Lutz, A. E., Dixon-Lewis, G., Smooke, M. D., Warnatz, J., Evans, G. H., Larson, R. S., Mitchell, R. E., Petzold, L. R., Reynolds, W. C., Caracotsios, M., Stewart, W. E., Glarborg, P., Wang, C., and Adigun, O., CHEMKIN Collection, Release 3.6, Reaction Design, Inc., San Diego, 2000.

[2] Jackson, R., "Transport in Porous Catalysts." Elsevier Scientific Publishing Company, New York, 1977.

[3] Frenklach, M., and Nokleberg, C. J., *ReactionLab*, 1 December 2003, <http://reactionlab.sf.net/> (22 October 2002).

[4] Susnow, R. G., Dean, A. M., Green, W. H., Jr., Peczak, P., and Broadbelt, L. J., *J. Phys. Chem. A* **101**, 3731 (1997).

[5] Matheu, D. M., Dean, A. M., Grenda, J. M., and Green, W. H., Jr., *J. Phys. Chem. A* **107**, 8552 (2003).

[6] Song, J., "Building Robust Chemical Reaction Mechanisms: Next Generation of Automatic Made Construction Software." (Ph.D. Thesis, Massachusetts Institute of Technology, 2003).

[7] Huff, M., and Schmidt, L. D., *J. Catal.* **149**, 127 (1994).